Monthly Notices of the ROYAL ASTRONOMICAL SOCIETY

MNRAS **552,** 1–63 (2026)
Advance Access publication 2026 June 29

https://doi.org/10.1093/mnras/stag1204

Composite bulges – V. Detecting signatures of gas inflows in IFU data: the MUSE view of ionized gas kinematics in nearby galaxies

Tutku Kolcu [1,2★] Witold Maciejewski,[1★] Peter Erwin [3,4†] Dimitri A. Gadotti [5] Francesca Fragkoudi [6] Paula R. T. Coelho [7] Victor P. Debattista [8] Adriana de Lorenzo-Cáceres,[9,10] Camila de Sá-Freitas [11] and Patricia Sánchez-Blázquez [12,13]

[1]*Astrophysics Research Institute, Liverpool John Moores University, IC2 Liverpool Science Park, 146 Brownlow Hill L3 5RF, UK*
[2]*School of Physics and Astronomy, University of Nottingham, University Park, Nottingham NG7 2RD, UK*
[3]*Max-Planck-Institut für Extraterrestrische Physik, Giessenbachstrasse, D-85748 Garching, Germany*
[4]*Universitäts-Sternwarte München, Scheinerstrasse 1, D-81679 München, Germany*
[5]*Centre for Extragalactic Astronomy, Department of Physics, Durham University, South Road, Durham DH1 3LE, UK*
[6]*Institute for Computational Cosmology, Department of Physics, Durham University, Durham DH1 3LE, UK*
[7]*Universidade de São Paulo, Instituto de Astronomia, Geofísica e Ciências Atmosféricas, Rua do Matão 1226, 05508-090 São Paulo-SP, Brazil*
[8]*Jeremiah Horrocks Institute, University of Lancashire, Preston PR1 2HE, UK*
[9]*Universidad de La Laguna, Departamento de Astrofísica. Avda. Astrofísico Francisco Sánchez SNR, E-38206 San Cristóbal de La Laguna, Tenerife, Spain*
[10]*Instituto de Astrofísica de Canarias. C/vía Láctea SNR, E-38205 San Cristóbal de La Laguna, Tenerife, Spain*
[11]*European Southern Observatory, Alonso de Córdova 3107, Vitacura, Región Metropolitana, Chile*
[12]*Departamento de Física de la Tierra y Astrofísica, Universidad Complutense de Madrid, E-28040, Madrid, Spain*
[13]*Instituto de Física de Partículas y Ciencias del Cosmos IPARCOS, Universidad Complutense de Madrid, E-28040, Madrid, Spain*

Accepted 2026 June 18. Received 2026 June 17; in original form 2025 December 11

ABSTRACT

Using VLT/MUSE data, we study the ionized-gas kinematics in a mass- and volume-limited ($M_* \geq 10^{10}\mathrm{M}_\odot$, $D \leq 20$ Mpc) sample of 21 nearby galaxies to identify signatures of extended shocks within their inner kiloparsec, which appear as coherent velocity jumps in kinematic maps. By removing angular momentum, shocks in gas cause inflows, which can trigger nuclear star formation and fuel active galactic nucleus (AGN) activity. To identify the signatures of extended shocks, we examine residual velocity fields after subtracting a modelled rotating disc, and we study velocity difference between various gas tracers. Combining our kinematic analysis with Baldwin, Phillips, Terlevich (BPT) ionization diagnostic maps and dust morphology, we find that 12 of 21 galaxies (∼57 per cent) show extended shock signatures with velocity jumps consistent with models of bar-driven shocks. This is likely a lower limit, as three additional galaxies (∼14 per cent) exhibit shocks along bars, potentially reaching the nucleus but obscured by AGN outflows. We trace shock signatures inwards close to the resolution limit, which suggests that shocks may be the prevailing mechanism of inflow in the central kpc of galaxies. The only two unbarred galaxies in our sample are also the only systems with unperturbed kinematics and no shocks, strongly linking the perturbed gas dynamics in centres of galaxies to the presence of bars. All galaxies with inner bars show LINER- or Seyfert-like nuclear emission, whereas galaxies without inner bars exhibit all emission types, indicating that regardless of gas supply, inner bars suppress star formation in galactic nuclei.

Key words: shock waves – galaxies: general – galaxies: kinematics and dynamics – galaxies: star formation.

1 INTRODUCTION

Gas inflows in galaxies can significantly affect their evolution by enhancing nuclear star formation (M. A. Prieto et al. 2019) and feeding the active galactic nucleus (AGN; R. I. Davies et al. 2014; A. Audibert et al. 2019), which consequently triggers AGN outflows (M. A. Prieto, W. Maciejewski & J. Reunanen 2005; R. I. Davies et al. 2014; A. Audibert et al. 2019) that in turn may cause quenching by suppressing star formation (Z.-y. Man et al. 2019; M. Donnari et al. 2021). Numerous observational and theoretical studies have investigated the mechanisms driving gas inflows in galaxies (R. H. Sanders & J. M. Huntley 1976; E. Emsellem, P. Goudfrooij & P. Ferruit 2003; K. Fathi 2004; M. A. Prieto et al. 2019). Tidal forces exerted during close encounters or collisions distort and reshape galactic structure, and redistribute angular momentum across the galaxy, leading to gas inflows (J. E. Barnes & L. Hernquist 1996; J. C. Mihos & L. Hernquist 1996; P. F.

★ E-mail: Tutku.Kolcu@nottingham.ac.uk (TK); w.maciejewski@ljmu.ac.uk (WM)
† Deceased

© The Author(s) 2026.
Published by Oxford University Press on behalf of Royal Astronomical Society. This is an Open Access article distributed under the terms of the Creative Commons Attribution License (https://creativecommons.org/licenses/by/4.0/), which permits unrestricted reuse, distribution, and reproduction in any medium, provided the original work is properly cited.

Downloaded from academic.oup.com/mnras/article/552/3/stag1204/8721813 by guest on 30 October 2026

Hopkins & L. Hernquist 2006; B. Robertson et al. 2006; C. d. P. Lagos et al. 2018). Moreover, density waves which create spiral arms can exert torques to the gas and stars (J. Roberts, M. S. Roberts & F. H. Shu 1975; S. Kendall et al. 2008), affecting the overall distribution of angular momentum in the galaxy, and causing gas inflows (D. M. Elmegreen et al. 1999; P. Grosbøl, P. A. Patsis & E. Pompei 2004). Dynamical friction is another pivotal mechanism that can cause infall. As satellites, globular clusters or giant molecular clouds orbit within/around a galaxy, the dynamical friction against the galaxy's stellar population can slow these bodies down, consequently leading to angular momentum exchange between these bodies and the galaxy's medium (F. Combes 2003; E. D'Onghia et al. 2006; S. Jogee 2006; A. A. Dutton & F. C. van den Bosch 2012).

Gas inflow can induce the secular evolutionary processes that slowly shape the galaxy's structure over time, promoting the reshaping of disc profiles (I. Shlosman & M. Noguchi 1993; J. F. Navarro, C. S. Frenk & S. D. M. White 1995), the formation and growth of central substructures such as gaseous and stellar discs and rings (I. Shlosman, J. Frank & M. C. Begelman 1989; E. Athanassoula 1992; C. H. Heller & I. Shlosman 1994; R. Buta & F. Combes 1996; T. Storchi-Bergmann et al. 2003; P. Martini et al. 2003; K. Fathi et al. 2005; W.-T. Kim & J. M. Stone 2012; M. C. Sormani, J. Binney & J. Magorrian 2015), and triggering starbursts in nuclear rings (C. H. Heller & I. Shlosman 1994; L. M. Mazzuca et al. 2008). Furthermore, gas reaching the nucleus can contribute to nuclear feeding (C. H. Heller & I. Shlosman 1994; K. Park & T. Bogdanović 2017). Another mechanism that can introduce a dimension of complexity to gas dynamics is magnetic loops; large-scale structures of magnetic fields that arch above the galactic plane. These structures can influence the regulation of galactic magnetic fields (M. Krause, E. Hummel & R. Beck 1989; R. Beck & R. Wielebinski 2013), gas dynamics (D. Liu et al. 2023), star formation (C. F. McKee & E. C. Ostriker 2007), and the nuclear feeding cycle (Y. Hu et al. 2022); their influence can also interfere with other galactic structures, such as bars (F. Abbate et al. 2020).

One of the most established mechanisms causing gas inflows involves shocks driven by bars. In the local universe, disc galaxies commonly host non-axisymmetric central stellar structures, with approximately two-thirds of this population hosting bars (P. B. Eskridge et al. 2000; K. Menéndez-Delmestre et al. 2007; D. A. Gadotti 2009; R. J. Buta et al. 2015). Simulations have revealed that the bars play a crucial role in transporting gas from the outer regions to the inner kiloparsec of galaxies (E. Athanassoula 1992; S. García-Burillo et al. 2005; F. Fragkoudi, E. Athanassoula & A. Bosma 2016). Torques generated by the bar pull gas clouds which can then collide with large relative velocities, causing shocks in gas. Angular momentum transfer in shocks results in inflow of gas towards the inner regions of the galaxy. Once a steady-state flow is established, cloud collisions and therefore shocks in gas, occur at specific locations, which can extend over significant portions of a galaxy, for several hundreds of parsecs. Here, we call such structures *extended shocks*. Numerical models indicate that gas inflows occur in extended shocks, usually of either straight or spiral shape (E. Athanassoula 1992; W. Maciejewski 2004). However, despite extensive research, it remains unclear whether extended shocks provide the dominant mechanism for gas inflow to galactic nuclei or whether the inflow there has a different origin.

Shock fronts in gas are surfaces across which gas characteristics undergo abrupt changes: gas density and temperature increase, and its velocity is reduced, according to the jump conditions (L. D. Landau & E. M. Lifshitz 1984). As such velocity jumps are present in extended shocks throughout their extent, extended shocks appear in observations as coherent kinematic structures (A. Zurita et al. 2004; K. Fathi et al. 2005; T. Storchi-Bergmann et al. 2007). Our objective in this work is to study the gas kinematic maps of the innermost galactic regions, within ∼1 kpc radius, in search of the signatures of coherent kinematic structures that display straight or spiral morphology consistent with that associated with the shocks in models of gas dynamics. As coherent structures can be missed in incomplete kinematic maps derived from clumpy emission, we rely on gas tracers that provide closest to complete coverage of the inner kiloparsec – Hα and [N II]λ6583 emission from ionized gas, observed with the *Multi Unit Spectroscopic Explorer* (MUSE) is the optimal choice for coverage and resolution. Our findings allow us to determine whether extended shocks are the prevalent mechanism of gas inflows to the galactic nuclei. We build on our pilot study presented in T. Kolcu et al. (2023), where, on the example of NGC 1097, we introduced our methods to highlight and identify the signatures of extended shocks in kinematic maps. In this work, we refine and apply these methods to all galaxies from the *Composite Bulges Survey* (*CBS*, PI: P. Erwin; P. Erwin et al. 2021; T. Kolcu et al. 2023; A. Ashok et al. 2023), and to two other galaxies that satisfy the selection criteria of the CBS sample, for which data with sufficient emission line signal are available. When compared to previous work, suffering from instrumental limitations of former generation integral field units (IFUs; K. Fathi et al. 2005, 2006; T. Storchi-Bergmann et al. 2007), the level of details resolved with MUSE maximizes the prospect of finding the coherent kinematic structures that can unveil extended shocks which are approaching the nucleus of galaxies.

The paper is organized as follows. In Section 2, we describe the sample selection and the MUSE observations of the galaxies analysed in this study. In Section 3, we outline the procedure used to extract stellar and ionized-gas kinematics from the MUSE spectroscopy. In Section 4, we summarize the motivation behind the different techniques employed to identify signatures of extended shocks and highlights the complementarity of these approaches. In Section 5, we present the collective analysis of the sample, drawing on the detailed kinematic results provided galaxy-by-galaxy in Appendix A. Specifically, we discuss the quantitative properties of the shocks (e.g. velocity jumps, radial extents) in Section 5.1, the common features evident across the sample in Section 5.2, and the grouping of galaxies according to shock class and nuclear emission in Sections 5.3 and 5.4, respectively. In Section 6, we explore correlations between the observed quantities and other galaxy properties, including: the relation between kinematic categories and the presence of large-scale bars (Section 6.1); correlations with inner bars (Section 6.2); the connection between the strength of extended shocks and the gas velocity dispersion (Section 6.3); and the dependence on host-galaxy mass (Section 6.4). Finally, Section 7 provides a summary of the main results and conclusions. We provide supplementary plots used in different parts of our analysis in Appendix B.

2 SAMPLE SELECTION AND MUSE OBSERVATIONS

2.1 Sample selection

The galaxy sample studied in this work comprises targets from the multiwavelength imaging and spectroscopic campaign CBS (PI: Peter Erwin; P. Erwin et al. 2021; T. Kolcu et al. 2023; A. Ashok et al. 2023) that show sufficiently strong ionized-gas

Downloaded from academic.oup.com/mnras/article/552/3/stag1204/8721813 by guest on 30 October 2026

emission in the MUSE data. We also include two additional galaxies that satisfy the CBS selection criteria but are not part of the CBS sample, and for which public MUSE observations are available. CBS focuses on understanding of the formation and growth mechanisms of bulges, and the correlation with their host galaxy properties. Moreover, it aims to identify and characterize the different forms of nuclear stellar components within the inner 1–2 kpc; from large-scale bars down to nuclear scale discs/rings/bars and nuclear star clusters (P. Erwin et al. 2021; A. Ashok et al. 2023).

The CBS sample is a mass- ($M_* \geq 10^{10}\,M_\odot$) and volume- ($D \leq 20$ Mpc) limited set of 53 S0–Sbc galaxies with Galactic latitude $|b| > 20^\circ$ and inclinations between 35° and 60° (P. Erwin et al. 2021). The sample has optical and near-infrared imaging with *the Hubble Space Telescope* (*HST*); at the survey distance limit, the near-infrared (IR) *HST F*160*W* image quality (PSF FWHM ≈ 0.15 arcsec) corresponds to a physical resolution of ∼10–15 pc, enabling us to resolve substructures within the inner bulge regions. Among 53 galaxies in CBS, 46 of them have been observed with MUSE, from which observations of 35 galaxies are obtained specifically for the CBS and observations of 11 galaxies are sourced from different programmes, including the *Time Inference with MUSE in Extragalactic Rings, TIMER Project* (PI: Dimitri Gadotti; D. A. Gadotti et al. 2019), the *MUSE Atlas of Disks, MAD* (PI: Marcella Carollo; S. Erroz-Ferrer et al. 2019), and the *Physics at High Angular resolution in Nearby GalaxieS Survey, PHANGS* (PI: Eva Schinnerer; E. Emsellem et al. 2022).

Upon reviewing the available MUSE data for the 46 galaxies in CBS, to ensure the reliability of the gas kinematics, we restrict our analysis to those galaxies with detected emission lines in more than 50 per cent of the spaxels within central 40 arcsec×40 arcsec (∼1 kpc). This specific field of view (FOV) covers the regions in which we search for kinematic signatures of extended shocks. This threshold was chosen to ensure the presence of sufficient emission line signal. This approach led to the selection of 19 galaxies from CBS. This criterion is a data-quality cut based on emission-line detectability across a spatial coverage, rather than on the measured velocities or dispersions. It should therefore not bias the kinematic measurements for galaxies that pass the cut, but it can introduce a selection bias by preferentially retaining systems with extended, high signal-to-noise (SNR) ionized-gas emission in the central ∼1 kpc (e.g. higher gas content or lower effective obscuration) and excluding gas-poor, centrally dust-obscured, or very compact-emission systems. Our results should thus be interpreted as representative of the CBS subset with spatially extended, detectable ionized gas, not the full parent sample.

To this sample, we added two galaxies from the TIMER Project (D. A. Gadotti et al. 2019). Since the CBS data set requires a minimum galaxy inclination of 35°, these galaxies, each with an inclination of 34°, were excluded from CBS, despite meeting all other criteria, such as distance and mass, and also surpassed the emission threshold we discussed in the previous paragraph. We decided to include these galaxies as the measurement error for inclination is at least on the order of 1°. We found no other galaxies at the limits of CBS selection criteria. As a result, our final sample comprises 21 galaxies. This is an almost complete sample of galaxies that satisfy the CBS selection criteria and have sufficient ionized emission, with the caveat that 7 out of 53 galaxies in the parent CBS sample have no MUSE observations.

From this sample, we selected NGC 1097 as a target for the pilot study where we developed the methodology for identifying extended shock signatures through kinematic analysis, which is presented in T. Kolcu et al. (2023, hereafter Paper IV). This methodology was then advanced and used for the remaining galaxies in our sample, whose analysis is presented in this work. More details on our methodology are provided in Section 4.

2.2 MUSE observations of the sample

Observations of all galaxies are done in MUSE Wide-Field Mode, WFM (R. Bacon et al. 2010). MUSE, mounted on the UT4 of the Very Large Telescope (R. Bacon et al. 2010), with its large, 60 arcsec×60 arcsec FOV, and fine, 0.2 arcsec×0.2 arcsec spatial sampling, allows capturing extensive portions of the central regions of nearby galaxies in great detail, across a rest frame wavelength range of 4650 to 9300 Å which covers prominent emission lines. Over this range, the instrumental spectral resolution corresponds to an approximately wavelength-dependent full width at half-maximum (FWHM) of ∼2.5–2.9 Å (equivalently $R \simeq 1770$ at 4800 Å increasing to $R \simeq 3590$ at 9300 Å). Besides these capabilities, MUSE also offers high sensitivity, providing high SNR, effectively minimising the common need for binning. Furthermore, MUSE is equipped with cutting-edge adaptive optics (AO) technology, contributing significantly to the data acquisition by correcting for atmospheric distortions, improving the seeing and allowing us to achieve fine spatial resolutions.[1]

In Table 1, we summarize the general properties and observations of each galaxy studied in this work. The spatial scale in pc per arcsec, for each galaxy is derived from the adopted distance listed in the table via the angular–physical conversion. The spatial resolution (SR) is then estimated from the delivered image quality, quantified by the median point spread function (PSF) full width at half maximum (FWHM; 'seeing') measured from the VLT guide star in the *V* band during MUSE slow-guiding exposures, using SR = (spatial scale) × (PSF FWHM). For a given PSF FWHM, the physical resolution therefore scales linearly with distance.

However, during the observations of 10 galaxies obtained for CBS and for NGC 1566 from MAD, MUSE's AO system is used. Therefore, for these galaxies, using the approach from T. Fusco et al. (2020), which accounts for AO monitoring, the PSF FHWMs have been reconstructed to obtain the corrected values. This method demonstrates significant improvements in the seeing for most galaxies, typically between 30 and 50 per cent. The PSF FHWMs recorded during observations, along with those improved by AO, are detailed in Table 1. This table also includes RC3 classification of each galaxy from G. Vaucouleurs et al. (1991), and the logarithmic stellar masses obtained from the *Spitzer* Survey of Stellar Structure in Galaxies (S4G), which have an approximate accuracy of 0.1 dex (J. C. Muñoz-Mateos et al. 2013, 2015). For NGC 7177, which is not included in S4G, the stellar mass is estimated from its *B*-band absolute magnitude in the HyperLEDA data base, assuming the same 0.1 dex uncertainty.

The large-scale images of each galaxy within our sample are provided in their respective sections in Appendix A, while their detailed analysis is explained. While images of IC 2051, NGC 289, NGC 613, NGC 1300, NGC 1433, NGC 1566, NGC 4941, and NGC 7513 are taken from The Carnegie-Irvine Galaxy

[1]The delivered spatial resolution, quantified by the PSF FWHM is 0.44–1.21 arcsec across our sample (median 0.7 arcsec; Table 1). This corresponds to ∼25–95 pc at the target distances (median ∼60 pc).

Downloaded from academic.oup.com/mnras/article/552/3/stag1204/8721813 by guest on 30 October 2026

Table 1. The galaxy sample studied in this work. NGC 1097, whose analysis is presented in T. Kolcu et al. (2023) is included to this table for completeness.

Galaxy ID	RC3	$\log_{10}(M_*/M_\odot)$	Vel_{sys} (km s^{-1})	Distance (Mpc)	Scale (pc arcsec^{-1})	Seeing (arcsec)	SR (pc)	Source	Proposal ID	Observing period
(1)	(2)	(3)	(4)	(5)	(6)	(7)	(8)	(9)	(10)	(11)
IC 2051	SBbc	10.58	1741	19.9[a]	96.5	0.79	76.0	CBS	0104.B-0404(A)	104
NGC 289	SBbc	10.63	1629	20.2 [a]	97.9	0.70	69.0	MAD	096.B-0309(A)	96
NGC 613	SBbc	11.09	1481	18.1[a]	87.8	1.00	88.0	TIMER	097.B-0640	97
NGC 1097	SBb	11.24	1271	14.8[a]	71.7	0.80	58.0	TIMER	097.B-0640	97
NGC 1300	SBbc	10.58	1573	19.6[a]	95.0	1.00	95.0	TIMER	097.B-0640	97
NGC 1433	SB(r)ab	10.30	1074	18.6[b]	90.2	0.90	81.0	TIMER	097.B-0640	97
NGC 1566	SABbc	10.58	1501	17.0[a]	82.4	0.56*	46.0	MAD	0100.B-0116(A)	100
NGC 3351	SBb	10.49	779	10.0[c]	48.5	0.70	34.0	TIMER	097.B-0640	97
NGC 3368	SABab	10.72	882	10.5[c]	50.9	0.49*	25.0	CBS	0104.B-0404(A)	104
NGC 3489	SAB0	10.14	677	11.7[d]	56.7	0.52*	30.0	CBS	109.22VU.001	109
NGC 3626	SAB0	10.59	1489	19.5[e]	94.5	0.48*	46.0	CBS	109.22VU.001	109
NGC 4237	SAbc	10.36	864	18.9[e]	91.6	0.44*	40.0	CBS	0104.B-0404(A)	104
NGC 4303	SAB(rs)bc	10.86	1562	17.0 [b]	82.4	0.80	66.0	TIMER	097.B-0640	97
NGC 4321	SABbc	10.93	1566	15.2[c]	73.7	0.86*	64.0	CBS	0104.B-0404(A)	104
NGC 4380	SAb	10.32	952	15.9[e]	77.1	0.49*	38.0	CBS	0104.B-0404(A)	104
NGC 4457	SAB0/a	10.58	880	16.5[f]	80.0	0.59*	47.0	CBS	109.22VU.001	109
NGC 4643	SB0/a	11.03	1331	19.1[a]	92.6	0.90	84.0	TIMER	097.B-0640	97
NGC 4941	SABab	10.36	1113	15.6[a]	75.6	1.21	92.0	MAD	096.B-0309(A)	96
NGC 5248	SABbc	10.67	1150	17.3[a]	83.9	0.70	59.0	TIMER	097.B-0640	97
NGC 7177	SABb	10.44	1146	17.5[a]	84.8	0.89*	76.0	CBS	109.22VU.001	109
NGC 7513	SBb	10.21	1566	19.8[a]	96.0	0.58*	56.0	CBS	109.22VU.001	109

Notes. (1) Galaxy; (2) RC3 classification (G. Vaucouleurs et al. 1991); (3) Stellar mass from S^{4}G; (4) Systemic velocity from NED; (5) Distance sources; (6) Spatial scale; (7) PSF FWHM (seeing), star denotes AO-corrected values following T. Fusco et al. (2020); (8) Spatial resolution; (9) IFU data source; (10) Proposal ID; (11) ESO observing period.
[a]Virgocentric-corrected redshift from HyperLEDA with $H_0 = 72$.
[b]TRGB (G. S. Anand et al. 2021).
[c]Cepheids (metallicity-corrected) (W. L. Freedman et al. 2001).
[d]SBF (J. L. Tonry et al. 2001) with correction from S. Mei et al. (2005).
[e]SBF (M. Cantiello et al. 2018).
[f]Virgo Cluster distances.

Survey, CGS.[2] (L. C. Ho et al. 2011; Z.-Y. Li et al. 2011), for the remaining galaxies in our sample, we use *ugriz* images from Sloan Digital Sky Survey (SDSS[3] ; M. A. Strauss et al. 2002; M. R. Blanton et al. 2017).

3 EXTRACTION OF THE KINEMATIC DATA

To derive emission line fluxes and to extract stellar and ionized gas kinematics from MUSE data, we employed the Data Analysis Pipeline[4] (DAP) of the PHANGS collaboration (E. Emsellem et al. 2022), which is an implementation based on the `gist` pipeline (A. Bittner et al. 2019), an exceptionally functional software of modular structure. DAP employs the commonly used penalized pixel-fitting (PPXF) code (M. Cappellari & E. Emsellem 2004) to perform both stellar and emission line analysis. It can also perform stellar population analysis but to optimize the processing time we discarded this module, since it was outside of the scope of this work.

[2]The CGS sample images can be accessed via https://cgs.obs.carnegiescience.edu/CGS/database_tables/sample0.html.
[3]SDSS webpage can be accessed via the link https://skyserver.sdss.org/dr16/en/home.aspx.
[4]DAP can be accessed at: https://gitlab.com/francbelf/ifu-pipeline.

3.1 Extracting stellar line-of-sight velocity distribution moments

We obtain the stellar kinematics in the form of line-of-sight velocity distribution moments (LOSVD) – mean velocity (V), velocity dispersion (σ), and higher order Gauss–Hermite moments ($h3$ and $h4$).

The data are re-sampled on a logarithmic wavelength axis and then spatially binned with Voronoi tessellation (M. Cappellari & Y. Copin 2003). For the spectral fitting, we use a nominal rest-frame wavelength range of 4800–7000 Å. By using PPXF, we convolve Extended Medium-resolution Isaac Newton Telescope library of empirical spectra (E-MILES) single-stellar population (SSP) models (A. Vazdekis et al. 2015) with the LOSVD, which are then fitted to each spectrum. The best-fitting parameters are determined by χ^2 minimization in pixel space. To exclude low-quality spaxels dominated by noise, we impose a minimum SNR threshold of 3, consistent with commonly adopted IFU analysis set-ups (e.g. A. Bittner et al. 2019), where spaxels below the isophotal detection limit (typically $\langle SNR \rangle \approx 3$) are excluded to avoid low-surface-brightness systematics. Additionally, each Voronoi bin is targeted to achieve an SNR of 40, a commonly used value in the literature that balances the accuracy of the extracted measurements with spatial resolution (R. P. der Marel & M. Franx 1993).

We employed eighth-order multiplicative Legendre polynomials in PPXF to fit the stellar continuum, which corrects inaccuracies in the spectral calibration and eliminates the need to

Downloaded from academic.oup.com/mnras/article/552/3/stag1204/8721813 by guest on 30 October 2026

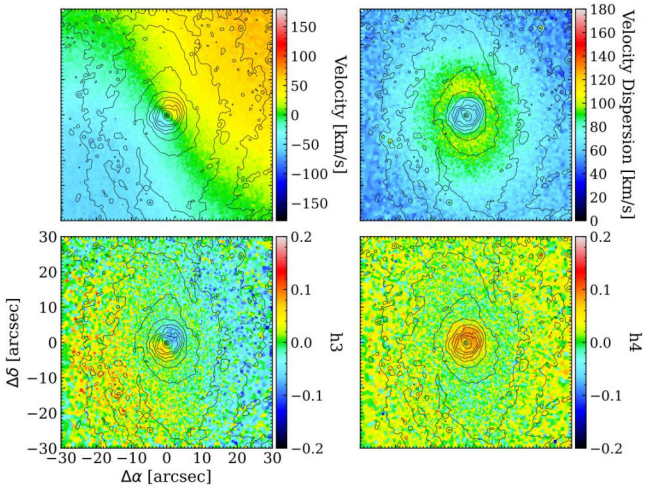

Figure 1. Stellar kinematic maps of NGC 4303. Panels show stellar velocity (top left), stellar velocity dispersion (top right), $h3$ (bottom left), and $h4$ (bottom right) moments of LOSVD. The black contours represent the continuum flux. Galaxy centre is at $\Delta\alpha$, $\Delta\delta$= [0,0].

provide dust reddening curves (M. Cappellari 2017) in fitting. While additive polynomials can reduce discrepancies between stellar templates and absorption lines, and remove artefacts caused by sky subtraction (M. Cappellari 2017), they can also alter the equivalent width of the Balmer absorption lines and introduce non-physical corrections to line fluxes (E. Emsellem et al. 2022). Therefore, we chose not to include additive polynomials in our fitting process.

The maps of mean velocity (V), velocity dispersion (σ), and higher order Gauss–Hermite moments $h3$ and $h4$ for a representative galaxy from our sample, NGC 4303, are shown in Fig. 1, with the continuum flux overplotted. The mean velocity in each spaxel is corrected for the galaxy's systemic velocity, taken from the NASA/IPAC Extragalactic Database (NED[5]), and provided in Table 1. The centre of galaxy is identified with the brightest spaxel in its nucleus and is located at $\Delta\alpha$, $\Delta\delta = [0, 0]$ on each map. As this paper does not focus on stellar kinematics, we do not present the stellar kinematic maps of the remaining galaxies in our sample unless they are essential for understanding gas dynamics.

3.2 Extracting ionized gas line-of-sight velocity distribution moments for multicomponent gas

To obtain the ionized gas kinematics, we initially fit single Gaussian functions to the emission lines while simultaneously modelling the stellar continuum. The emission-line fitting is carried out on individual spaxels to preserve spatial resolution. During these fits, the stellar continuum is included but its kinematic parameters (velocity and dispersion) are fixed to the values previously determined from Voronoi-binned stellar kinematic fits. For each spectrum, PPXF performs a weighted χ^2 minimization using the per-pixel noise vector. Formal statistical uncertainties on gas kinematics and line fluxes are obtained from the covariance of the best-fitting solution (PPXF/GIST pipeline/Data Analysis pipeline), and thus depend on the line SNR and the spectral resolution through the adopted line profiles and instrumental broadening. We mask wavelength intervals affected by strong skylines and fit the stellar continuum and emission lines simultaneously to reduce biases from sky residuals and template mismatch; such systematics are not fully reflected in the formal error estimates.

We gathered the emission lines into three main groups, and among each group, the kinematics are shared. We left the emission line fluxes free from each other, except for the constraints from atomic physics (D. E. Osterbrock & G. J. Ferland 2006). The emission lines are grouped as follows:

(i) Balmer lines: H$\beta\lambda$4861, H$\alpha\lambda$6562 (hereafter Hβ and Hα).
(ii) Low-ionization lines: [N I]$\lambda\lambda$5197,5200; [N II]λ5754; [O I]$\lambda\lambda$6300,64; [N II]$\lambda\lambda$6548,83; [S II]$\lambda\lambda$6717,31.
(iii) High-ionization lines: [O III]$\lambda\lambda$4959,5007; [S III]λ6312.

The wavelengths singled out in each emission line group are taken from the National Institute of Standards and Technology (NIST)[6].

3.2.1 *Fitting emission lines with multiple Gaussians*

As we presented in Paper IV, our pilot study of NGC 1097 revealed a significant limitation of the standard approach of fitting emission lines with single Gaussians, when the line contains emission coming from different sources along the line of sight (LOS), such as from the disc and from the AGN outflows. When one attempts to fit such a line with a single Gaussian, the resultant fit is poor, which can artificially increase the velocity dispersion and alter the velocity. Such inaccuracies could significantly impact our work, particularly when constructing diagnostic maps of residual velocity and velocity differences, in which we search for the kinematic signatures of extended shocks (see Section 4).

Therefore, for spaxels that show unusually high velocity dispersion, compared to their surroundings, for any group of emission lines, we carefully examined the spectra for signs of multiple sources of emission which are expected to show up as an *excess emission* from the weaker source superimposed on the Gaussian profile of the emission from the stronger source. Discovering such emission signature prompts us to apply the *secondary component fitting approach*, introduced in Paper IV. When emission from two distinct sources is present along the LOS, fitting a secondary Gaussian component allows to separate out the emission attributed to excess sources and thus get a better estimate of the kinematics of the main source.

Galaxies studied in this work exhibited excess emission in their spectra that displayed more complex line features than those observed in NGC 1097's spectra in our pilot study. Therefore, we have found it necessary to tailor certain aspects of the secondary component fitting to accommodate the unique characteristics of each individual galaxy, which we explain below.

During this tailored emission line fitting process, we start with the same assumption that is made in the analysis of NGC 1097. We assume that the excess emission to which the secondary component is fitted comes from the same emission line to which the main component is fitted but either blue or redshifted with respect to the main component. If the excess emission is present in more than one emission line, we use the following configuration within DAP to incorporate secondary components to the emission line fitting: if excess emission is present in emission lines from different groups defined above, the kinematics of secondary

[5]NED can be accessed via https://ned.ipac.caltech.edu/.

[6]NIST can be accessed from https://www.nist.gov/pml/atomic-spectra-database.

Downloaded from academic.oup.com/mnras/article/552/3/stag1204/8721813 by guest on 30 October 2026

components are determined independently for each group. For example, in NGC 4303 (see Appendix A, Fig. A12), a secondary component fitted to [N II]λ6583 excess emission and a secondary component fitted to Hα excess emission are independent from each other. However, when excess emission is significant in more than one emission line within the same emission line group, such as [N II] doublets, the kinematics and the line ratios of the fitted secondary components are tied together, analogous to the approach used for tying the main component emission.

Although we have tried fitting the secondary components for various emission lines that show excess, only the one fitted to [N II]λ6583 changed the derived kinematics. In Paper IV, fitting of the secondary component to [N II]λ6583 not only influenced the kinematics derived for [N II]λ6583 but also reduced the Hα velocity dispersion by ∼20 per cent and shifted its LOS velocity by roughly 20 km s^{-1}. In this work, we find that in the three galaxies in our sample, in which a significant excess emission is present, including secondary component to [N II]λ6583 reduced the velocity dispersion of [N II]λ6583 by ∼15−25 per cent and shifted the LOS velocity by 20 up to 60 km s^{-1} in some spaxels at certain cases (see NGC 4303, Appendix A12). In these three galaxies, unlike in NGC 1097 shown in Paper IV, Hα kinematics were not significantly affected in by fitting of the secondary component. Moreover, none of the galaxies in our sample showed significant excess emission in [O III]λ5007, even in the regions with high [O III]λ5007 velocity dispersions. For instance, slightly non-Gaussian [O III]λ5007 profiles seen in NGC 4303's spectra are caused by a weak excess emission but including a secondary component to the fitting did not significantly influence the derived measurements. This suggests that [O III]λ5007 measurements from single Gaussian fits are in general reliable. Thus, to simplify the analysis and to reduce the number of free parameters in the fit, we omitted including a secondary component for [O III]λ5007 in these cases, this decision is elaborated further in Appendix A.

3.2.2 *Creating LOSVD moments' maps of multicomponent gas*

Although excess emission can significantly affect the measured velocity and velocity dispersion values of the main component, it does so for a small number of spaxels, generally grouped in a specific region of a galaxy. To identify which spaxels are most significantly affected by excess emission, we first analysed the differences between measurements from single Gaussian fits and those including secondary components. We focused on detecting large changes in the velocity and velocity dispersion measurements of the main emission line component caused by the introduction of a secondary Gaussian component. As in Paper IV, in order to construct the most accurate kinematic maps of the main emission component, we created masks, where these changes exceed certain magnitude. Within the mask, kinematic measurements for the main component were taken from the fits that included a secondary component. Outside the mask, kinematic measurements are made by fitting a single Gaussian to each emission line.

As the excess emission significantly affected only the measurements of [N II]λ6583, when establishing the masking criteria for the affected galaxies, we only used the [N II]λ6583 velocity shift and velocity dispersion change conditions. We refined the masking criteria employed in Paper IV by placing the following two conditions, which have to be satisfied for a spaxel to be included in the mask:

(i) there is a significant (≥10 km s^{-1}) [N II]λ6583 velocity shift or a substantial (≥15 per cent) decrease in [N II]λ6583 velocity dispersion between the single Gaussian fit and the fit including the secondary component

(ii) the velocity dispersion of the secondary [N II]λ6583 component is not excessively high, ensuring that the secondary component is a representation of real emission rather than noise.

For each of the three affected galaxies, the specific values chosen for the conditions listed above are detailed in their respective sections in Appendix A. Detailed information on the fitting approach of the secondary component, mask conditions, and further kinematic analysis for each of the three galaxies exhibiting excess emission in their spectra is provided in their respective sections in Appendix A (Sections A5, A12, and A13).

For each galaxy in our sample, the flux, velocity, and velocity dispersion maps across the three emission line groups are presented in the nine top right panels of Figs A1–A20. In the same panels of Fig. 2, these results are presented for the example of NGC 4303. For comparison, the kinematic maps of the three galaxies with excess emission, derived from single Gaussian fitting are presented in Fig. B1. The mean velocity in each spaxel is corrected for the galaxy's systemic velocity, taken from the NED and provided in Table 1. The centre of each galaxy is identified with the brightest spaxel in continuum emission in its nucleus and is located at $\Delta\alpha, \Delta\delta = [0, 0]$ on each map.

The refined fitting approach presented above significantly enhances the accuracy of the kinematic measurements extracted from MUSE data cubes, thereby minimizing errors associated with excess emission in the diagnostic maps we construct to search for the kinematic signatures of extended shocks. Consequently, this approach substantially improves the quality of the analysis and enhances the robustness of our findings.

4 METHODOLOGY

Orbital theory and hydrodynamical simulations indicate that shocks can play an important role in driving gas inwards towards galactic nuclei (E. Athanassoula 1992; W. Maciejewski 2004). Observationally, however, identifying such shocks is not straightforward. Although dust morphology can reveal structures that are suggestive of shock compression (P. Martini & R. W. Pogge 1999; R. W. Pogge & P. Martini 2002), morphology alone cannot determine whether these features truly correspond to shocks in the gas or instead arise from other processes unrelated to inflow. Kinematic information is therefore essential, since shocks are expected to produce rapid changes in velocity and hence extended signatures superimposed on the overall rotation pattern of the disc.

In Paper IV, we showed that residual velocity maps are a powerful diagnostic of such structures, but also that relying on a single method may be insufficient, because residual maps can be affected by uncertainties in the disc model and by vertical gas motions. For this reason, we combine complementary diagnostics based on kinematics, dust morphology, and ionization maps in order to identify and characterize signatures of extended shocks in the central regions of our galaxies. The sections that follow describe the techniques used in each approach, explain their complementarity, and summarize the logic of our identification strategy through a decision tree.

Downloaded from academic.oup.com/mnras/article/552/3/stag1204/8721813 by guest on 30 October 2026

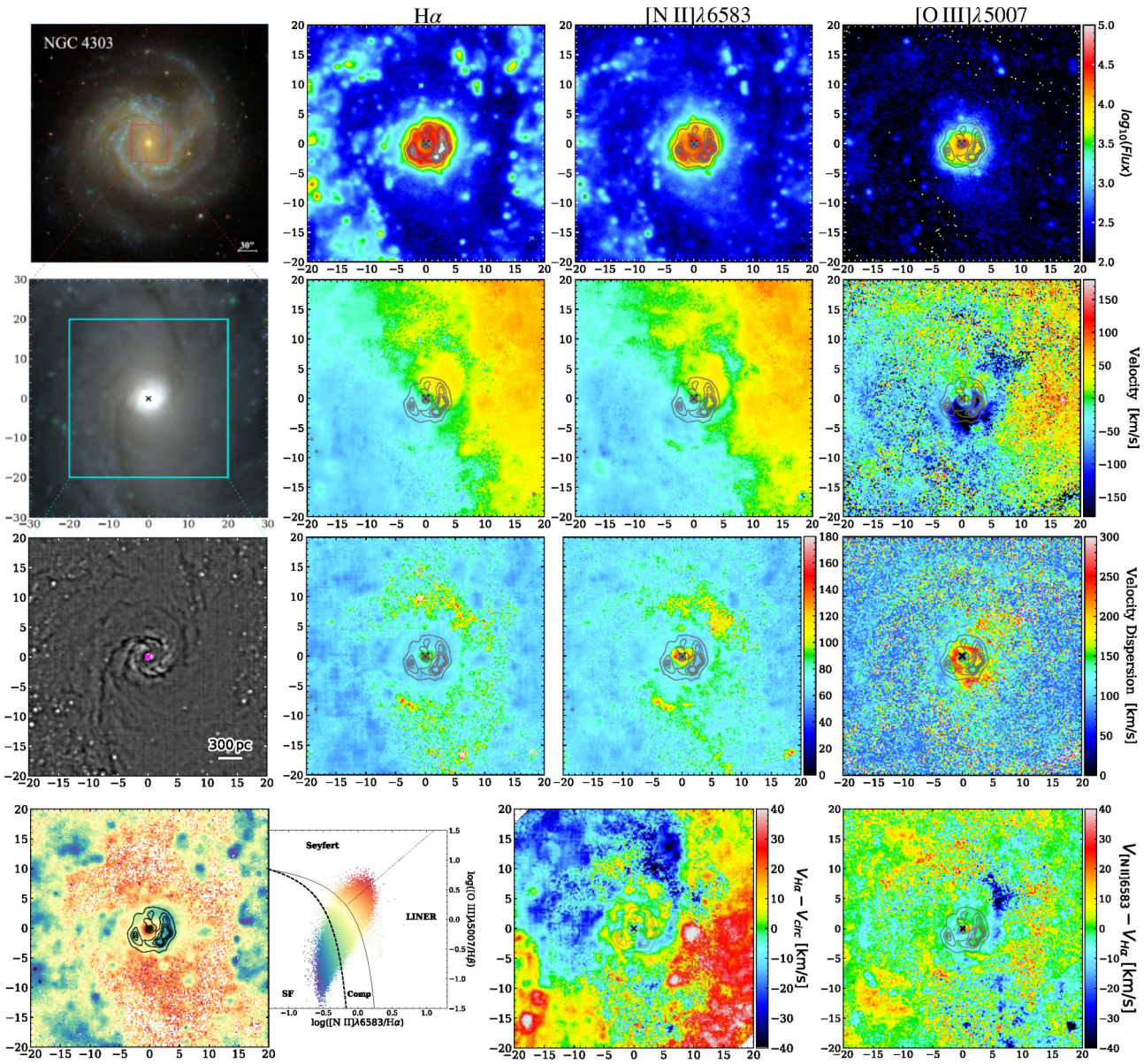

Figure 2. Images and diagnostic maps of NGC 4303. Unless stated otherwise, the *x*- and *y*-axes give positional offsets from the galaxy centre ($\Delta\alpha$, $\Delta\delta$) in arcseconds. The first three panels in the left-hand column show a large-scale image (taken either from CGS or SDSS) with the MUSE FOV is highlighted (top), a colour image constructed using MUSE data within the highlighed FOV , 40 arcsec × 40 arcsec region of the map is marked with a box (middle), and an unsharp mask image enclosed in the marked box, showing dust features (bottom). All other panels show the region enclosed within the highlighed box: top row – Hα, [N II]λ6583, [O III]λ5007 flux maps; second row – velocity maps; third row – velocity dispersion maps. The bottom row shows the BPT map with its diagnostic diagram (see Section 4.1.3), the residual velocity map (see Section 4.1.1), and the velocity difference map (see Section 4.1.2). The dark contours trace the Hαflux.

4.1 Techniques for identifying and characterizing signatures of extended shocks

4.1.1 A search for coherent kinematic structures in deviations from circular motion

Signatures of extended shocks are best highlighted in **residual velocity maps** created by fitting to the observed velocity field an axisymmetric rotating disc model, and then subtracting the velocity field of such model, which is referred as $V_{\rm circ}$ in Figs 2 and A1–A20, from the observed velocity field. Coherent structures in the residual velocity map that exhibit large magnitudes disclose the presence of extended shocks because shocks in gas cause velocity discontinuities.

For each galaxy, we model a thin flat rotating disc in circular motion by fitting the observed velocity field of Hα, using the KINEMETRY software (D. Krajnović et al. 2006). KINEMETRY is specifically designed for IFU data and performs a harmonic expansion along the best-fitting ellipses. The residual velocities highly depend on the disc orientation parameters defined in the disc model: the Position Angle (PA) of the line of nodes (LON) and the inclination (i). If the LOS velocity of a wrongly fitted disc

Downloaded from academic.oup.com/mnras/article/552/3/stag1204/8721813 by guest on 30 October 2026

model is subtracted from the observed LOS velocity, artefacts will arise in the residual velocity map (P. C. der Kruit & R. J. Allen 1978) and will obscure the real features coming from non-circular motion and velocity jumps. Therefore, to ensure the artefacts in the residual velocity field are not misinterpreted for real features, one must be careful while fitting the disc and examining the resultant maps.

As we explained thoroughly in Paper IV, to accurately model the thin flat rotating disc, one can perform three KINEMETRY fits, by gradually fixing the global disc orientation parameters. The first fit allows all ellipse parameters to vary, but we showed that the derived radial distributions of parameters do not significantly vary between the runs with the centre fixed or free. Thus, to optimize the analysis we omitted this first KINEMETRY fit and we ran KINEMETRY for a fixed centre and the additive constant in the expansion being equal to the velocity measured at the centre. We fix the centre at the photometric centre of each galaxy based on the brightest spaxel in its nucleus.

From the ellipse parameter distributions obtained in this initial fit, we deduce optimal values for the PA of the LON and i, which can accurately describe the galaxy disc, particularly within the inner kpc regions. Lastly, we construct our final disc model with centre, PA of LON, and i fixed to those deduced based on the previous fits. Due to insufficient data within ellipses in the inner 2 arcsec, and the influence of the AGN for AGN host galaxies, we consider the estimated parameters within this radius as unreliable and therefore discard them.

We note that our application of KINEMETRY assumes that the gas flow is intrinsically circular. For galaxies whose gas flow is dominated by local (e.g. stellar outflows) motions, the distributions of PA of the LON and i derived from KINEMETRY will show large fluctuations and settling on optimal values based on such fluctuated distributions will be challenging. Consequently, wrongly fitted parameters in the disc model will raise certain harmonic terms in residual velocity maps. For instance, an incorrect inclination can lead to m=3 harmonic terms, while an incorrect PA of the LON can result in m= 1 harmonic terms (P. C. der Kruit & R. J. Allen 1978). We show and explain this effect in sections 3.1 and 4.1 of Paper IV. If not taken into account with care, such artefacts can be mistakenly interpreted as real features.

Conversely, identifying the artefacts in residual velocity maps can guide us to determine the disc parameters that need to be adjusted. Thus, for galaxies whose disc orientation is not well constrained by KINEMETRY, we first define an initial PA of the LON and i based on the parameters computed from large-scale studies. Next, we alter these initial parameters within a range deduced from the fluctuated distributions given by KINEMETRY. With this approach, we construct different disc models and the corresponding residual velocity maps, in which we search for the signs of artefacts. As for the optimal disc orientation parameters, we settle on the values that minimize the strength of the artefacts in the residual velocity maps. After the rotating disc in circular motion is modelled, we subtract its LOS velocity from the observed LOS velocity to construct the residual velocity map.

Residual velocity maps showing extended structures are presented in Fig. 3, where the deprojected residual velocity values (residual velocity corrected for sin i) are displayed. In these maps, we search for coherent structures that extend over large spatial scales, similar to those observed in bars and nuclear spirals (A. Zurita et al. 2004; K. Fathi et al. 2005; J. Blasco-Herrera et al. 2013; A. Schnorr-Müller et al. 2016, 2017). The figure includes only galaxies in which such extended coherent structures are identified (which are outlined with dashed lines), and therefore serves as a representative example of the features targeted in our analysis. However, it is important to note that not all extended structures in the residual velocity map are associated with extended shocks in gas. To emphasize, the galaxies whose deprojected residual maps are presented in Fig. 3, are later grouped under different kinematic perturbation categories and not all structures are associated with extended shocks. Shock conditions imply a large change in velocity (E. Athanassoula 1992; W. Maciejewski 2004). Thus, besides their coherent appearance, these structures should also have large residual velocity magnitudes, indicating large velocity jumps characteristic for shocks. For instance, coherent structures in residual velocity field presented in R. I. Davies et al. (2009) which are associated with extended shocks, exhibit the LOS residual velocities of magnitudes 30 km s^{-1} or higher, corresponding to deprojected velocity magnitudes of $\sim$40 km s^{-1} or higher. These magnitudes are indicative of a nuclear spiral shock that causes a velocity jump of approximately 70 km s^{-1} between the minimum and maximum velocity as shown in W. Maciejewski (2004). As residual velocities describe the oscillations around the mean, their amplitude is half of the velocity jump. Furthermore, E. Athanassoula (1992) also resolves a velocity jump of $\sim$100 km s^{-1} when extended shocks are present, indicating deprojected velocity magnitudes around $\sim$50 km s^{-1} in extended shocks. In order to determine whether the coherent structures found in the velocity residual maps can be caused by extended shocks in gas, we examine the magnitude of velocity residuals in them. These results are presented in Section 5.1.2.

4.1.2 Coherent structures in maps of velocity difference between distinct emission lines

In Paper IV, we introduced a complementary approach to finding extended shocks in gas. It is based on the simple idea of subtracting the velocity fields of two different tracers. Thus in this approach, we construct **the velocity difference maps** by subtracting the LOS velocity of Hα from the LOS velocity of [N II]λ6583. For each galaxy, these are presented in Appendix A, and examples are given in the bottom right panel of Fig. 2 and in Fig. 4 for different galaxies. This method purely depends on the observed data and involves no contribution from kinematic or mass models. Therefore, the constructed velocity difference maps do not reflect artefacts from any underlying model and only highlight features present in the data.

This approach stems from the notion that the line profile recorded at any spaxel of a galaxy dataset is a convolution of emission from all regions of gas along the LOS towards this spaxel, and each region may have different physical conditions and may move with respect to the others. If physical conditions in these regions differ, then the relative contribution of each region to the emission along this LOS may differ between different emission lines. Thus, the integrated line profile, and therefore the LOSVD recorded in each spaxel may vary between the emission lines. As a result, the evaluated value of its first moment (velocity) may also differ depending on the tracer. Areas upstream and downstream of a shock in gas are a good example of two regions of gas that differ in physical conditions and move with respect to one another. As jump conditions in the shock impose a velocity difference between these two regions, for a spaxel which records emission from pre-shock and post-shock regions, the derived velocities may vary among the tracers. When extended shocks are present, then in many adjacent spaxels the velocity difference takes consistently

Downloaded from academic.oup.com/mnras/article/552/3/stag1204/8721813 by guest on 30 October 2026

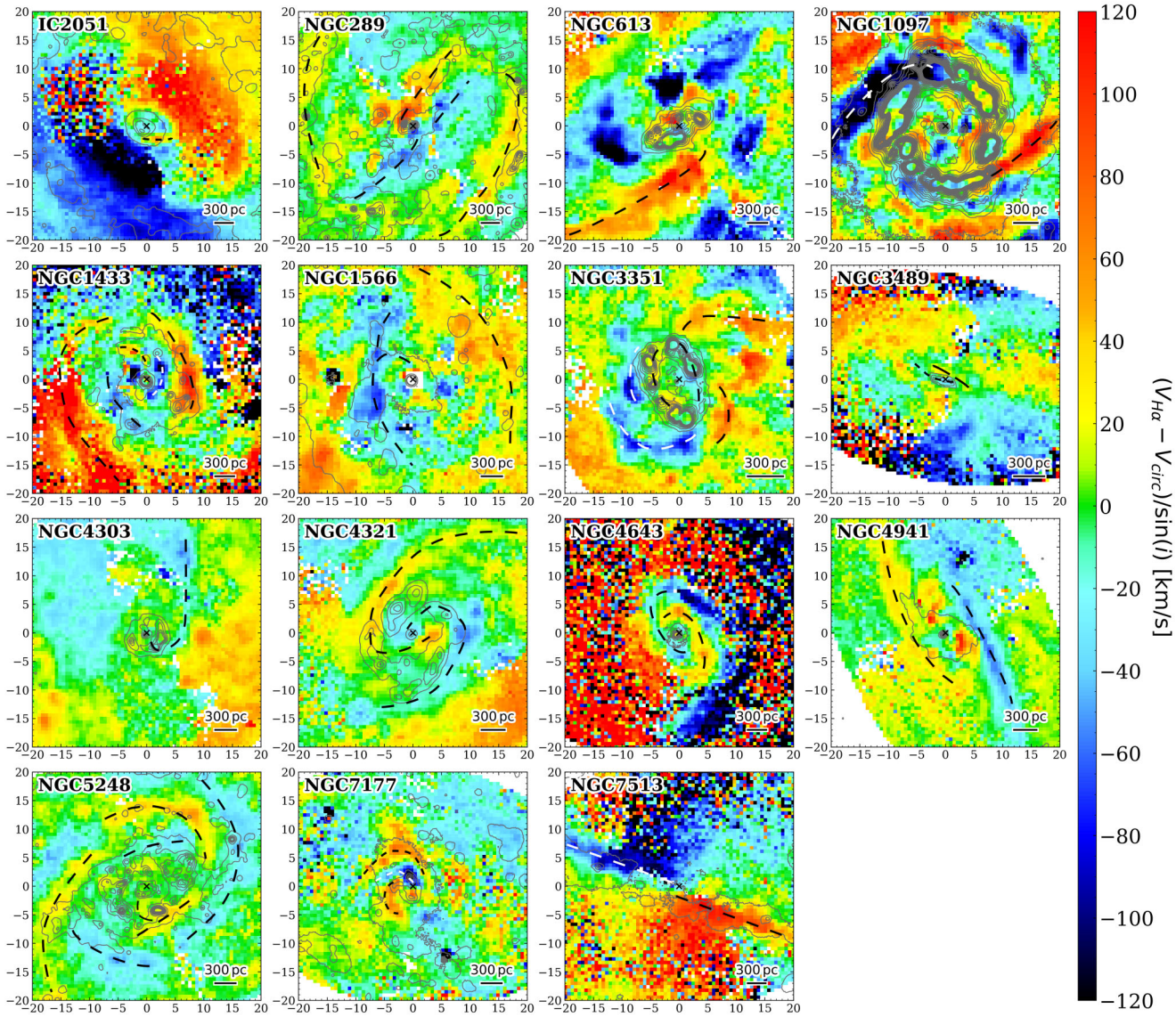

Figure 3. Residual velocity maps of galaxies exhibiting coherent extended structures (see Section 4.1.1). Spaxels with residual velocity measurements below 2σ significance are masked. The galaxy centres are marked with an 'x'. The dashed lines indicate the approximate locations of the extended kinematic features. The value of each spaxel is the average over 3×3 spaxels' box centred on it. The contours represent the Hα emission.

positive (or negative) values, and therefore extended shocks may give rise to continuous structures in velocity difference maps.

Note that when this scenario is applied to our data, the extended shocks will not always result in a velocity difference between the tracers. No velocity difference will be observed if different physical conditions in pre- and post-shock gas do not affect emission from the tracers, or if there is no significant difference in the LOS velocity between pre- and post-shock gas. Therefore, this method of finding extended shocks, although not dependent on galaxy models, can only be used in addition to other methods. In particular, velocity residuals, which are departures from circular motion in the disc plane, can be distorted in the presence of vertical motions, while the velocity differences do not assume a rotating disc. Note also that while the amplitude of the velocity residuals has a clear interpretation, interpreting the amplitude of velocity differences would require detailed modelling of emission from shock-excited plasma. Examples of extended structures found in velocity difference maps are outlined in Fig. 4 with dashed lines.

4.1.3 Determining the role of star formation and AGN using BPT maps

To complement the kinematic analysis explained in the previous sections, we study types of ionization mechanisms prevailing in the structures that we find in the central regions of galaxies. The diffuse ionized emission that we detect originates largely from the diffuse ionized gas, sustained by AGN, star formation (SF), and shocks in the turbulent interstellar medium (ISM). To distinguish the dominating source of ionization, such as AGN or star formation regions, from optical emission lines we constructed the Baldwin, Phillips, Terlevich (BPT) diagrams (J. A. Baldwin, M. M. Phillips & R. Terlevich 1981) for each galaxy within our sample. Each point on the BPT diagram corresponds to one spaxel

Downloaded from academic.oup.com/mnras/article/552/3/stag1204/8721813 by guest on 30 October 2026

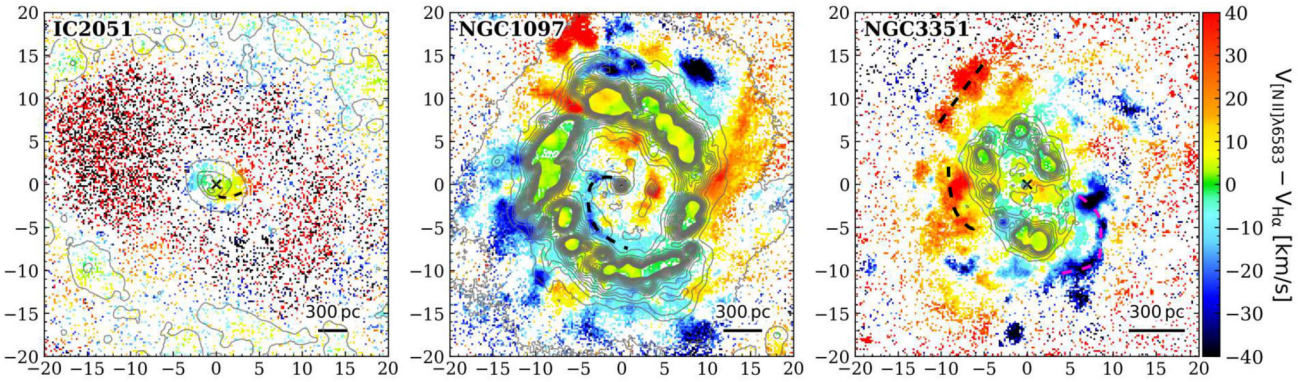

Figure 4. Velocity difference maps of galaxies exhibiting coherent extended structures. Spaxels with residual velocity measurements below 2σ significance are masked. The galaxy centres are marked with an 'x'. Dashed lines indicate the approximate locations of the extended kinematic features. Contours show the Hα flux distribution. These maps were used to support and refine the perturbation classifications assigned to the sample (see Sections 4.1.2 and 4.3).

in the data, and the position of each point is determined by fluxes measured for that spaxel. In order to exclude spaxels that are predominantly influenced by the noise, we implemented a threshold amplitude over noise (AON) (M. Sarzi et al. 2006) of Hβ, Hα, [N II]λ6583, and [O III]λ5007 emission lines. Spaxels with an AON for any of the four emission lines below the defined threshold were discarded. We avoid using the same AON value for all targets when constructing the BPT diagrams, as it could lead to a loss of spaxels with useful information if not applied carefully. Therefore, an arbitrary AON threshold is applied in order to prioritize a balance between maximizing the number of the displayed spaxels with information and minimizing noise levels in each map.

To differentiate between ionization driven by star-forming regions and AGN, we used the L. J. Kewley et al. (2001, hereafter Kewley+01) relation which indicates what line ratios can be produced by stellar photoionization, as for points above the Kewley+01 line emission likely originates from shocks or AGN. We note that the Kewley+01 relation does not account for the composite emission with ionization from both SF and AGN. Therefore, we also include the modified Kewley+01 line from G. Kauffmann et al. (2003, hereafter Kauffmann+03) relation, so that the region between Kaufmann+03 and Kewley+01 lines is the location of the composite emission, and the points below the Kaufmann+03 line show ionization from pure SF. We applied a further separation in the AGN region by using the R. Cid Fernandes et al. (2011) relation, which divides the region into two: low-ionization nuclear emission-line region (LINER) and Seyfert region.

As explained above, each point on the BPT diagram represents a spaxel in the data. These points are colour-coded according to their distance from the Kewley+01 line. We imposed the same colour-code on the spatial maps of galaxies, producing the **BPT maps** to highlight different ionization mechanisms in every location of each galaxy. Note that our BPT maps do not differentiate between LINER and Seyfert excitation, but the accompanying BPT diagram indicates which AGN excitation mechanism dominates overall. The BPT diagram and BPT map of each galaxy we studied in this work are presented in Appendix A, and examples of them are given in the bottom left panel of Fig. 2. Examining the velocity difference and residual velocity maps together with the BPT maps helps us in interpreting the origin of the observed coherent kinematic structures.

4.1.4 Studying the dust morphology in unsharp mask images

Gas and dust are generally well mixed in the interstellar medium, so large-scale shocks that compress the gas are also expected to compress and redistribute the dust along the same structure. In this context, the alignment of coherent kinematic structures with large residual velocity magnitudes and dust lanes strengthens the interpretation that extended shocks are present. In particular, when the kinematic signature appears fragmented or partially discontinuous, coherent dust lanes seen in unsharp-masked images can provide useful supporting evidence that separated kinematic segments may trace different parts of the same larger-scale shock structure, rather than unrelated local disturbances. However, it is important to note that dust morphology alone is not sufficient to build a definitive argument for the presence of extended shocks. This is because the coherent morphology of dust structures can also arise from the differential rotation, unrelated to shocks in gas.

To study the morphology of dust structures, we constructed **unsharp mask images** using a series of image processing techniques applied to MUSE images. Initially, we created red MUSE images by isolating emissions from redder wavelengths (∼7800–9350 Å). We then applied a Gaussian blur technique to the red images. This step is crucial as it reduces noise and smoothens the details in the images, enhancing the signal-to-noise ratio for subsequent analysis. For each galaxy, we adjusted the width of the Gaussian to emphasize dust structures within the innermost regions. While this application made inner dust structures clearer, it also weakened the visibility of dust lanes along the bars of galaxies, which ideally would require a wider Gaussian. Subsequently, we applied the unsharp masking technique, which involves subtracting the blurred version of the image from the original, to produce images that accentuate the edges and fine details of the dust structures.

Although this unsharp masking approach was not included in our pilot study of NGC 1097 in Paper IV, we examined there the dust structures inwards from the nuclear ring using a

Downloaded from academic.oup.com/mnras/article/552/3/stag1204/8721813 by guest on 30 October 2026

near-infrared (NIR) *J*-band image from M. A. Prieto et al. (2005). While for NGC 1097 we relied on NACO observations, such observations were not available for other galaxies of this sample. Therefore, to study dust structures in the remaining galaxies we used MUSE observations. Alongside other diagnostic maps, the unsharp mask image of each galaxy we studied in this work is presented in Appendix A, with an example given in the first panel of the third row of Fig. 2. The arrangement of Fig. 2, and of analagous figures in Appendix A for the remaining galaxies of the sample, allows the reader to identify structures common in different approaches and facilitates following of the analysis of individual galaxies.

4.2 Complementarity of approaches used to identify signatures of extended shocks

As explained in Section 4, we used various methodologies to reveal and study the coherent kinematic structures that might indicate the presence of shocks in gas. It is essential to emphasize that relying solely on one method might not be sufficient to definitively confirm or dismiss the presence of shocks.

For instance, in the residual velocity maps, which is the classical approach used in various other studies (e.g. K. Fathi et al. 2005, 2006; T. Izumi et al. 2013), some coherent kinematic structures may be artefacts of subtracting the model of circular disc with incorrect orientation (P. C. der Kruit & R. J. Allen 1978), and estimating the accurate orientation of a disc model might be challenging when global non-circular motions dominate the gas flow (see Paper IV). Such artefacts can obscure real coherent features present in the data. In addition, even in the absence of coherent kinematic structures in the residual velocity maps, shocks can still be deduced from extended regions of significant velocity difference between distinct emission lines, such as Hα and [N II]λ6583.

Even though we expect to see alignments between the structures observed in residual velocity maps and those in velocity difference maps, it is important to note that these two methods have different sensitivities to the vertical motion of the gas. The residual velocity maps depend on a model, which assumes gas in circular motion confined to a thin disc. This means that if the gas has some vertical motion, like in outflows, coherent structures may appear in the residual velocity map. However, if such outflow is seen in both Hα and [N II]λ6583 emission, no structures may be seen in the velocity difference maps. This effect is seen in the diagnostic maps of NGC 3351 (see Fig. A7). While the residual velocity map reveals the coherent 'L' shape structure of the transverse dust lane of the galaxy, which is associated with outflowing gas from the galaxy's nuclear ring (R. Leaman et al. 2019), this structure is absent in the velocity difference maps, which show a pair of red and blue lanes consistent with the classical picture of gas inflow in a bar.

As the velocity residuals and differences might be disguised in the presence of strong SF or AGN activity that dominates the velocity field, to complement our kinematic analyses, we studied the BPT map of each galaxy to pinpoint locations where gas kinematics may be affected by SF or AGN. However, we note that this approach can be limited if irradiation from the AGN dominates the central regions of the galaxies (see e.g. NGC 3489 in Appendix A9).

Finding coherent dust structures in the unsharp mask images can provide additional support for the existence of shocks, as shocks are expected to enhance the dust density. However, it is not expected for coherent structures seen in either residual velocity or velocity difference maps to align with dust structures over large azimuthal extents. This is because velocity projection convolves the in-plane velocity structure with a sinusoidal modulation along the azimuth, resulting in 'one-less' kinematic multiplicity of extended structures (B. Canzian 1993; R. H. M. Schoenmakers, M. Franx & P. T. de Zeeuw 1997). Thus for example a velocity jump in a two-arm morphological spiral will appear as a one-arm kinematic spiral of different pitch angle, hence the morphological and kinematic spirals cannot overlap over large azimuthal extents, despite well overlapping in e.g. bar lanes, which are mostly radial and therefore do not extend over large azimuth. We expect good alignment for structures extending up to 90° in azimuth. On the other hand, if the region has low optical depth (small amount of dust), the presence of continuous dust structure may not be apparent at all even when kinematic structures are evident.

Continuous dust structures can also originate from molecular clouds stretched by differential rotation, indicating that not all coherent dust filaments necessarily have a shock origin. One might also argue that dust obscuration in coherent filaments could produce coherent structures in residual velocity maps even in the absence of such structures in the actual gas velocity. This is possible in an optically thick disc, whose rotation depends on the height above the disc, because along the line of sight containing the dust structure emission may be dominated by regions located higher above the disc, and therefore rotating with different velocity. The velocity difference maps would not be affected by such obscuration as strongly as velocity residual maps since Hα and [N II]λ6583 are at similar wavelengths and would be affected similarly by the dust obscuration. Coherent structures in residual velocity maps caused by obscuration can closely resemble those resulting from shocks, including the misalignment caused by one-less kinematic multiplicity compared to the morphological one. However, the magnitude of coherent structures in residual velocity maps caused by dust obscuration should be rather small, proportional to the projected velocity difference at smaller and larger heights above the disc.

On the other hand, the magnitude of coherent structures in the residual velocity maps resulting from extended shocks can be large. For example, studying the observations of ionized gas, A. Zurita et al. (2004) revealed structures of extended shocks along the bar of galaxy NGC 1530, characterized by positive and negative residual velocities along the LOS with magnitudes up to 120 km s^{-1}. These magnitudes would correspond to even stronger shocks and larger velocity jumps along the galaxy's bar than those determined from models. Moreover, within the innermost regions of the NGC 1530, their residual velocity map reveals distinct structures, with positive and one with negative velocities, both with magnitudes of $\sim$40 km s^{-1}. These structures coincide with nuclear dust spirals visible in their $J-K$ colour images of the galaxy, and are interpreted as evidence of spiralling inflow to galaxy's nucleus. Their observational findings show an excellent alignment with their kinematic model of the gas flow and velocities along the dust spirals. Similar structures associated with spiral shocks and gas inflows to the nucleus, are also seen in other galaxies, such as NGC 5236 (K. Fathi et al. 2008) and UG 10200 (J. Blasco-Herrera et al. 2013), with residual velocity magnitudes of $\sim$30–50 km s^{-1}, and in NGC 3081 and NGC 1358 (A. Schnorr-Müller et al. 2016, 2017) with magnitudes of $\sim$50 km s^{-1}.

Our analysis highlights that not all diagnostic methods necessarily reveal extended shocks in gas simultaneously,

Downloaded from academic.oup.com/mnras/article/552/3/stag1204/8721813 by guest on 30 October 2026

emphasizing the importance of employing multiple complementary approaches when searching for such features. Although the residual velocity and velocity difference methods are each influenced by distinct factors, and a perfect spatial correspondence between their coherent structures is not always expected, in certain cases they exhibit good alignment. For instance, in NGC 4303 (see Fig. 2 and Appendix A12) both methods show aligning structures. The residual velocity map of NGC 4303 reveals a coherent structure extending continuously from the north to the south, exhibiting large deprojected velocities of approximately 50 km s^{-1}, downstream from the northern dust lane along the bar. This structure extends past the nuclear ring and directly reaches the nucleus of the galaxy. Similarly, the velocity difference map of the galaxy reveals a coherent structure that is almost spatially aligned with the one observed in the residual velocity map along the bar. These structures are associated with extended shocks in the gas.

4.3 Criteria for identifying extended shocks

As described in the previous sections, we use a combination of complementary diagnostics to identify and interpret signatures of extended shocks in the centres of galaxies. The residual velocity (Section 4.1.1) and velocity difference maps (Section 4.1.2) serve as the primary identification maps, since extended shocks are expected to produce coherent kinematic structures associated with rapid changes in velocity. However, because these two approaches are sensitive to different effects and need not reveal exactly the same structures, a candidate feature is not required to appear identically in both maps. Once we identify candidate extended kinematic features in one or both maps, we use the dust morphology (Section 4.1.4) and BPT maps (Section 4.1.3) to assess whether the feature is consistent with an extended shock and to interpret possible discontinuities, contamination, or alternative explanations.

Our criteria for identifying extended shocks are therefore as follows.

(i) **Initial identification in the kinematic maps.** We identify candidate signatures of extended shocks by examining the residual velocity and velocity difference maps for spatially extended, coherent features – as outlined in Figs 3 and 4. A candidate must be visible in at least one of these maps, while detection in both strengthens the identification. This approach accounts for the fact that the residual velocity map can be influenced by uncertainties in the disc model and by vertical motions, whereas the velocity difference map is model-independent and responds differently to gas traced by distinct emission lines but rarely produces strong signal. The identified features must be extended and elongated rather than compact or patchy. In practice, we look for quasi-linear or spiralling structures that can be traced across multiple adjacent spaxels – corresponding to at least is hundreds of parsecs – and whose length is clearly larger than their width. These structures may appear either as continuous features or as fragmented segments; in the latter case, they are retained if the segments plausibly trace a larger-scale structure based on their orientation, geometry, and overall continuity across the map.

(ii) **Velocity amplitude criterion.** Once a coherent extended kinematic feature has been identified, we examine its deprojected residual velocity to determine whether it is consistent with the magnitudes expected for shocks. Spatial coherence alone is not sufficient (see e.g. NGC 4237, Appendix A11): the feature should also show a velocity amplitude that is compatible with extended shocks. This criterion is essential because not all extended features in the kinematic maps correspond to shocks, whereas large residual magnitudes are expected for genuine shock signatures.

(iii) **Presence of a counterpart feature.** A particularly strong indication of an extended shock signature is the presence of a corresponding feature on the opposite side of the centre with an opposite velocity sign, as expected in shocks driven by bars or in nuclear spiral shocks (R. I. Davies et al. 2009). This is especially valuable when the candidate structure is not fully continuous, as paired features can support the interpretation that they trace a single large-scale shock-related pattern rather than unrelated local disturbances. However, this criterion is not always satisfied. The detectability of counterpart features depends on projection effects, the three-dimensional geometry of the system, and the complexity of the gas flows. Asymmetries in the gas distribution, local perturbations, or obscuration can result in only one side of the structure being clearly visible. Therefore, while the presence of a counterpart feature strengthens the classification, its absence does not preclude the identification of an extended shock signature.

(iv) **Support from dust morphology.** For candidate features, we also examine the unsharp-masked image for aligned dust lanes. Such alignment strengthens the interpretation in terms of extended shocks, since shocks are expected to compress gas mixed with dust. This is particularly useful in more fragmented cases, where the dust morphology can help assess whether disconnected kinematic segments are still part of a single larger-scale structure. However, dust morphology is used only as supporting evidence: dust lanes alone cannot demonstrate the presence of a shock, and agreement between dust and kinematic structures is not always expected because of projection effects and because coherent dust structures may also arise for reasons unrelated to shocks.

We apply the criteria above in the form of the following decision tree: a feature is considered a candidate for an extended shock when it appears as an extended coherent structure in at least one kinematic diagnostic map and exhibits deprojected residual velocities consistent with those expected for shocks. The presence of a counterpart feature strengthens the case. Features that satisfy only part of these conditions, or whose interpretation may be complicated by star formation or AGN, are treated more cautiously with the help of dust and BPT maps. Figs 3 and B3 present the deprojected residual velocity magnitudes for the galaxies in our sample. In Fig. 3, we highlight the features that we identify as extended, in Fig. B3 we present the kinematic maps in which we did not indentify extended features.

Once a kinematic structure has been identified, following the decision tree presented above, and associated with extended shocks, the BPT information provides additional physical context, helping to assess whether discontinuities in the structure coincide with star-forming regions or whether the observed kinematics may be influenced by AGN-driven outflows. In this sense, the BPT maps aid the interpretation of the nature and morphology of the candidate feature, but do not by themselves define the presence of an extended shock signature. Maintaining this distinction between identification (based on kinematics) and characterization (informed by ionization diagnostics) is essential, as BPT information is most powerful once the underlying kinematic structure has already been established. In this way, our decision tree combines model-dependent and model-independent kinematic diagnostics with supporting morphological and ionization

Downloaded from academic.oup.com/mnras/article/552/3/stag1204/8721813 by guest on 30 October 2026

information, while keeping the identification stage distinct from the characterization stage.

5 COLLECTIVE ANALYSIS OF GALAXIES IN THE SAMPLE

Each galaxy of our sample is analysed individually in its section of Appendix A, which gives the full set of kinematic maps, diagnostic maps, and images in figures analogous to Fig. 2, which we present here for the example of NGC 4303. A detailed explanation of each panel in these figures is provided in the beginning of Appendix A. These figures visualize the approaches that we take when identifying extended shocks, and the maps that we use for that. In this section, we gather the quantitative results of our analysis and provide an overview of our findings on the common kinematic characteristics observed in galaxies across our sample, based on their analyses provided in Appendix A.

5.1 Collected quantitative results for galaxies in the sample

5.1.1 Orientation of disc model for residual velocity fits

The parameters and approach taken to construct the disc model of each galaxy are individually provided in their respective sections in Appendix A. The PA of LON and i, derived for each galaxy using the appraoch given in Section 4.1.1, are summarized in Table 2, with the large-scale parameters provided for comparison.

Table 2. Large-scale and KINEMETRY-inferred disc orientation parameters. Superscripts denote the literature sources of the large-scale parameters.

	PA (deg)		Inc. (deg)	
Galaxy ID	Kinemetry	Large scale	Kinemetry	Large scale
IC 2051	60	72[a]	41	55[a]
NGC 289	125	130[b]	46	46[b]
NGC 613	110	115[c]	37	37[c]
NGC 1300	107	87[d]	35	35[d]
NGC 1433	19.7	19.7[e]	29	29[f]
NGC 1566	40	35[e]	37	31[f]
NGC 3351	23	10[f]	46	46[f]
NGC 3368	172	172[f]	46	50[f]
NGC 3489	80	71[f]	60	58[f]
NGC 3626	163	163[a]	53	47[a]
NGC 4237	107	106[g]	53	53[g]
NGC 4303	135	132[e]	42	23.5[e]
NGC 4321	155	152[h]	36	32[h]
NGC 4380	161	126[i]	59	56[i]
NGC 4457	80	66[i]	20	22[i]
NGC 4643	58	53[f]	43	38[f]
NGC 4941	25	21[j]	60	48[j]
NGC 5248	114	114[h,k]	44	45[h,k]
NGC 7177	90	83[f]	46	48[f]
NGC 7513	105	105[i]	46	46[i]

Note. Sources of large-scale parameters:
[a]H. Salo et al. (2015).
[b]W. Walsh, L. Staveley-Smith & T. Oosterloo (1997).
[c]E. Bajaja et al. (1995).
[d]P. A. B. Lindblad et al. (1997).
[e]P. Lang et al. (2020).
[f]P. Erwin, M. Pohlen & J. E. Beckman (2008).
[g]L. Chemin et al. (2006).
[h]S. Haan et al. (2008).
[i]J. C. Muñoz-Mateos et al. (2015).
[j]L. Gutiérrez et al. (2011).
[k]S. Haan et al. (2009).

5.1.2 Determination of velocity jumps in shocks

In order to ensure that the coherent structures seen in the residual velocity maps are indeed due to extended shocks, we examined the deprojected residual velocity magnitudes in these structures. Working under the assumption that the gas moves in the plane of the galaxy disc, we obtain the deprojected velocities using the formula $V_{\rm true} = V_{\rm LOS}/sin(i)$, where $V_{\rm true}$ is the deprojected velocity, $V_{\rm LOS}$ is the observed LOS velocity, and i is the inclination angle of the galaxy. We record the highest and lowest magnitudes, for both positive and negative velocities, along the coherent structures, which could indicate extended shocks. To reduce the level of noise in the residual velocity maps we applied box filter convolution, so that the value at each spaxel is the average over 3×3 spaxels' box centred on it. Maps of the deprojected residual velocity, created following this approach, are presented in Fig. 3 for a subset of galaxies for which extended structures are detected and in Appendix B, Fig. B3 for the remaining galaxies. The recorded velocity magnitudes in extended structures are explicitly stated for each galaxy in their respective sections in Appendix A, and also listed in Table 3. For completeness, in this table we also included the target of our pilot study, NGC 1097.

In the majority of galaxies that we studied, the highest deprojected residual velocity magnitudes, recorded along the coherent structures associated with extended shocks, are $\sim$50 km s^{-1} or higher. These magnitudes are similar to the magnitudes observed in other galaxies, which are associated with spiral shocks extending to the nucleus (A. Zurita et al. 2004; K. Fathi et al. 2008; R. I. Davies et al. 2009; J. Blasco-Herrera et al. 2013; A. Schnorr-Müller et al. 2016, 2017). Particularly, for galaxies like NGC 1433 and NGC 4643, the deprojected velocity magnitudes exceed 100 km s^{-1}, indicating much stronger shocks and larger velocity jumps, even larger than the jumps of $\sim$100 km s^{-1} seen in models by E. Athanassoula (1992) and of $\sim$70 km s^{-1} by W. Maciejewski (2004).

On the other hand, the coherent structures observed in the residual velocity maps of the two unbarred galaxies in our sample, NGC 4237 and NGC 4380, have deprojected velocity magnitudes of only 20 km s^{-1}. This indicates that these structures are either caused by obscuration (see Section 4.2) or by a low-amplitude wave propagating in gas, below the threshold of steepening into a shock. This amplitude of the velocity residual is several times smaller than the magnitudes seen in the other galaxies of our sample (see also Fig. 7).

Note that in the majority of galaxies that we studied, the lowest residual velocity magnitudes recorded along the coherent kinematic structures associated with extended shocks, have values similar those in the unbarred galaxies of our sample. This may indicate that in the regions where we recorded the lowest magnitudes, the shocks wane into mere waves propagating in gas, but this can also be the effect of noise in the data, still noticeable after binning.

5.1.3 Radial extent of the shocks

For each galaxy in which signatures of extended shocks are identified, Appendix A describes in detail how deeply inwards and

Downloaded from academic.oup.com/mnras/article/552/3/stag1204/8721813 by guest on 30 October 2026

Table 3. The individual findings for the sample galaxies studied in this work. Columns: (1) index used in figures to represent each galaxy; (2) galaxy ID; (3) nuclear emission type (see Section 5.4); (4) kinematic category (see Section 5.3); (5) ranges of deprojected galactocentric radii of the signatures associated with extended shocks (see Section 5.1.3); (6) minimum and (7) maximum positive/negative deprojected velocity magnitudes in extended structures (see Section 5.1.2); (8) average Hα velocity dispersion (Section 6.3.1); (9) inner bar presence; (10) nuclear ring presence – 'N': absence, 'Y': presence, 'Y?': potential presence, '?': uncertain classification.

Index (1)	Galaxy ID (2)	Nuclear emission (3)	Kinematic (km s^{-1}) (4)	Radial range (pc) (5)	Min vel. (km s^{-1}) (6)	Max vel. (km s^{-1}) (7)	$<\sigma>$ (km s^{-1}) (8)	Inner bar (9)	Nuclear ring (10)
1	IC 2051	Composite	Ext. Shocks	320–820	−15, 20	−40, 65	75.7 ± 3.8	N	Y
2	NGC 289	Composite	Ext. Shocks	300–2150	−20, 15	−65, 90	72.4 ± 0.9	N	N
3	NGC 613	Composite	Ext. Shocks+Outflow	650–3010	−30, 40	−90, 110	101.1 ± 5.6	N	Y
4	NGC 1097	LINER	Ext. Shocks	100–2660	−50, 40	−130, 150	80.7 ± 4.6	Y	Y
5	NGC 1300	LINER	Other Perturb.	–	–	–	70.5 ± 3.8	N	Y
6	NGC 1433	LINER	Ext. Shocks	140–2160	−20, 25	−116, 115	74.6 ± 3.0	Y	Y
7	NGC 1566	–	Ext. Shocks	480–1860	−20, 20	−80, 70	100.4 ± 11.4	Y?	Y?
8	NGC 3351	SF	Ext. Shocks	270–560	−25, 12	−95, 50	81.0 ± 9.7	N	Y
9	NGC 3368	LINER	Other Perturb.	–	–	–	103.8 ± 1.9	Y	N
10	NGC 3489	Seyfert	Ext. Shocks	140–880	−12, 8	−40, 30	69.8 ± 1.0	N	?
11	NGC 3626	LINER	Other Perturb.	–	–	–	74.0 ± 4.2	Y	N
12	NGC 4237	Composite	Unperturbed	–	−5, 5	−20, 18	54.1 ± 0.2	N	N
13	NGC 4303	LINER	Ext. Shocks	120–2200	−15, 10	−50, 20	69.3 ± 4.2	Y	Y
14	NGC 4321	LINER	Ext. Shocks	130–2390	−15, 15	−55, 55	66.9 ± 1.9	Y	Y
15	NGC 4380	LINER	Unperturbed	–	−4, 9	−13, 20	53.7 ± 0.3	N	Y?
16	NGC 4457	LINER	Other Perturb.	–	−35, 45	−125, 120	86.4 ± 1.3	Y	N
17	NGC 4643	LINER	Ext. Shocks	130–2070	−20, 20	−110, 70	71.2 ± 0.6	N	N
18	NGC 4941	Seyfert	Ext. Shocks + Outflow	620–3320	−20, 15	−60, 45	95.3 ± 11.8	Y	N
19	NGC 5248	Composite	Ext. Shocks	90–2830	−15, 20	−50, 60	62.6 ± 1.5	N	Y
20	NGC 7177	Composite	Ext. Shocks + Outflow	150–1100	−15, 20	−70, 60	82.5 ± 1.2	N	N
21	NGC 7513	LINER	Ext. Shocks	100–2080	−30, 30	−80, 100	59.3 ± 0.5	N	N

how far outwards the shock signatures can be traced within the disc. Table 3 (fifth column) summarizes the smallest and the largest deprojected galactocentric radii of these features, converted to physical units (pc) using the distance to each galaxy.

The deprojected radii listed in the fifth column of Table 3 shows that extended shock signatures are detected across large radial ranges, reaching inward to radii below 100 parsecs, and extending out to more than 3 kpc, in some cases to the edge of the MUSE FOV. In most systems, the furthest radii lie between $\sim$ 1 and 3 kpc, demonstrating that the shocks often reach well into the galactic disc, with several galaxies – most notably NGC 613, NGC 4303, NGC 4321, NGC 4941, and NGC 5248 – showing shock-related features beyond 2 kpc.

The smallest galactocentric radii of extended shocks signatures indicate that these structures can penetrate deep into the inner regions: in 7 galaxies they are around 100 pc, the value similar to the typical resolution of the observations. In three galaxies in our sample – NGC 613, NGC 4457, and NGC 4941, strong outflows from the AGN obscure the features within the innermost regions of the diagnostic residual velocity and velocity difference maps. Consequently, the signatures of extended shocks in these galaxies cannot be traced further inwards to the same radii as in the systems without strong AGN outflows, and the measured closest radii – typically around $\sim$ 600 pc – likely underestimate how close to the galactic nucleus the shocks in these galaxies actually extend. Moreover, we note that the innermost few arcseconds of NGC 1566 are discarded due to saturated spaxels and the signatures of extended shocks in this galaxy extend down to 480 pc, which is also likely underestimated. In the remaining three galaxies – IC 2051, NGC 289, and NGC 3351 – whose central regions do not appear affected by the AGN outflows, extended shocks reach inward only to $\sim$300 pc. In these three galaxies the innermost radius at which shocks can be reliably traced coincides with the location of the nuclear rings, suggesting that the rings may act as a structural barrier that prevents shock signatures from propagating further into the nucleus.

5.2 Common features seen across the sample

One of the striking examples of shocks in gas that yield inflows to the galactic nucleus is revealed within the kinematic fields of NGC 5248 (see Fig. 3, last row/first panel and Fig. A18). The residual velocity map of that galaxy exhibits a coherent continuous structure, manifested as a spiral pattern with a red (with positive velocities) and a blue (with negative velocities) arm. These structures appear as counterparts of one another, with a pattern that is almost a textbook example of extended shocks in gas, similar to those expected from models (R. I. Davies et al. 2009). Inner to the star-forming ring of the galaxy, the observed structures become more patchy yet there are indications of some parts of these structures extending to the innermost regions. Similar counterpart structures with positive and negative velocities, extending over large range of radii are also seen in the residual velocity maps of NGC 1566, NGC 4321, NGC 4643, and NGC 7513 (see Figs 5, A11, A16, and A20). In these galaxies, the coherent continuous structures exhibit large deprojected residual velocity magnitudes ranging approximately from 60 to 100 km s^{-1}. The residual velocity map of NGC 4303, shown in Fig. 2, also reveals a coherent structure, extending continuously from the north of the frame southwards, exhibiting large deprojected velocities of approximately 50 km s^{-1}, downstream from the northern dust lane along the bar. However, there is no clear counterpart with positive velocities.

Downloaded from academic.oup.com/mnras/article/552/3/stag1204/8721813 by guest on 30 October 2026

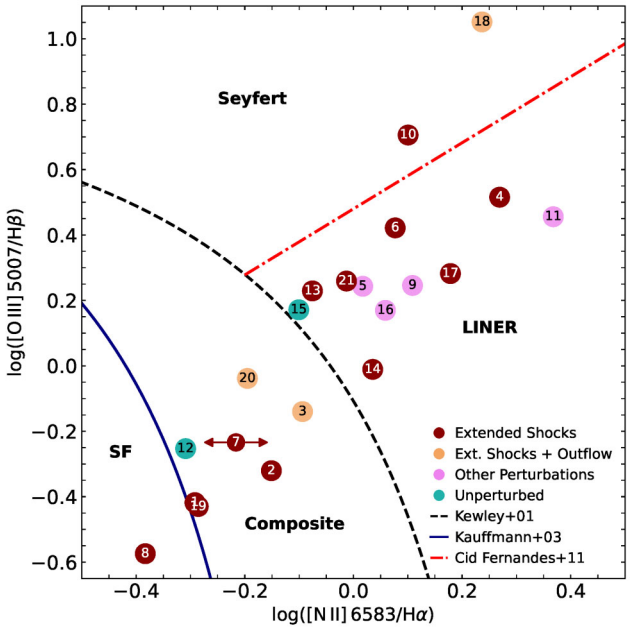

Figure 5. The BPT diagram of the galaxy sample analysed in this study, computed using integrated emission-line flux ratios within 150 pc radius. The navy (solid), black (dashed), and red (dot–dashed) lines show G. Kauffmann et al. (2003), L. J. Kewley et al. (2001), and R. Cid Fernandes et al. (2011) fits, respectively. These lines determine the regions associated with different ionization mechanisms: SF, Composite, LINER, and Seyfert. Each point in the diagram represents an individual galaxy, with the accompanying numbers listed in the index column of Table 3 for identification. The points are colour-coded as described in the legend according to the categories assigned based on the extended shock signatures.

In some galaxies, such as IC 2051 and NGC 3489, see Figs A1 and A9, the resolution of structures in central regions is limited due to galaxy distance and the inclined geometry of the system. However, we can discern aligning structures across our multiple approaches, exhibiting large deprojected velocity magnitudes around $\sim$50 km s^{-1}, that are indicative of extended shocks.

Within the inner kpc region of some galaxies, such as in NGC 289, NGC 1433, and NGC 3351, several extended structures are observed in the residual velocity map, exhibiting deprojected velocity magnitudes of 90 km s^{-1} or higher (see Figs A2, A5a, and A7, respectively). However, unlike those seen in NGC 5248, these structures do not extend continuously from the outer regions of the galaxy towards the nucleus. Instead, they appear as discontinuous pieces. For instance, the extended structures in NGC 1433 are located within the nuclear disc, where strong SF occurs. These structures mostly are located downstream from the curving dust lanes in the nuclear disc. In NGC 3351, these structures are found in and inner to the nuclear ring and just outside it, where strong SF and stellar outflows occur. Similarly, the structures in the central regions of NGC 289 are also located in areas dominated by SF. In all there galaxies, where extended structures occur in the residual velocity map, the velocity differences also show enhancements. In these three galaxies, continuous dust lanes extend from the outer regions towards the nucleus, while kinematic structures are rather discontinuous. Based on the alignments across multiple methodologies, we associate the observed discontinuous yet extended structures with extended shocks in the gas. We hypothesize that due to strong star-forming activities, the self-gravity of the gas is strong enough to disrupt the continuity of extended shocks in the gas, leaving behind disconnected pieces. In contrast, the dust is less affected by these disturbances and maintains its spiral form as it propagates towards the nucleus.

The kinematics within the innermost regions of three galaxies in our sample, namely NGC 613, NGC 4941, and NGC 7177 are strongly dominated by AGNs. This dominance is primarily evident in the velocity dispersion and BPT maps of these galaxies (see Appendix A3, A17, and A19). The residual velocity maps of these galaxies exhibit extended shock signatures in their bar regions, with large deprojected velocity magnitudes ranging from roughly 60 to 100 km s^{-1}. However, strong AGN outflows which are dominating the kinematics in the innermost regions, prevent the tracing of shock signatures to the nucleus.

Furthermore, the kinematic fields of several other galaxies in our sample, namely NGC 1300, NGC 3368, NGC 3626, and NGC 4457, shown in Figs A4, A8, A10(a), and A15 respectively, are strongly disturbed, but we cannot associate them with any mechanism of inflow. They seem rather related to AGN or stellar outflows, or we cannot identify the source of the disturbance. Standing as one of the most intriguing galaxies within our sample is NGC 3626. Throughout the observed region, the gas counter-rotates with respect to the stars, yet the gas reaching the central regions collapsed to form a boxy ring structure within the inner $\sim$15 arcsec (see Appendix A10). However, the origin and motion of gas in this galaxy are complex and there is no evidence of extended shocks to the nucleus.

Lastly, the only two unbarred galaxies in our sample, NGC 4237 and NGC 4380, have relatively unperturbed kinematic fields and show no evidence of extended shocks. Their residual velocity maps typically exhibit low deprojected velocity magnitudes, not exceeding $\sim$20 km s^{-1}. No prominent structures are seen in the velocity difference maps either. These results suggest the absence of shocks in these systems. Any mild perturbations may instead arise from obscuration effects, variations in velocity with height, or wave patterns generated by lopsidedness.

5.3 Grouping of galaxies based on the observed signatures of extended shocks: prevalence of shocks in the sample

As we noticed in Section 5.2, the individual examinations of each galaxy (presented in Appendix A) reveal similar patterns in several cases. This allowed us to classify the galaxies into four distinct categories, based on the extended shock signatures identified from their diagnostic maps. We further refer to this classification as the *kinematic category*.

The first kinematic category is defined as ***extended shocks***. Galaxies in this category exhibit compelling shock signatures that extend over large distances into the inner parsec regions and are characterized by high residual velocities or significant velocity differences. These extended shock signatures can appear as coherent continuous structures, spanning inwards either in a straight (see e.g. NGC 4941 in Fig. 3) or spiralling pattern (see e.g. NGC 5248 in Fig. 3), or as more discontinuous structures that nevertheless remain consistent with extended shocks. In some galaxies, these structures can be traced continuously over large scales, while in others they appear more fragmented, possibly due to strong local activity disrupting the propagation of the shocks. Even in such cases, they are still characterized by high residual velocities and/or large velocity differences, and often follow the continuous dust patterns that

Downloaded from academic.oup.com/mnras/article/552/3/stag1204/8721813 by guest on 30 October 2026

can be associated with loci of shock compression. We classified 12 galaxies in our sample as showing extended shocks: IC 2051, NGC 289, NGC 1097, NGC 1433, NGC 1566, NGC 3351, NGC 3489, NGC 4303, NGC 4321, NGC 4643, NGC 5248, and NGC 7513.

The second category is ***extended shocks and outflows*** . Although galaxies in this category exhibit extended shock signatures along their bar, within the innermost regions the kinematics are obscured by strong outflows from AGNs, preventing the tracing of shock signatures to the nucleus (see e.g. NGC 613 in Fig. 3). We classified three galaxies in our sample under this category: NGC 613, NGC 4941, and NGC7177.

The third category, defined as ***other perturbations*** , includes galaxies that do not exhibit compelling signatures of extended shocks associated with inflow. However, the kinematic fields of these galaxies are strongly perturbed. In most of these galaxies, the perturbations within inner kpc can be associated with local shocks from SF and/or AGN. We classified four galaxies in our sample as having other perturbations: NGC 1300, NGC 3368, NGC 3626, and NGC 4457.

The final category is defined as ***unperturbed*** . Galaxies under this category have relatively unperturbed kinematic fields and show no evidence of extended shocks. The residual velocity maps typically exhibit perturbations with low amplitudes. We classified two galaxies in our sample as unperturbed: NGC 4237 and NGC 4380. It is important to note that although both *other perturbations* and *unperturbed* categories include galaxies without shock signatures, galaxies within the former category have significantly perturbed kinematic fields, unlike the galaxies in the latter category. The kinematic category assigned to each galaxy in the sample we studied in this work is presented in the third column of Table 3.

The grouping above indicates that 57 per cent (12 out of 21) of the galaxies in our sample, including NGC 1097 from Paper IV, exhibit signatures of extended shocks within their inner kpc region which can be traced to the innermost parsecs. In contrast, 29 per cent of the galaxies (6 out of 21) do not show such signatures, with 2 of these galaxies displaying unperturbed kinematic fields. For the remaining $\sim$ 14 per cent (3 out of 21), coherent structures with large deprojected residual magnitudes are observed along the bars, but AGN outflows obscure the innermost regions, preventing us from tracing these structures further. As a result, the 57 per cent figure may be a lower limit, as extended shocks could be reaching the nucleus in those 3 galaxies, but they are obscured by the dominating outflows. Therefore, this significant proportion – at least 57 per cent – suggests that extended shocks could be the prevalent mechanism of gas inflow in the central regions of galaxies in our sample.

5.4 Grouping of galaxies based on the nuclear emission type

We further categorized the galaxies in our sample based on the dominant emission type in their nuclear regions, to explore the correlation between the type of nuclear emission and the presence of extended shocks. In Fig. 5, we present the ***BPT diagram of the sample***. Each point on the diagram represents a single galaxy, colour-coded according to the kinematic category assigned based on the signatures of extended shocks identified in each. The location of each point on the BPT diagram is determined by the ratio of emission line fluxes measured within a 150 pc radius. The diagnostic lines based on relations from L. J. Kewley et al. (2001), G. Kauffmann et al. (2003), and R. Cid Fernandes et al. (2011) separate the regions for SF, Composite, LINER, and Seyfert nuclear emission type as in Section 4.1.3. This classification is used for identifying the main ionization source in the nucleus of each galaxy.

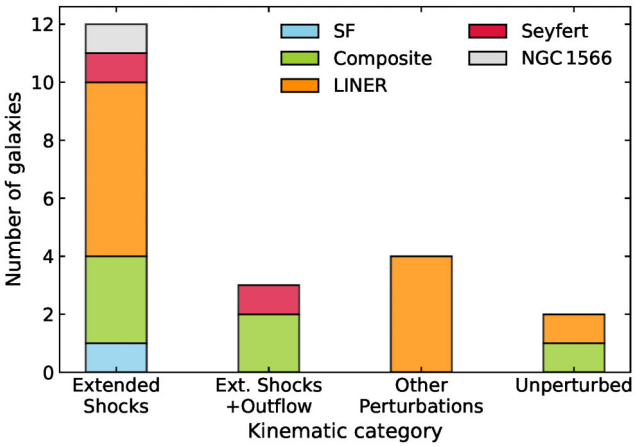

Figure 6. The distribution of galaxies stacked in each kinematic category, colour-coded based on their nuclear emission types, both classifications are defined in Sections 5.3 and 5.4. Different colours represent SF in blue, composite emission in green, LINER in orange, and Seyfert in red. NGC 1566, which has an uncertain nuclear emission type, is represented in grey.

Consequently, based on the BPT diagram of the sample, we have assigned a nuclear emission type to each galaxy, which are presented in the third column of Table 3. We note that, because of strong broad emission from its AGN, NGC 1566 had unreliable Hα and [N II]λ6583 flux measurements within its inner $\sim$1 arcsec but the flux measurements of [O III]λ5007 and Hβ were not significantly affected. Therefore, to represent the uncertainty in the x-axis position of this galaxy on the BPT diagram of the sample, we have marked its location with two horizontal arrows, indicating its position could shift either to the left or right. While previous studies have classified this galaxy as Seyfert/LINER type (e.g. D. Alloin et al. 1985; J.-H. Woo & C. M. Urry 2002), we have decided not to assign a nuclear emission type obtained from other works to ensure consistency across the galaxies analysed in this study based on the BPT diagram of the sample.

In Fig. 6, we present the distribution of galaxies in our sample grouped by kinematic category. The colour-coding indicates the nuclear emission type assigned to each galaxy. We find no clear correlation between the nuclear emission types derived from the BPT diagram and the kinematic categories defined by the presence of extended shock signatures in the galaxies we studied. This lack of correlation is not surprising given the mismatch in characteristic time-scales: transporting gas from kpc scales to the central $\lesssim$10$-$100 pc typically requires $\sim 10^7 - 10^8$ yr (e.g. P. F. Hopkins & E. Quataert 2010; L. A. Silva-Lima et al. 2022), whereas AGN activity is expected to be highly intermittent, with 'flickering' on much shorter time-scales of order $\sim 10^5$ yr (e.g. K. Schawinski et al. 2015). Such variability can therefore wash out any contemporaneous correspondence that might otherwise be expected. Additionally, the small sample size may further limit our sensitivity to subtle trends.

Downloaded from academic.oup.com/mnras/article/552/3/stag1204/8721813 by guest on 30 October 2026

6 CORRELATIONS BETWEEN THE OBSERVED QUANTITIES AND OTHER PROPERTIES OF THE HOST GALAXIES

In Section 5, we classified galaxies in our sample according to their gas kinematics in the central kpc region, as well as the type of nuclear emission deduced from the same data. We found no obvious correlations between classes in the two groupings. However, correlations are expected between other properties of the host galaxies and their gas dynamics and nuclear activity. For example, one expects from dynamical considerations that bars in galaxies should stir gas, leading to shocks and disturbed kinematics, as well as to some nuclear activity, though whether this means nuclear star formation or feeding of the active nucleus remains being disputed. With the size of our sample, we can not only test those hypotheses, but we are also able to look for other correlations of the observed gas and shock parameters with e.g. the galaxy mass or the presence of other morphological features. Below we report on what correlations we found, their confidence level, their possible physical reasons, and their implications for gas flow in galaxies.

6.1 The correlation between the kinematic category and the presence of large-scale bars

One of the strongest observational findings of our analysis is that the two galaxies in our sample that have unperturbed kinematics, NGC 4237 and NGC 4380, are also the only two unbarred galaxies in our sample. Unlike the other galaxies we studied, these two galaxies exhibit very regular kinematic fields and they lack extended shock signatures. When attributed to their unbarred morphology, this observation confirms the significance of bars, causing perturbation in the discs, driving extended shocks and facilitating gas inflows to the nucleus. Although this conclusion is based on only two galaxies, statistically it appears significant, as with 2 unperturbed galaxies in a sample of 21, the likelihood of randomly selecting an unperturbed one is 2/21, and if the presence of bar were unrelated to unperturbed gas kinematics, the likelihood of two unbarred galaxies displaying by chance unperturbed kinematics would be $(2/21)^2 = 0.9$ per cent.

Note that having only two unbarred galaxies in a sample of 21 is not representative of the population: according to P. Erwin (2018), in a sample of galaxies with stellar masses $\sim 10^{10-11} M_\odot$, approximately 60 per cent are barred, so the remaining ∼40 per cent are unbarred. Taking this as a probability distribution, one might expect to find around 8 unbarred galaxies in a sample of 21, and the likelihood of having only 2 is 0.2 per cent. There are two sources of this discrepancy. First, in the original complete CBS sample of 53 galaxies, only 25 per cent are unbarred. This fraction is slightly reduced to 22 per cent when one limits the sample to 46 galaxies observed with MUSE. However, when the sample is further limited to galaxies with sufficient emission-line signal, this fraction drops to 12 per cent: only 20 per cent (2 out of 10) of unbarred galaxies in the subsample observed by MUSE have emission-line signal above our threshold, while among barred galaxies 47 per cent (17 out of 36) do.

Therefore, our analysis implies that in the CBS sample observed by MUSE, in which the fraction of barred galaxies is not far off the general population, 47 per cent of barred galaxies show gas emission in their central kpc sufficient for gas dynamics to be characterized, and in all cases this is a disturbed gas dynamics. On the other hand, in the same sample, only 20 per cent of unbarred galaxies show gas emission in their central kpc sufficient for gas dynamics to be characterized, and in all cases this dynamics is unperturbed.

6.2 Correlations with the presence of inner bars and nuclear rings

Inner bars and nuclear rings play important roles in the transport of gas to the nucleus. While inner bars are seen as one of the primary mechanisms of inflow to the nucleus of galaxies (I. Shlosman et al. 1989; I. Shlosman 2001; P. Martini et al. 2003; D. Namekata et al. 2009; Z. Li et al. 2023; A. Lorenzo-Cáceres, J. Falcón-Barroso & A. Vazdekis 2013), nuclear rings are typically seen as barriers of gas transport to the nucleus, as the inflowing gas accumulates in them (B. G. Piner, J. M. Stone & P. J. Teuben 1995; K. Sheth et al. 2005; M. C. Sormani et al. 2015).

In this section, we explore the correlation between the presence of extended shocks and the occurrence of inner bars and nuclear rings as identified within CBS. The CBS sample spans a diverse range of galaxies and is designed to consistently extract central stellar structures, including nuclear star clusters (A. Ashok et al. 2023), inner bars, and nuclear rings. Table 3 indicates whether the galaxies studied here host inner bars or rings, based on the CBS classification, which is carried out using a combination of isophotal ellipse fitting, unsharp masking, and visual inspection of optical and near-IR images (P. Erwin et al. 2021; P. Erwin 2024). Unsharp masking is particularly valuable for confirming weak inner bars and for distinguishing them from nuclear spirals, discs, or rings, while optical imaging highlights the dust and star formation that reveal nuclear rings. Nuclear rings are further classified as star-forming, stellar, or dusty, depending on their colours, morphology, and associated emission features. While methodological details are discussed in P. Erwin et al. (2021) and P. Erwin (2024), further refinements to the measurements of CBS galaxies will be presented in the forthcoming CBS publication.

6.2.1 The correlation between the nuclear emission type and the presence of inner bars

Amongst the 21 galaxies of our sample, 8 have inner bars, while 12 do not show an evidence of one. One galaxy, namely NGC 1566, exhibits a potential presence of an inner bar. Because of this uncertainty, this galaxy is excluded from further statistical analysis. Therefore, the total number of galaxies considered for examining the correlation between the presence of extended shocks and inner bars is 20. Fig. 7 presents the fraction of galaxies in each kinematic category, separated according to the presence or absence of inner bars. Each galaxy is colour-coded according to the nuclear emission type derived from the BPT diagram shown in Fig. 5.

Although the distribution of galaxies among kinematic categories does not seem to depend on whether the galaxy hosts an inner bar or not, Fig. 7 reveals that all 8 galaxies with inner bars exhibit either LINER or Seyfert emission dominating their inner 150 pc. Noticeably, no galaxies with inner bars have their innermost 150 pc dominated by star formation or show composite emission in that region. On the other hand, the nuclear emission in the remaining 12 galaxies that do not have inner bars spans all categories: we classify 6 of those galaxies as composite, 5 as Seyfert/LINER, and 1 as star-forming. Overall, there are 13 galaxies classified Seyfert/LINER in our sample of 20 galaxies. If we assume that the probability of showing a Seyfert/LINER emission by a galaxy from our sample is 13 out of 20, and that

Downloaded from academic.oup.com/mnras/article/552/3/stag1204/8721813 by guest on 30 October 2026

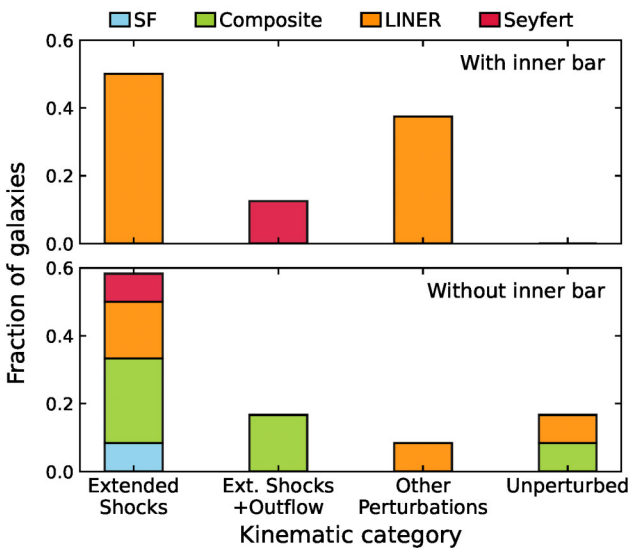

Figure 7. The fraction of galaxies in each kinematic category, grouped by the presence (top) and absence (bottom) of inner bars. The colours represent different nuclear emission types assigned to galaxies based on the BPT diagram of the sample: SF in blue, composite in green, LINER in orange, and Seyfert in red.

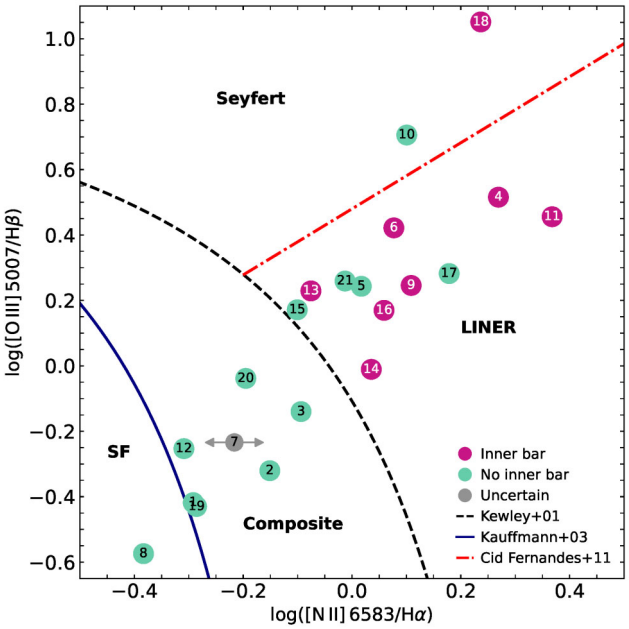

Figure 8. The BPT diagram for the galaxy sample analysed in this study, constructed using integrated emission-line flux ratios within a 150 pc radius. The demarcation lines, identical to those in Fig. 5, indicate the regions corresponding to different ionization mechanisms: SF, Composite, LINER, and Seyfert. The numbers assigned to each galaxy correspond to the indexes shown in Table 3. Each point is colour-coded to indicate the presence (pink), absence (green), or uncertain (grey) classification of inner bars in the respective galaxies.

this probability is independent of whether the galaxy is hosting an inner bar, then the likelihood of all 8 galaxies in the subsample with an inner bar showing Seyfert/LINER emission is $(13/20)^8 \simeq 3$ per cent. In other words, with 97 per cent confidence we can say that the distributions of nuclear emission types for galaxies with and without inner bars differ: galaxies with inner bars are more likely to display Seyfert/LINER nuclear emission.

Different distributions of galaxies with and without inner bars are evident in the Global BPT diagram for our sample presented in Fig. 8 (see Section 5.4 for an explanation of the diagnostic lines), colour-coded by the presence or absence of inner bars: galaxies hosting inner bars are found exclusively in the LINER or Seyfert regions of the diagram, with none occupying the star forming or composite regions. By contrast, galaxies without inner bars span the full range of emission types. There is a clear trend in the diagram, where at low line ratios, only galaxies without inner bar are present, while galaxies with inner bar start appearing at intermediate line ratios, and eventually dominate at the highest line ratios. The BPT diagram therefore provides a clear visual confirmation of the trend that inner bars are associated with AGN-like nuclear emission.

Although the trend that we found does not imply that inner bars drive inflow to the galactic nuclei, it suggests that inner bars may inhibit star formation in the innermost regions, which in galaxies without inner bars can proceed unsuppressed.

6.2.2 The correlation between the kinematic category and the presence of nuclear rings

Amongst 21 galaxies in our sample, 9 galaxies host nuclear rings, while another 9 galaxies do not. As for the remaining three galaxies, two of them are classified as potentially having a nuclear ring, one of them being NGC 1566, which also has an uncertain nuclear emission type, and for one galaxy (marked with a '?' in the nuclear ring column of Table 3), the presence of a nuclear ring has not been verified. Since these three galaxies do not provide the presence of nuclear rings confidently, we exclude them from our statistical analysis and description. Therefore, the total number of galaxies we consider when examining the correlation between the presence of nuclear rings and extended shocks is 18.

Fig.9 presents the fraction of galaxies in each kinematic category, grouped by the presence (top) and the absence (bottom) of nuclear rings within their inner kpc. As in Fig. 7, the colours represent galaxies with different nuclear emission types. While, contrary to what we found in the case of inner bars, we find no significant correlation between the presence of nuclear rings and the nuclear emission type, the distribution of galaxies among kinematic categories seen Fig. 9 appears to depend on whether the galaxy hosts a nuclear ring or not, again contrary to the case of inner bars seen in Fig. 7. Approximately 78 per cent of galaxies (7 out of 9) with nuclear rings are classified under in *extended shocks* category. On the other hand, the fraction of galaxies *without* nuclear rings in the same category is low, approximately 33 per cent (3 out of 9). Moreover, $\sim$ 33 per cent (3 out of 9) of galaxies without nuclear rings are in the *other perturbations* category, while for galaxies *with* nuclear rings this fraction is only 11 per cent (1 out of 9).

Although our sample is small, the observed trends support the concept of gas inflow along the bars contributing to the formation of the nuclear rings within the inner kpc of the galaxies. Moreover, strong disturbances caused by other perturbations, such as local SF and AGN activities, within the inner kpc of galaxies, which fall under the *other perturbations* category, might inhibit the formation of nuclear rings in these galaxies.

Downloaded from academic.oup.com/mnras/article/552/3/stag1204/8721813 by guest on 30 October 2026

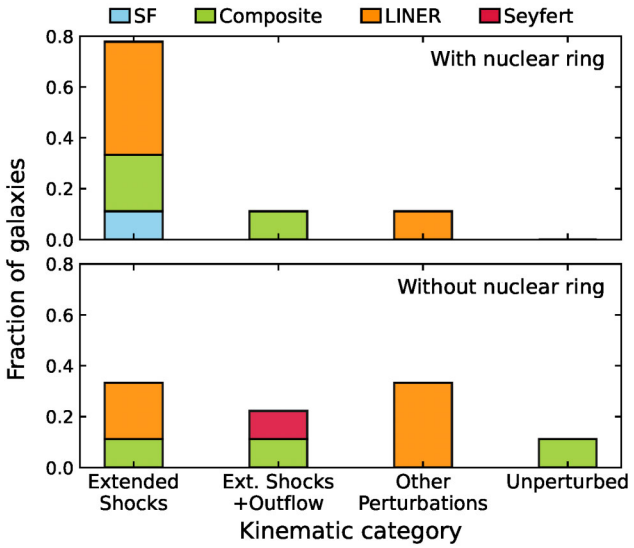

Figure 9. The fraction of galaxies in each kinematic category, grouped by the presence (top) and absence (bottom) of nuclear rings. The colours represent different nuclear emission types assigned to the galaxies based on the BPT diagram of the sample: SF in blue, composite in green, LINER in orange, and Seyfert in red.

6.3 Relating the strength of extended shocks to the central gas velocity dispersion

As shown in diagnostic maps presented for each galaxy individually in Appendix A, the velocity dispersion of all emission line groups across the sample shows a large variety. While some galaxies, such as the ones with AGN outflows, show extremely high velocity dispersions, less perturbed systems like NGC 5248, have smaller velocity dispersions across the MUSE FOV. Similar to AGN outflows, extended shocks with large amplitudes can potentially cause turbulence in the gas of galaxies, elevating velocity dispersions. Below we explore the correlation between the strength of extended shocks and the average Hα velocity dispersion within the inner kpc region of the galaxies in our sample.

6.3.1 Determination of shock strength and central gas velocity dispersion

We quantify the strength of the shock as the deprojected residual velocity magnitude seen in the residual velocity maps and introduced in Section 5.1.2. In Table 3, four values of this magnitude are given: the largest and the smallest magnitude along the blueshifted and the redshifted structures in the residual velocity maps that we associate with the shocks. Thus we have two ranges of velocity magnitude, one for each Doppler shift, and below we analyse each range separately, with the values for the blueshifted one carrying the minus sign.

In order to estimate the average Hα velocity dispersion within the inner kpc region for each galaxy, we select from the MUSE data spaxels within an elliptical region with the major axis aligned with the line of nodes, whose semimajor axis is 1 kpc and semiminor axis is cos i kpc, where i is the inclination of the galaxy given in Table 2, together with its PA. We then apply the AON threshold of 20 (M. Sarzi et al. 2006) to exclude noisy spaxels within the defined elliptical region from calculating the average velocity dispersion. This threshold is determined by examining the spread of the Hα velocity dispersion measured in the individual spaxels as a function of the AON for each galaxy individually, as presented in Appendix B, Fig. B4. Points with low AON and high velocity dispersion indicate measurements from noisy spaxels, where the velocity dispersions are artificially high due to inaccurate Gaussian fitting, likely caused by low signal.

After excluding the noisy spaxels, we compute the average Hα velocity dispersion, by taking an unweighted mean. This method of calculating the central velocity dispersion is not affected by the overall rotation, contrary to the line-width estimates for aperture-integrated spectra. The formal error on this quantity is very small ($\sim$0.1 km s^{-1}) because of the large number of spaxels that we average over. However, it is not this random error, but a systematic error that dominates the uncertainty of the central velocity dispersion value. The true value should be the mean over the spaxels weighted by the gas mass in each spaxel, which is different from the unweighted mean. An AON-weighted mean, such that spaxels with higher AON contribute more strongly while lower-quality measurements carry less weight, or a mean weighted by the Hα flux in the spaxel are alternative ways of estimating the central velocity dispersion value, and although they are poor substitutes to weighting by mass, they give an indication of the systematic error associated with the derived central velocity dispersion value.

Therefore, for each galaxy in our sample, we calculated the unweighted, AON-weighted, and flux-weighted means of the velocity dispersion over selected spaxels which are presented in Table B1. For most galaxies all three means are within less than 25 km s^{-1} from each other, except for galaxies where AGN outflows interacting with the galaxy disc create bright regions of high velocity dispersion. In those galaxies, the flux-weighted mean can be twice higher than the other two. Therefore, we calculated the final average Hα velocity dispersion as the average of the unweighted and the AON-weighted means only, discarding the flux-weighted mean. Note that for galaxies under extended shocks and outflow category, velocity dispersions evaluated in this way will systematically differ from the ones derived from aperture-integrated spectra, which are intrinsically flux-weighted. The final average Hα velocity dispersion values for all galaxies are presented in Table 3. The errors given there are half the difference between the means, and therefore they indicate uncertainty of the result against different reasonable weighting schemes.

6.3.2 The role of extended shocks in driving gas turbulence in the central regions

In the top panel of Fig. 10, for each galaxy, in which we detected extended kinematic structures, the range of deprojected residual velocity magnitudes measured along these structures, marked by the vertical bars, is plotted as a function of its central gas (Hα) velocity dispersion. The positive magnitudes give the values for the redshifted structures, and the negative magnitudes give them for the blueshifted ones. The *unperturbed* category is included for comparison, as in galaxies in this category we also identified coherent kinematic structures for which we measured the velocity magnitudes, though these magnitudes are smaller than those expected in shocks. On the other hand, galaxies in the *other perturbations* category are omitted as they lack structures associated with extended shocks.

Generally, galaxies exhibiting larger deprojected residual velocity magnitudes also tend to display higher average velocity dispersions, especially for velocity dispersions up to $\sim$80 km s^{-1}.

Downloaded from academic.oup.com/mnras/article/552/3/stag1204/8721813 by guest on 30 October 2026

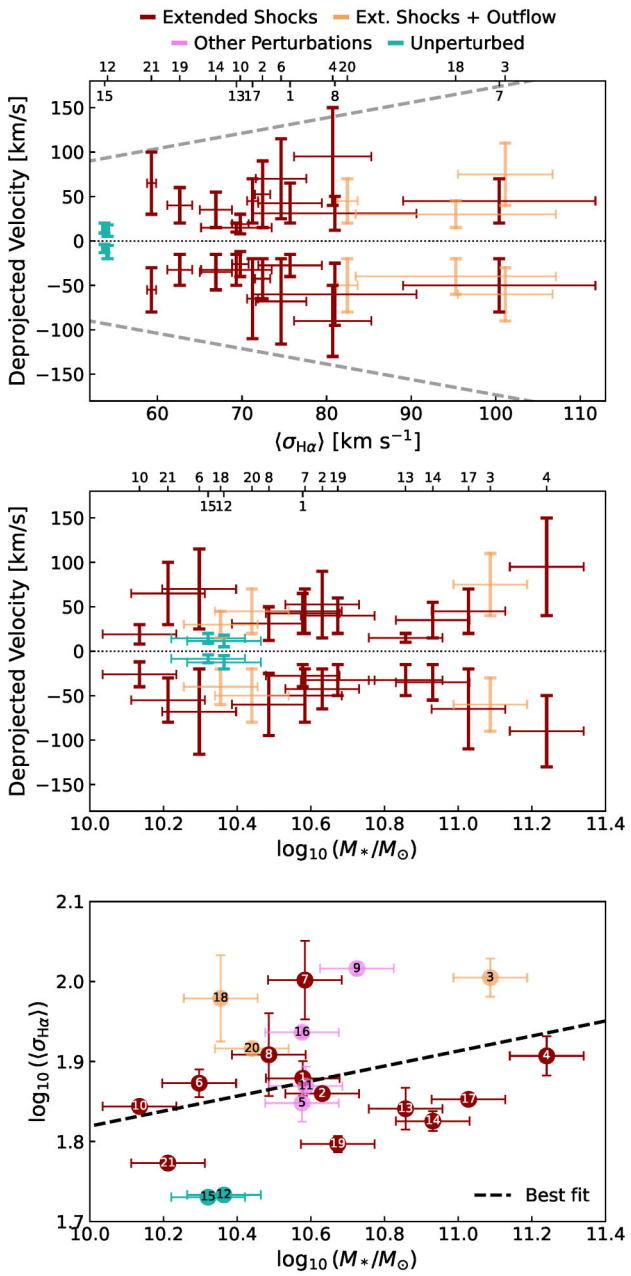

Figure 10. *Top and middle panels:* The range (minimum to maximum) of positive and negative deprojected residual velocity magnitudes measured along the extended kinematic structures (vertical bars), plotted against the average Hα velocity dispersion in the inner kpc of the galaxies (top) and stellar mass (middle). Dashed lines in the top panel mark deprojected velocity equal to $\sqrt{3}\sigma_{H\alpha}$. *Bottom panel:* Average Hα velocity dispersion plotted against stellar mass. Dashed line shows unweighted least squares fit to the data points. In all panels, the index numbers of galaxies, specified in Table 3 index column, are indicated either on the top axis or on the scatter points. The markers are colour-coded as described in the legend according to the categories assigned based on the extended shock signatures.

Although this correlation is relatively weak, it suggests that extended shocks with large deprojected velocity magnitudes may induce turbulence in the ISM, thereby increasing the overall level of kinematic disturbance and increasing the observed velocity dispersion. Along the dashed grey lines in this panel, the velocity is $\sqrt{3}$ times the observed one-dimensional velocity dispersion. Under the assumption of isotropic turbulent motions, this means that along these lines the energy in the turbulent motion is the same as the one associated with the deprojected residual velocity magnitude in the shocks. Thus this line allows us to relate the energy deposited to gas in shocks to the energy in turbulent motion. For points close to this line, the observed velocity dispersion could be attributed to disturbance caused by extended shocks.

For all galaxies in our sample, the bars indicating the ranges of velocity magnitudes in shocks lie in between the two dashed lines, which means that the energy deposited by shocks is smaller than that in the turbulent motions. Therefore the shocks cannot fully account for gas turbulent motions in the centres of galaxies, although they are likely to contribute to turbulence, as evidenced by the correlation between their strength and gas central velocity dispersion discussed above. This contribution can be significant, especially for NGC 1097 (index 4), for which the bars in Fig. 10 reach close to the grey dashed line. However, this contribution is small compared to that from the AGN, as the orange-brown bars in Fig. 10, representing the galaxies in *extended shocks and outflow* category, indicate. For all three galaxies in this category, central gas velocity dispersions are higher than in the rest of the sample, and the bars, representing velocity magnitudes in extended shocks, are well within the dashed grey lines. This means that the turbulence in gas in the central kiloparsec of those galaxies is most likely mainly driven by AGN outflows. Also, for galaxies in our *unperturbed* category (cyan bars in Fig. 10), the velocity magnitudes are very small, around 10 km s^{-1} (so that we do not classify the extended kinematic features there as shock structures), yet the observed central gas velocity dispersions there exceed 50 km s^{-1}. Clearly something else drives central gas turbulence in those galaxies.

6.4 Dependence of the observed quantities on host galaxy mass

Following the CBS selection criteria, our sample consists of galaxies with masses differing by over one order of magnitude ($10^{10.1}$–$10^{11.2}$ M$_\odot$). Below we investigate how characteristics in our sample change with galaxy mass. In the middle panel of Fig. 10, we present the deprojected velocity magnitudes of extended shocks as a function of the stellar mass of the host galaxy listed in Table 1. There appears to be a positive trend, suggesting that stronger (higher-magnitude) shocks preferentially occur in galaxies with larger stellar masses, but this trend is weak. For example, a relatively low-mass galaxy such as NGC 1433 ($10^{10.3}$ M$_\odot$) may host shocks with deprojected velocity magnitudes up to 115 km s^{-1}, almost as strong as those in a high-mass galaxy such as NGC 1097 ($10^{11.24}$ M$_\odot$), where shock velocity magnitudes reach 150 km s^{-1}.

The Faber–Jackson relation (S. M. Faber & R. E. Jackson 1976) links galaxy luminosity, and thus indirectly its mass, to its central stellar velocity dispersion. If there were a similar relation to the *gas* velocity dispersion studied above, the mass dependence could affect our results presented in Section 6.3.2. The bottom panel of Fig. 10 shows the Hα velocity dispersion in the central kpc as a function of stellar mass for all galaxies in our sample, colour-coded by kinematic category. There is a very weak trend for more massive galaxies to display higher velocity dispersion, but the plot is dominated by scatter, and therefore such weak dependence of velocity dispersion on mass does not affect our conclusions in Sec-

Downloaded from academic.oup.com/mnras/article/552/3/stag1204/8721813 by guest on 30 October 2026

tion 6.3.2. Nevertheless, the plot reveals a clear regularity in the distribution of galaxies across the different kinematic categories: *unperturbed* galaxies lie below the average mass–dispersion relation marked by the dashed line, whereas galaxies in the *extended shocks and outflows* category lie clearly above it. This distribution supports our findings from Section 6.3.2, even in the presence of the slight dependence of gas velocity dispersion on galaxy mass. Extended shocks do contribute to gas turbulence in the central regions, since galaxies without them show lower velocity dispersions than galaxies with them, but this contribution appears to be overtaken by AGN activity in galaxies with strong outflows.

Galaxies in the kinematic category *other perturbations* exhibit a wide range of velocity dispersions, reflecting the diverse non-shock processes that disturb the gas, and they all have masses below $10^{10.8}$ $M_\odot$, indicating that those perturbations are limited to lower-mass galaxies. This may be related to the fact that gas in higher-mass galaxies appears to move in a more orderly way under the stronger influence of the overall gravitational potential.

7 SUMMARY AND CONCLUSIONS

Using MUSE/VLT data, we analysed ionized gas kinematic maps of 20 galaxies from the CBS and other ancillary surveys to identify signatures of extended shocks, similar to those found along bars, that can reach the innermost regions of galaxies, and to assess whether such shocks are the dominant mechanism driving inflow towards galactic nuclei (inner ∼100 pc). This study builds on our pilot study on NGC 1097 (T. Kolcu et al. 2023), where we developed a consistent methodology to highlight signatures of extended shocks in galaxy kinematic maps using both model-dependent and independent approaches.

Extended shocks driven by the stellar gravitational potential appear as coherent velocity jumps in gas kinematic maps, with large distinctive velocities. Their appearance can be distorted by inaccurate extraction of gas kinematics from the data, as well as by local perturbations in gas, such as stellar outflows or nuclear activity. Where line profiles show large excess of flux over a single Gaussian fit, we use multiple components in emission-line fitting to account for emission from multiple sources along the line of sight such as AGN outflows. Moreover, we show that removal of the global rotational flow by subtracting the circular velocity of a fitted flat disc can produce artefacts that obscure signatures of the extended shocks in the residual velocities if the fit is inaccurate. In order to exclude those artefacts, we examine residual velocity fields for disc models with a range of parameters. As an alternative, we examine the velocity differences of Hα and [N II]λ6583 emission lines. Moreover, we analyse the origin of ionization through diagnostic line flux ratios and examine the dust morphology. Together with our kinematic study, these provide complementary evidence supporting our interpretation of extended shocks in the galaxies.

The individual analysis of the galaxies in our sample through various diagnostics revealed complex kinematic fields with unique structures in each galaxy. Finding common features among them allowed us to classify the galaxies in our sample into four kinematic categories based on the presence and characteristics of extended shock signatures identified through their diagnostic maps. These categories include: (i) *extended shocks*, where galaxies exhibit large-scale kinematic structures with high deprojected velocity magnitudes that are indicative of extended shocks.; (ii) *extended shocks and outflow*, in which outflows from the AGN dominate the innermost regions of galaxies, preventing tracing the shock structures to the nucleus; (iii) *other perturbations*, where the velocity field is clearly perturbed but it lacks extended shock signatures – kinematics are likely dominated by other perturbations, such as local star formation or AGN activities; (iv) *unperturbed*, where galaxies have relatively unperturbed kinematic maps with no evidence of shock activity.

The statistical analysis across the sample reveals the following.

(i) 12 out of 21 galaxies in our sample (∼57 per cent) exhibit extended shock signatures within their inner kiloparsec. In nine of these galaxies, the shock features can be traced down to the innermost 1–2 arcsec (corresponding to ∼100 pc, depending on distance), which is effectively MUSE resolution limit for finding extended structures, as they must stretch over the lengths of several times the spatial resolution in order to be identified. In the remaining three cases, extended shocks cannot be traced further in than ∼200–300 pc. These findings suggest that shocks may represent a dominant mechanism driving gas inflow toward the nucleus. The ∼57 per cent fraction likely represents a lower limit, as galaxies classified under *extended shocks and outflow* (∼14 per cent of the sample) may also host bar-driven shocks extending into the nucleus, but their signatures are obscured by AGN outflows.

(ii) Galaxies in the *extended shocks* classes show deprojected residual velocity magnitudes of 50 km s^{-1} or more across the shock signatures, consistent with models of bar driven shocks.

(iii) Galaxies in the *extended shocks* category have on average higher gas velocity dispersion in their inner kpc than galaxies classified as *unperturbed*, but lower than galaxies in the *extended shocks and outflow* category. Also, the deprojected residual velocity magnitudes in extended kinematic structures shows weak correlation with average gas velocity dispersion within the inner kpc. This suggests that extended shocks contribute to turbulence in the host galaxy.

(iv) We find no distinct correlation between the nuclear emission type and kinematic category. This may be attributed to the differing time-scales of gas inflow and AGN activity, as well as the small sample size.

Further examining the correlation between extended shock signatures and the central stellar structures recovered in the CBS, we find that:

(i) The two unbarred galaxies in our sample are the only galaxies with unperturbed kinematic maps, showing no evidence of shock activity. Moreover, great majority (8 out of 10) of unbarred galaxies satisfying our selection criteria does not exhibit sufficient ionized emission to be included in our analysis. Our study, limited to the stellar mass range $10^{10.1}-10^{11.2}$ $M_\odot$, shows that while centres of barred galaxies usually show strong ionized emission and signatures of extended shocks, centres of unbarred ones show either no signatures of extended shocks, or ionized emission to weak to derive gas kinematics.

(ii) The nuclear emission in galaxies with inner bars is either of LINER- or of Seyfert-type, while in galaxies without inner bars it shows no preference, with star-forming or composite emission equally likely. This indicates that inner bars suppress SF activity in the innermost regions of galaxies. We found no statistical significance between the presence or absence of inner bars and any kinematic category.

(iii) Approximately 78 per cent of galaxies hosting nuclear rings are classified under *extended shocks* vategory, compared to only 33 per cent of galaxies without nuclear rings.

Downloaded from academic.oup.com/mnras/article/552/3/stag1204/8721813 by guest on 30 October 2026

Methodology used in this work provides new means of finding coherent kinematic structures associated with extended shocks – a mechanism which could be the predominant driver of inflows to the inner ∼100–150 pc of galaxies. Although the sample size we presented is limited, this work offers a tailored strategy to characterize extended shocks over a broad range of galaxy types. Expanding this study to a larger sample size could strengthen the statistical significance of our findings by potentially uncovering stronger correlations between the presence of extended shocks and the characteristics of the galaxies such as the nuclear emission types, stellar masses, and distinct central stellar structures.

The main work for this paper was completed in close collaboration with **Dr Peter Erwin**, whose untimely passing is deeply mourned. Peter's sharp insight, kindness, and dedication to understanding galaxies shaped both this work and those who worked alongside him. He provided the data and decompositions that form the foundation of this paper, but his influence went far beyond that – through his careful feedback, patience, and genuine curiosity. His enthusiasm for astronomy and his generosity with his time and knowledge will always be remembered. This paper stands as a small reflection of his lasting impact on our work.

ACKNOWLEDGEMENTS

We thank the anonymous referee for comments that gave us opportunity to clarify the presentation of this work. We thank Luis C. Ho, Aaron Barth, and the Carnegie–Irvine Galaxy Survey group for granting us access to large-scale images of several galaxies used in this work, Ivan Baldry for his insights into improving the statistical analysis in our study, Ric Davies for guiding us through various AGN diagnostics, and Roberto P. Saglia for the nice discussions on the text. TK acknowledges the joint PhD studentship support from Liverpool John Moores University, the Faculty of Engineering and Technology and the Science and Technology Facilities Council. TK is also grateful for the financial support from The Leverhulme Trust. WM is grateful to MPE for its hospitality, which created opportunity to discuss this work with the Infrared/Submillimeter Astronomy Group there. DAG is supported by STFC grants ST/T000244/1 and ST/X001075/1. AdLC acknowledges financial support from the Spanish Ministry of Science and Innovation (MICINN) through RYC2022-035838-I and PID2021-128131NB-I00 (CoBEARD project).

DATA AVAILABILITY

MUSE data used in this work are accessed via the data archive of the European Southern Observatory at http://archive.eso.org/wdb/wdb/adp/phase3_main/form, under proposal IDs 0104.B-0404(A) and 109.22VU.001 (PI: Peter Erwin) provided by Composite Bulges Survey (CBS) collaboration; 0097.B-0640 (PI: Dimitri Gadotti) provided by the Time Inference with MUSE in Extragalactic Rings (TIMER) collaboration; 0100.B-0116(A) and 096.B-0309(A) (PI: Marcella Carollo) provided by the MUSE Atlas of Disks (MAD) collaboration.

REFERENCES

Abbate F., Possenti A., Tiburzi C., Barr E., van Straten W., Ridolfi A., Freire P., 2020, Nat. Astron., 4, 704
Ahumada R. et al., 2020, ApJS, 249, 3
Allard E. L., Peletier R. F., Knapen J. H., 2005, ApJ, 633, L25
Alloin D., Pelat D., Phillips M., Whittle M., 1985, ApJ, 288, 205
Anand G. S. et al., 2021, MNRAS, 501, 3621
Annibali F., Bressan A., Rampazzo R., Zeilinger W. W., Danese L., 2007, A&A, 463, 455
Annibali F., Bressan A., Rampazzo R., Zeilinger W. W., Vega O., Panuzzo P., 2010, A&A, 519, A40
Arp H., 1981, ApJS, 46, 75
Ashok A. et al., 2023, ApJ, 958, 100
Asmus D., Hönig S. F., Gandhi P., Smette A., Duschl W. J., 2012, J. Phys. Conf. Ser., 372, 012034
Athanassoula E., 1992, MNRAS, 259, 345
Atkinson J. W. et al., 2005, MNRAS, 359, 504
Audibert A. et al., 2019, A&A, 632, A33
Bacon R. et al., 2010, in McLean I. S., Ramsay S. K., Takami H., eds, Proc. SPIE Conf. Ser. Vol. 7735, Ground-based and Airborne Instrumentation for Astronomy III. SPIE, Bellingham, p. 773508
Bajaja E., Wielebinski R., Reuter H. P., Harnett J. I., Hummel E., 1995, A&AS, 114, 147
Baldwin J. A., Phillips M. M., Terlevich R., 1981, PASP, 93, 5
Barnes J. E., Hernquist L., 1996, ApJ, 471, 115
Beck R., Wielebinski R., 2013, in Oswalt T. D., Gilmore G., eds, Planets, Stars and Stellar Systems. Vol. 5: Galactic Structure and Stellar Populations. p. 641
Bendo G. J., Joseph R. D., 2004, AJ, 127, 3338
Bittner A. et al., 2019, A&A, 628, A117
Bittner A. et al., 2021, A&A, 646, A42
Blanton M. R. et al., 2017, AJ, 154, 28
Blasco-Herrera J., Fathi K., Östlin G., Font J., Beckman J. E., 2013, MNRAS, 435, 1958
Buta R., Combes F., 1996, Fund. Cosmic Phys., 17, 95
Buta R. J., Knapen J. H., Elmegreen B. G., Salo H., Laurikainen E., Elmegreen D. M., Puerari I., Block D. L., 2009, AJ, 137, 4487
Buta R. J. et al., 2015, ApJS, 217, 32
Calzetti D. et al., 2021, ApJ, 913, 37
Cantiello M. et al., 2018, ApJ, 856, 126
Canzian B., 1993, ApJ, 414, 487
Cappellari M., 2017, MNRAS, 466, 798
Cappellari M., Copin Y., 2003, MNRAS, 342, 345
Cappellari M., Emsellem E., 2004, PASP, 116, 138
Chemin L. et al., 2006, MNRAS, 366, 812
Cid Fernandes R., Stasińska G., Mateus A., Vale Asari N., 2011, MNRAS, 413, 1687
Ciri R., Bettoni D., Galletta G., 1995, Nature, 375, 661
Colina L., Wada K., 2000, ApJ, 529, 845
Combes F., 2003, in Collin S., Combes F., Shlosman I., eds, ASP Conf. Ser. Vol. 290, Active Galactic Nuclei: From Central Engine to Host Galaxy. Astron. Soc. Pac., San Francisco, p. 411
Cortés J. R., Kenney J. D. P., Hardy E., 2015, ApJS, 216, 9
D'Onghia E., Burkert A., Murante G., Khochfar S., 2006, MNRAS, 372, 1525
Davies R. I., Maciejewski W., Hicks E. K. S., Tacconi L. J., Genzel R., Engel H., 2009, ApJ, 702, 114
Davies R. I. et al., 2014, ApJ, 792, 101
de Jong R. S., 1996, J. Astron. Data, 2, 1
de Lorenzo-Cáceres A., Falcón-Barroso J., Vazdekis A., Martínez-Valpuesta I., 2008, ApJ, 684, L83
de Lorenzo-Cáceres A., Falcón-Barroso J., Vazdekis A., 2013, MNRAS, 431, 2397
de Lorenzo-Cáceres A. et al., 2019, MNRAS, 484, 5296
de Sá-Freitas C. et al., 2023, A&A, 678, A202
de Vaucouleurs G., de Vaucouleurs A., Corwin Herold G. J., Buta R. J., Paturel G., Fouque P., 1991, Third Reference Catalogue of Bright Galaxies. Springer-Verlag, New York
Díaz A. I., Álvarez M. Á., Terlevich E., Terlevich R., Sánchez Portal M., Aretxaga I., 2000, MNRAS, 311, 120
Donnari M. et al., 2021, MNRAS, 500, 4004
Dutton A. A., van den Bosch F. C., 2012, MNRAS, 421, 608

Downloaded from academic.oup.com/mnras/article/552/3/stag1204/8721813 by guest on 30 October 2026

Elmegreen D. M., Elmegreen B. G., Chromey F. R., Hasselbacher D. A., 1996, ApJ, 469, 131
Elmegreen D. M., Chromey F. R., Bissell B. A., Corrado K., 1999, AJ, 118, 2618
Emsellem E., Goudfrooij P., Ferruit P., 2003, MNRAS, 345, 1297
Emsellem E. et al., 2022, A&A, 659, A191
Erroz-Ferrer S. et al., 2019, MNRAS, 484, 5009
Erwin P., 2004, A&A, 415, 941
Erwin P., 2005, MNRAS, 364, 283
Erwin P., 2018, MNRAS, 474, 5372
Erwin P., 2024, MNRAS, 528, 3613
Erwin P., Sparke L. S., 2003, ApJS, 146, 299
Erwin P., Pohlen M., Beckman J. E., 2008, AJ, 135, 20
Erwin P. et al., 2015, MNRAS, 446, 4039
Erwin P. et al., 2021, MNRAS, 502, 2446
ESA/Hubble and NASA, Erwin P., 2019, Discs and Bulges, https://esahubble.org/images/potw1950a/ (Accessed Oct 2024)
Eskridge P. B. et al., 2000, AJ, 119, 536
Eskridge P. B. et al., 2002, ApJS, 143, 73
Faber S. M., Jackson R. E., 1976, ApJ, 204, 668
Fathi K., 2004, PhD thesis, Univ. Groningen
Fathi K., van de Ven G., Peletier R. F., Emsellem E., Falcón-Barroso J., Cappellari M., de Zeeuw T., 2005, MNRAS, 364, 773
Fathi K., Storchi-Bergmann T., Riffel R. A., Winge C., Axon D. J., Robinson A., Capetti A., Marconi A., 2006, ApJ, 641, L25
Fathi K. et al., 2008, ApJ, 675, L17
Fischer T. C., Crenshaw D. M., Kraemer S. B., Schmitt H. R., 2013, ApJS, 209, 1
Fragkoudi F., Athanassoula E., Bosma A., 2016, MNRAS, 462, L41
Freedman W. L. et al., 2001, ApJ, 553, 47
Fusco T. et al., 2020, A&A, 635, A208
Gadotti D. A., 2009, MNRAS, 393, 1531
Gadotti D. A. et al., 2019, MNRAS, 482, 506
García-Burillo S., Sempere M. J., Bettoni D., 1998, ApJ, 502, 235
García-Burillo S., Combes F., Schinnerer E., Boone F., Hunt L. K., 2005, A&A, 441, 1011
Greusard D., Friedli D., Wozniak H., Martinet L., Martin P., 2000, A&AS, 145, 425
Grosbøl P., Patsis P. A., Pompei E., 2004, A&A, 423, 849
Gutiérrez L., Erwin P., Aladro R., Beckman J. E., 2011, AJ, 142, 145
Haan S., Schinnerer E., Mundell C. G., García-Burillo S., Combes F., 2008, AJ, 135, 232
Haan S., Schinnerer E., Emsellem E., García-Burillo S., Combes F., Mundell C. G., Rix H.-W., 2009, ApJ, 692, 1623
Heller C. H., Shlosman I., 1994, ApJ, 424, 84
Hermosa Muñoz L., Márquez I., Cazzoli S., Masegosa J., Agís-González B., 2022, A&A, 660, A133
Ho L. C., Filippenko A. V., Sargent W. L. W., 1997, ApJS, 112, 315
Ho L. C., Li Z.-Y., Barth A. J., Seigar M. S., Peng C. Y., 2011, ApJS, 197, 21
Hopkins P. F., Hernquist L., 2006, ApJS, 166, 1
Hopkins P. F., Quataert E., 2010, MNRAS, 407, 1529
Hu Y., Lazarian A., Beck R., Xu S., 2022, ApJ, 941, 92
Hughes M. A. et al., 2005, AJ, 130, 73
Izumi T. et al., 2013, PASJ, 65, 100
Jana A., Naik S., Kumari N., 2022, JA&A, 43, 4
Jogee S., 2006, in Alloin D., ed., Physics of Active Galactic Nuclei at all Scales. Vol. 693, Springer, p. 143
Kauffmann G. et al., 2003, MNRAS, 346, 1055 (Kauffmann+03)
Kendall S., Kennicutt R. C., Clarke C., Thornley M. D., 2008, MNRAS, 387, 1007
Kewley L. J., Dopita M. A., Sutherland R. S., Heisler C. A., Trevena J., 2001, ApJ, 556, 121 (Kewley+01)
Kim W.-T., Stone J. M., 2012, ApJ, 751, 124
Knapen J. H., Beckman J. E., Shlosman I., Peletier R. F., Heller C. H., de Jong R. S., 1995a, ApJ, 443, L73
Knapen J. H., Beckman J. E., Heller C. H., Shlosman I., de Jong R. S., 1995b, ApJ, 454, 623
Knapen J. H., Shlosman I., Heller C. H., Rand R. J., Beckman J. E., Rozas M., 2000, ApJ, 528, 219
Kolcu T., Maciejewski W., Gadotti D., Fragkoudi F., Erwin P., 2023, MNRAS, 524, 207 (Paper IV)
Krajnović D., Cappellari M., de Zeeuw P. T., Copin Y., 2006, MNRAS, 366, 787
Krause M., Hummel E., Beck R., 1989, A&A, 217, 4
Kriss G. A., Hartig G. F., Armus L., Blair W. P., Caganoff S., Dressel L., 1991, ApJ, 377, L13
Lagos C. d. P. et al., 2018, MNRAS, 473, 4956
Laine S., Shlosman I., Knapen J. H., Peletier R. F., 2002, ApJ, 567, 97
Landau L. D., Lifshitz E. M., 1984, Fluid Mechanics. Course of Theoretical Physics Vol. 6, Pergamon Press, Oxford, UK
Lang P. et al., 2020, ApJ, 897, 122
Leaman R. et al., 2019, MNRAS, 488, 3904
Li Z. et al., 2023, ApJ, 958, 77
Li Z.-Y., Ho L. C., Barth A. J., Peng C. Y., 2011, ApJS, 197, 22
Lindblad P. A. B., Kristen H., 1996, A&A, 313, 733
Lindblad P. A. B., Kristen H., Joersaeter S., Hoegbom J., 1997, A&A, 317, 36
Liu D. et al., 2023, A&A, 672, A36
Maciejewski W., 2004, MNRAS, 354, 892
Man Z.-y., Peng Y.-j., Kong X., Guo K.-x., Zhang C.-p., Dou J., 2019, MNRAS, 488, 89
Marino A. et al., 2011, MNRAS, 411, 311
Martini P., Pogge R. W., 1999, AJ, 118, 2646
Martini P., Regan M. W., Mulchaey J. S., Pogge R. W., 2003, ApJ, 589, 774
Mazzalay X. et al., 2014, MNRAS, 438, 2036
Mazzuca L. M., Knapen J. H., Veilleux S., Regan M. W., 2008, ApJS, 174, 337
McKee C. F., Ostriker E. C., 2007, ARA&A, 45, 565
Mei S. et al., 2005, preprint (arXiv:astro-ph/0506314)
Menéndez-Delmestre K., Sheth K., Schinnerer E., Jarrett T. H., Scoville N. Z., 2007, ApJ, 657, 790
Mihos J. C., Hernquist L., 1996, ApJ, 464, 641
Misselt K. A., Clayton G. C., Gordon K. D., 1999, PASP, 111, 1398
Möllenhoff C., Heidt J., 2001, A&A, 368, 16
Muñoz-Mateos J. C. et al., 2013, ApJ, 771, 59
Muñoz-Mateos J. C. et al., 2015, ApJS, 219, 3
Namekata D., Habe A., Matsui H., Saitoh T. R., 2009, ApJ, 691, 1525
Navarro J. F., Frenk C. S., White S. D. M., 1995, MNRAS, 275, 56
Nemmen R. S., Storchi-Bergmann T., Eracleous M., 2014, MNRAS, 438, 2804
Nowak N., Thomas J., Erwin P., Saglia R. P., Bender R., Davies R. I., 2010, MNRAS, 403, 646
Osterbrock D. E., Ferland G. J., 2006, Astrophysics of Gaseous Nebulae and Active Galactic Nuclei. University Science Books, New York
Pan H.-A. et al., 2022, ApJ, 927, 9
Park K., Bogdanović T., 2017, ApJ, 838, 103
Piner B. G., Stone J. M., Teuben P. J., 1995, ApJ, 449, 508
Pogge R. W., Martini P., 2002, ApJ, 569, 624
Pohlen M. et al., 2010, A&A, 518, L72
Prieto M. A., Maciejewski W., Reunanen J., 2005, AJ, 130, 1472
Prieto M. A., Fernandez-Ontiveros J. A., Bruzual G., Burkert A., Schartmann M., Charlot S., 2019, MNRAS, 485, 3264
Querejeta M. et al., 2021, A&A, 656, A133
Roberts I. D. et al., 2023, A&A, 675, A78
Roberts W. W. J., Roberts M. S., Shu F. H., 1975, ApJ, 196, 381
Robertson B., Bullock J. S., Cox T. J., Di Matteo T., Hernquist L., Springel V., Yoshida N., 2006, ApJ, 645, 986
Ryder S. D., Knapen J. H., Takamiya M., 2001, MNRAS, 323, 663
Salo H. et al., 2015, ApJS, 219, 4
Sanders R. H., Huntley J. M., 1976, ApJ, 209, 53
Sarzi M. et al., 2006, MNRAS, 366, 1151
Schawinski K., Koss M., Berney S., Sartori L. F., 2015, MNRAS, 451, 2517
Schinnerer E., Maciejewski W., Scoville N., Moustakas L. A., 2002, ApJ, 575, 826

Downloaded from academic.oup.com/mnras/article/552/3/stag1204/8721813 by guest on 30 October 2026

Schnorr-Müller A., Storchi-Bergmann T., Robinson A., Lena D., Nagar N. M., 2016, MNRAS, 457, 972
Schnorr-Müller A., Storchi-Bergmann T., Nagar N. M., Robinson A., Lena D., 2017, MNRAS, 471, 3888
Schoenmakers R. H. M., Franx M., de Zeeuw P. T., 1997, MNRAS, 292, 349
Sheth K., Vogel S. N., Regan M. W., Thornley M. D., Teuben P. J., 2005, ApJ, 632, 217
Sheth K. et al., 2010, PASP, 122, 1397
Shlosman I., 2001, in Knapen J. H., Beckman J. E., Shlosman I., Mahoney T. J., eds, ASP Conf. Ser. Vol. 249, The Central Kiloparsec of Starbursts and AGN: The La Palma Connection. Astron. Soc. Pac., San Francisco, p. 55
Shlosman I., Noguchi M., 1993, ApJ, 414, 474
Shlosman I., Frank J., Begelman M. C., 1989, Nature, 338, 45
Sil'chenko O. K., Moiseev A. V., Shulga A. P., 2010, AJ, 140, 1462
Silva-Lima L. A., Martins L. P., Coelho P. R. T., Gadotti D. A., 2022, A&A, 661, A105
Silva-Lima L. A. et al., 2025, MNRAS, 540, 2787
Simien F., Prugniel P., 2002, A&A, 384, 371
Smajić S., Moser L., Eckart A., Busch G., Combes F., García-Burillo S., Valencia-S. M., Horrobin M., 2015, A&A, 583, A104
Smirnova K. I., Wiebe D. S., 2019, Astron. Rep., 63, 445
Sormani M. C., Binney J., Magorrian J., 2015, MNRAS, 449, 2421
Sosa-Brito R. M., Tacconi-Garman L. E., Lehnert M. D., Gallimore J. F., 2001, ApJS, 136, 61
Storchi-Bergmann T. et al., 2003, ApJ, 598, 956
Storchi-Bergmann T., Dors Oli L. J., Riffel R. A., Fathi K., Axon D. J., Robinson A., Marconi A., Östlin G., 2007, ApJ, 670, 959
Strauss M. A. et al., 2002, AJ, 124, 1810
Stuber S. K. et al., 2021, A&A, 653, A172
Stuber S. K. et al., 2023, A&A, 676, A113
Terashima Y., Ho L. C., Ptak A. F., Mushotzky R. F., Serlemitsos P. J., Yaqoob T., Kunieda H., 2000, ApJ, 533, 729
Tonry J. L., Dressler A., Blakeslee J. P., Ajhar E. A., Fletcher A. B., Luppino G. A., Metzger M. R., Moore C. B., 2001, ApJ, 546, 681
Tully R. B., 1988, Nearby Galaxies Catalog. Cambridge Univ. Press, New York
van der Kruit P. C., Allen R. J., 1978, ARA&A, 16, 103
van der Marel R. P., Franx M., 1993, ApJ, 407, 525
Vazdekis A. et al., 2015, MNRAS, 449, 1177
Veron-Cetty M. P., Veron P., 1986, A&AS, 66, 335
Véron-Cetty M. P., Véron P., 2006, A&A, 455, 773
Vollmer B., Soida M., Beck R., Chung A., Urbanik M., Chyży K. T., Otmianowska-Mazur K., Kenney J. D. P., 2013, A&A, 553, A116
Walsh W., Staveley-Smith L., Oosterloo T., 1997, AJ, 113, 1591
Woo J.-H., Urry C. M., 2002, ApJ, 579, 530
Zurita A., Relaño M., Beckman J. E., Knapen J. H., 2004, A&A, 413, 73

APPENDIX A: INDIVIDUAL ANALYSIS OF SAMPLE GALAXIES

In the following sections, we provide details on the analysis and specific results for each galaxy in our sample. The main results for each galaxy are visualised in multipanel Figs A1–A20, one for each galaxy, each following the same arrangement. Here, we describe the contents of the panels, and we introduce their respective names (in italics) that we use in the remainder of this section. The top left panel shows a *large-scale image* of the galaxy, with the MUSE FOV marked with a red box. These images are taken from either the Carnege–Irvine Galaxy Survey (L. C. Ho et al. 2011; 'CGS' in the lower-left corner of the image)[7] or from DR16 of SDSS (R. Ahumada et al. 2020; 'SDSS' in the lower-left corner).[8] Immediately below this (leftmost panel in the second row) is a *colour image* created by dividing the 4650–9300 Å wavelength range of MUSE data cubes into three segments: ∼ 4650–6200, 6200–7750, and 7750–9300 Å. These segments were assigned to blue, green, and red channels and combined to produce the colour image. The cyan box overplotted on the colour image marks the inner 40 arcsec × 40 arcsec region which was further analysed. All other panels in the figure show this same 40 arcsec× 40 arcsec FOV. Further below, in the leftmost panel of the third row, we show an *unsharp mask image* generated from the MUSE data following the procedure described in Section 4.1.4.

The remaining three panels of the first row show the fluxes of Hα, [N II]λ6583, and [O III]λ5007 emission lines (from left to right) in units 10^{-20} erg s^{-1} cm^{-2}. For brevity, these are referred to as *H α*, *[N II] λ 6583,* and *O III] λ 5007 flux maps*. White spaxels in the flux maps indicate flux below the detection limits. The three panels below them (the second row) show the LOS velocities for the three emission line groups defined in Section 3.2: the Balmer lines, the low-ionization lines, and the high-ionization lines. Because of the lines dominating in each group, these are referred to as *H α*, *[N II] λ 6583* and *O III] λ 5007 velocity maps*. In the corresponding panels of the third row, we plot the *dispersion maps* showing the velocity dispersion for the same line groups. Note that spaxels of low flux have inaccurate velocity and dispersion estimates, which results in areas of spaxels with close-to-random distribution of the kinematic values which should be disregarded.

Finally, in the fourth row, the leftmost two panels connected together show information from emission-line ratios: the *BPT map* to the left, where individual spaxels are colour-coded by their location in the *BPT diagram* immediate to the right (see Section 4.1.3 for the details on the construction of the BPT maps). The right two panels in the fourth row show two different maps created by *subtracting* emission-line velocities. The first one, the *residual velocity map*, shows the observed Ha velocity minus the best-fitting circular-rotation model (see Section 4.1.1). The second, the *velocity difference map* is created by subtracting the Hα velocity map from the [N II]λ6583 velocity map (see Section 4.1.2).

The grey contours in the flux, velocity, and dispersion maps, as well as in all the maps in the bottom row of panels, are isophotes of the Hα emission. The cross mark is the centre of the galaxy.

A1 IC2051

The images and the diagnostic maps of IC 2051 are presented in Fig. A1. As shown in the large-scale and colour images, within the MUSE FOV, the galaxy has a luminous core, a bar situated within the ∼11 arcsec radius, a star-forming inner ring at approximately 12 arcsec radius which encompasses the bar, and an outer ring encircling the inner one. The *Hubble Space Telescope* (*HST*) observations (ESA/Hubble and NASA and P. Erwin 2019) of the galaxy reveal a small dusty nuclear ring within the ∼2 arcsec radius. The MUSE FOV covers the entire bar of the galaxy and a portion of the inner ring surrounding it. Starting from the inner edge of the inner ring, ∼11 arcsec north from the centre, a dust lane stretches towards the south along the bar. After reaching ∼3 arcsec west of the centre, the dust lane curves towards the

[7] https://cgs.obs.carnegiescience.edu/CGS/database_tables/sample1.html

[8] https://skyserver.sdss.org/dr16/en/home.aspx

Downloaded from academic.oup.com/mnras/article/552/3/stag1204/8721813 by guest on 30 October 2026

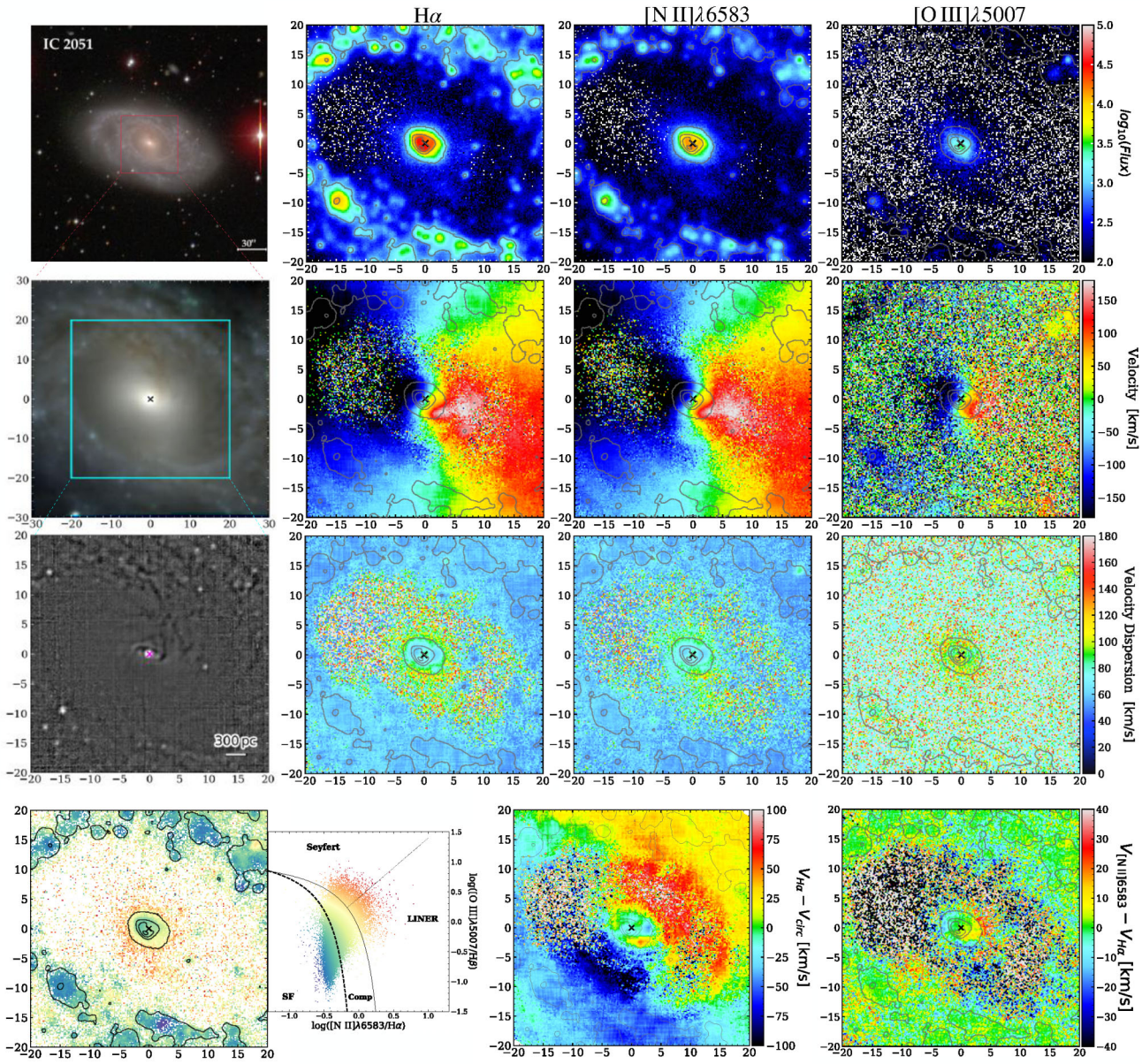

Figure A1. Images and diagnostic maps of IC 2051. Panels show the same as in Fig. 2.

centre connecting to the nuclear ring; a counterpart of this dust lane is seen to the north of the centre. These distinctive dust lane features are more prominent in the unsharp mask image of the galaxy, and resemble two curving dust lanes often seen in bars.

As shown in the flux maps, the strongest emission in all three line groups is concentrated within the radius of ∼3 arcsec. Particularly, the Hα emission forms a crescent of radius ∼1–2 arcsec south-east of the centre. Outside the ∼3 arcsec radius, around the bar, the emission is strongly depleted. The inner ring has relatively high Hα and [N II]λ6583 emission, featuring clumps of enhancements dispersed throughout due to local star formation; the [O III]λ5007 emission within the inner ring is relatively weak.

The velocity maps of all emission line groups show signs of non-circular motions throughout the entire MUSE FOV. The zero velocity line forms an 'S' shape, characteristic of the flow in bars. The velocity dispersion maps of Hα and [N II]λ6583 exhibit peak values at the centre, reaching roughly 100 km s^{-1}. Past ∼1 arcsec from the centre, the velocity dispersion drops and reaches the lowest values, approximately 50 km s^{-1}, in two lobes at ∼2 arcsec east and west of the centre. These two lobes extend beyond the crescent seen in Hα and [N II]λ6583 emission. Outside the two lobes, the velocity dispersion increases yet we can not reliably determine the velocity dispersion values beyond this region due to poor signal. The random motions of the gas within the inner ring are mild, with velocity dispersion values for Hα and [N II]λ6583 staying around 50–60 km s^{-1}.

Within the ∼3 arcsec radius, the BPT map of the galaxy exhibits composite emission with contribution from SF, SF being the strongest within the ∼2 arcsec radius, particularly within the crescent in Hα emission. This BPT pattern together with

Downloaded from academic.oup.com/mnras/article/552/3/stag1204/8721813 by guest on 30 October 2026

the dust and low velocity dispersion is consistent with the small nuclear ring of the galaxy. The inner ring encompassing the bar has prominent star formation activity throughout.

The poor signal within the bar region makes IC 2051 a challenging target when fitting a circularly rotating disc to its velocity field. Results from KINEMETRY, when run with free parameters and a fixed centre, show a roughly stable radial distribution of i converging on $\sim$41°, but the distribution of position angle (PA) of the line of nodes (LON) is fluctuating. In an attempt to obtain more consistent parameter distributions, we binned the velocity map by aggregating the data into 2×2, 3×3, and 4×4 spaxel blocks. While this technique decreases the resolution of the velocity map, it increases the signal within each bin. However, even after applying binning, the results did not change. Therefore, we ran KINEMETRY with different i and PA of the LON values, trying to minimize the artefacts arising from their incorrect values in the residual velocity maps. A model fitted with a fixed centre, fixed i at 41°and the PA of the LON at 60°effectively showed the minimum artefacts within the $\sim$3 arcsec radius. Therefore, we fixed the parameters to these values for further analysis. However, these values differed from the values obtained in CBS from large-scale fits to outer isophotes (see Table 2). The resultant residual velocity map is presented in Fig. A1. Since we aim to trace the inflow to the innermost regions, we focused on minimizing the artefacts within the $\sim$3 arcsec radius. Beyond this region, the artefacts of incorrectly fitted PA of the LON dominate the residual velocity map, observed as m=1 harmonic terms.

The best fit of the rotating disc exposes two structures within the $\sim$4–5 arcsec radius, exhibiting amplitudes of $\sim$30–40 km s^{-1} in the residual velocity map, one with positive and one with negative velocity residuals. The corresponding minimum and maximum deprojected residual velocity amplitudes measured along these structures are $-$15 and $-$40 km s^{-1} for negative and 20 and 65 km s^{-1} for positive velocities. The feature exhibiting negative velocity residuals overlaps with the dust lane on the west, coinciding with its curve and extension towards the centre. In the velocity difference map, there is a coherent structure with positive values, with amplitude of $\sim$10–15 km s^{-1}, extending from $\sim$4 arcsec south-west of the centre towards $\sim$4 arcsec east. One could argue that there is a counterpart of this feature in the north-east, exhibiting negative velocities around similar velocity amplitudes. The largest amplitudes of these two structures are co-spatial with the largest amplitudes of the features seen in the residual velocity map.

The coherent kinematic features in IC 2051 extend over several hundred parsecs, which are outlined in Fig. 3, and exhibit large deprojected residual velocity magnitudes of up to $\sim$65 km s^{-1}. We therefore attribute these features to coherent extended shocks in the gas. A summary of the properties of the extended structures, including their radial extents and velocity magnitudes, is provided in Table 3. While a part of the gas shock structure seen in the residual velocity map coincides with the dust lanes, the structures seen in the velocity difference map are $\sim$1 arcsec downstream from the dust lanes.

A2 NGC 289

The images and diagnostic maps of NGC 289 are presented in Fig. A2. As shown in large scale and colour images, NGC 289 has a luminous core, a bar located within the $\sim$15 arcsec radius and two star-forming spiral arms surrounding the bar. Both spiral arms extend from the bar region several tens of kpcs towards the outer parts of the galaxy, where they both appear disturbed; this disturbance is associated with the interacting companion of the galaxy (H. Arp 1981; G. J. Bendo and R. D. Joseph 2004). The MUSE FOV covers the entire bar region, together with a portion of the spiral arms. The dust lanes along the spiral arms and the bar are notably seen in the unsharp mask image of the galaxy.

The Hα and [N II]λ6583 flux maps show two central emission peaks. One at the nucleus and the other $\sim$2 arcsec east of the centre. These regions coincide with the region of a small nuclear disc with $\sim$ 1 arcsec radius that was found in C. Sá-Freitas et al. (2023). Within the bar region, there is clumpy Hα emission likely originating from local SF, as well as extended emission elongated with the bar, close to the bar's major axis and on its leading side, likely related to shocks in the bar, which upon close inspection can be attributed to a set of aligned emission clumps. These structures are also seen, though relatively weaker, in [N II]λ6583 emission. The spiral arms show prominent Hα and [N II]λ6583 emission throughout their extent. Compared to Hα and [N II]λ6583, [O III]λ5007 emission is notably weaker and is mostly confined within the $\sim$4 arcsec radius of the galaxy, its elongation at the larger radii not correlated with the orientation of the bar.

The Hα and [N II]λ6583 velocity maps show signs of non-circular motions, particularly along the zero velocity line where several distinct features are seen. Approximately 1.5–2 arcsec towards the north-west and 2–3 arcsec south-east from the centre, Hα and [N II]λ6583 velocities reach a local maximum of around 120 km s^{-1}. These two regions are not co-spatial with the central peaks in the emission. However, throughout the region where emission is notably high, within the $\sim$3–4 radius, the Hα and [N II]λ6583 velocities also show an increase, with values $\sim$90–100 km s^{-1}. Approximately 6 arcsec north-east from the centre, a velocity peak with Hα and [N II]λ6583 velocities, $\sim$80–100 km s^{-1} is seen; this coincides with a clumpy structure in Hα emission, which may indicate a young stellar cluster moving with respect to the ambient medium.

The centre of the galaxy exhibits Hα and [N II]λ6583 velocity dispersion values around 100–120 km s^{-1}, spanning over a region from the centre $\sim$4 arcsec towards the north and south-east, almost manifesting an 'S' shape. From the centre $\sim$2 arcsec towards the east, velocity dispersion reaches a minimum, exhibiting values around 50 km s^{-1}. This region coincides with a region with high Hα velocity. Moreover, $\sim$6 arcsec towards the north-east from the centre, another velocity dispersion minimum is seen which coincides with the Hα clump of velocity higher than its surroundings. Several other features with low Hα and [N II]λ6583 velocity dispersion are seen along the bar, coinciding with the two regions with elevated Hα flux. Throughout the extent of the spiral arms, the velocity dispersion of both Hα and [N II]λ6583 remains around 50–60 km s^{-1}.

The disc orientation parameters, PA of the LON = 125°and i = 46°obtained from KINEMETRY agree with the values from large-scale studies (W. Walsh et al. 1997: PA of the LON = 130°and i = 46°). Thus, we fit the rotating disc by fixing the parameters to these values. The residual velocity map of the galaxy reveals several distinct coherent structures. Outside the bar region, velocity residuals take a spiral pattern exhibiting amplitudes of $\sim$20–30 km s^{-1}. Within the bar region, the velocity residuals form a straight feature with amplitudes of $\sim$50 km s^{-1}, one with positive and one with negative velocities. The deprojected residual velocity amplitudes across these structures are large, up to 70–90 km s^{-1}. The innermost part of the structure with positive velocities,

Downloaded from academic.oup.com/mnras/article/552/3/stag1204/8721813 by guest on 30 October 2026

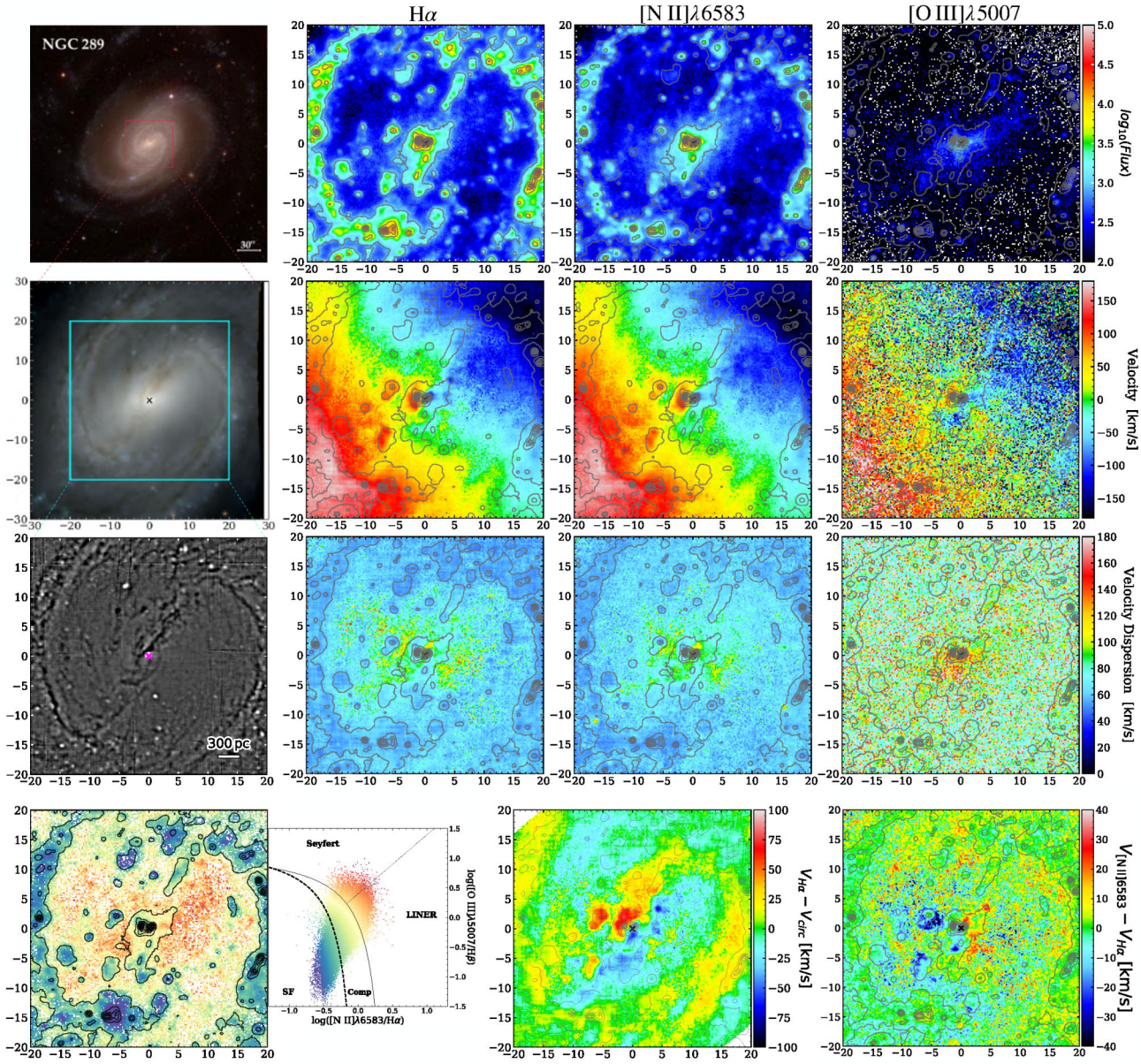

Figure A2. Images and diagnostics maps of NGC 289. Panels show the same as in Fig. 2.

at ∼2 arcsec north-east from the centre, coincides with a region of high Hα and [N II]λ6583 velocities. The spiral and straight structure with positive velocity residuals meet at the north-west end of the bar. The straight structure with negative velocities extending along the bar passes the centre by ∼7 arcsec towards the north-west end of the bar. Approximately 5 arcsec north-east from the centre, high positive velocity residuals with amplitudes of ∼50 km s^{-1} are seen in the Hα clump.

The velocity difference map is generally noisy. Along the bar, two structures with velocity difference amplitudes around ∼15–20 km s^{-1} are visible, one stretching from the centre ∼5 arcsec towards the south, and the other stretching from the centre ∼3 arcsec towards the north-west. Approximately 4–5 arcsec north-east of the centre, surrounding the clumpy region exhibiting high Hα flux, the velocity differences reach ∼30 km s^{-1} likely indicating a spatial overlap of two regions with different physical conditions.

The BPT map of the galaxy reveals composite emission in the centre. Approximately 2 arcsec east of the centre, coinciding with the off-centre Hα clump, contribution from SF is stronger than the central clump. Along the bar, the emission is of a composite nature with contribution from SF. Within the bar region, several distinct star-forming clumps are present, including the region at ∼6 arcsec north-east from the centre, where we observed high Hα flux. Outside the star-forming clumps, the ionization is dominated by the LINER region. Furthermore, the spiral arms predominantly show active SF throughout their entire extent.

Although rather discontinuous, coherent spiral and straight structures seen in the residual velocity map extend across several hundreds of parsecs, exhibiting large deprojected velocity

Downloaded from academic.oup.com/mnras/article/552/3/stag1204/8721813 by guest on 30 October 2026

magnitudes of ∼60–90 km s^{-1} (see outlined features in Fig. 3, also a summary of the properties of the extended structures, including their radial extents and velocity magnitudes, is provided in Table 3). Moreover, the alignment of these kinematic features with the dust lanes are compelling evidence of the presence of extended shocks in gas. Additionally, we hypothesize that a portion of the straight feature with negative velocities, which passes the centre by ∼7 arcsec towards the north-west end of the bar, is the overshot gas after being funnelled in towards the centre from the south-east end of the bar. Instead of falling further inwards, the gas continues to flow towards the north-west bar end, where it collides with the gas present there.

A3 NGC 613

The images and diagnostic maps of NGC 613 are presented in Fig. A3. As shown in the large scale and colour image, NGC 613 has a luminous core, a star-forming nuclear ring of ∼6 arcsec radius, a bar and star-forming spiral arms surrounding the bar region. The MUSE FOV encompasses the core, the nuclear ring and nearly the entire bar. Along the bar, two prominent dust lanes are seen. These dust lanes are prominent in the unsharp mask image of the galaxy, where they curve to follow the nuclear ring over a full circle.

As shown in the flux maps of the galaxy, the Hα and [N II]λ6583 emission is mostly confined within the ∼5–6 arcsec radius. The Hα emission has several peaks in the nuclear ring and one ∼0.5 arcsec south-east of the nucleus. The main peak of the [N II]λ6583 emission is ∼0.5 arcsec south-east of the nucleus, the peaks in the nuclear ring correspond to the ones in Hα emission, but they are rather weaker than the nuclear peak. [O III]λ5007 emission, rather strong and extended, is confined within a region stretching from the central ∼8–9 arcsec towards the north-east, indicating possibly an off-plane outflow. Some Hα and more [N II]λ6583 emission appear to extend from the nuclear ring towards that direction as well. Moreover, there is enhanced emission across all line groups in an elongated region at ∼3–6 arcsec south-west of the centre. While Hα and [N II]λ6583 emission in this region appears joined with the emission from the nuclear ring, [O III]λ5007 emission appears notably separated. The separation overlaps with the region where the dust lane to the south-east connects to the nuclear ring. Clumpy Hα emission is seen along the bar lanes, but also towards the north-east of the centre, where it appears to group into a spiral arm offset tangentially by roughly 90°from the dust lanes.

The velocity fields of all emission line groups are strongly perturbed, showing signs of non-circular motions. Outside the nuclear ring, there is a region with large negative velocities across all line groups, covering a PA between 0 and 45°and extending radially out to ∼10 arcsec in Hα and [N II]λ6583 and ∼15 arcsec in [O III]λ5007, with amplitudes around ∼80–100 km s^{-1} for Hα and [N II]λ6583, and ∼150 km s^{-1} for [O III]λ5007. This region appears separate from the main region with blueshifted velocities along the LON and is likely associated with the elevated [O III]λ5007 emission and with the outflow.

Within a region extending from the centre towards ∼5–6 arcsec north-east, the velocity dispersion across all emission line groups reaches a peak, with values exceeding 150 km s^{-1} for Hα and [N II]λ6583, and 200 km s^{-1} for [O III]λ5007. This region coincides with the regions of negative velocities across all line groups. The velocity dispersion values of Hα and [N II]λ6583 in the nuclear ring are around ∼70 km s^{-1}. Outside the nuclear ring, the velocity dispersion across all line groups is high, around ∼100–140 km s^{-1} but in the spiral towards the north-east with clumpy Hα emission, Hα and [N II]λ6583 velocity dispersion values reach a minimum of ∼50–70 km s^{-1}.

The disc orientation parameters, the PA of the LON = 115° and i = 37°, obtained from KINEMETRY agree well with the parameters estimated from large-scale fits; the PA of the LON differing by 5°from the value estimated from E. Bajaja et al. (1995) (see Table 2). The residual velocity map of the galaxy reveals several strong localized extremes within the nuclear ring, likely originating from the complex interaction between the inflow, SF and the AGN outflows. Throughout the region to the north-east of the nucleus, associated with AGN outflows, strong negative residual velocities with amplitudes exceeding 50 km s^{-1} are seen. Coinciding with the dust lanes along the bar, two coherent structures with amplitudes ∼30–50 km s^{-1} are seen, one exhibiting negative and one exhibiting positive velocity residuals. The corresponding deprojected residual velocity amplitudes across these coherent structures along the bar range from 30–40 to 90–110 km s^{-1}. While the structure with positive velocities can be traced towards its connection to the nuclear ring, the structure with negative velocities is dominated by the strong AGN outflows likely located in front of it. To the east of the nuclear ring, there is a coherent region where the amplitudes of the residual velocity exceed 50 km s^{-1}. This region is not co-spatial with the SF spiral structure with clumpy Hα emission seen in the BPT map; only their innermost parts overlap.

The velocity difference map of the galaxy exposes two coherent structures with amplitudes of ∼40–50 km s^{-1}. One of these structures, characterized by negative velocity differences, extends from the central ∼10–11 arcsec towards the north. The other structure, characterized by positive velocity differences, is situated ∼3 arcsec east of the centre and extends ∼6 arcsec towards the north-east. These two structures nearly encircle the area exhibiting coherent negative velocity residuals, which are associated with the AGN outflows. This suggests the presence of two distinct regions of gas with differing physical conditions along these structures, where there is a transition from emission dominated by the disc to that dominated by outflow. Moreover, there is a faint coherent continuous structure with amplitudes of ∼10–15 km s^{-1} upstream from the coherent structure with positive residual velocities along the dust lane to the south-east.

The core of NGC 613 is classified as a LINER type (A. Audibert et al. 2019). In the BPT map, LINER emission is seen at the very core as well as in the north-east region, where velocity dispersion across all line groups peaks, and in the south-east region with enhanced emission across all line groups. The latter two regions resemble a bi-symmetric structure, co-spatial with pronounced [O III]λ5007 emission. This confirms that these features are likely originating from AGN outflows; consistent with similar emission-line diagnostics. The interpretation of outflows in this galaxy is provided by L. A. Silva-Lima et al. (2025). However, the emission from a high-energy mechanism occurs where the innermost part of the dust lane connects to the nuclear ring, which may indicate the inflowing gas is irradiated by the AGN, except for the north-east region, where the nuclear ring is dominated by SF. Furthermore, the clumpy Hα emission in the north-east appears as a coherent spiral in SF, winding from the north-east of the centre and connecting to the nuclear ring at the east. This spiral was not identified clearly in the emission or characterized by the dust lanes, but it is notably revealed in the BPT map.

Downloaded from academic.oup.com/mnras/article/552/3/stag1204/8721813 by guest on 30 October 2026

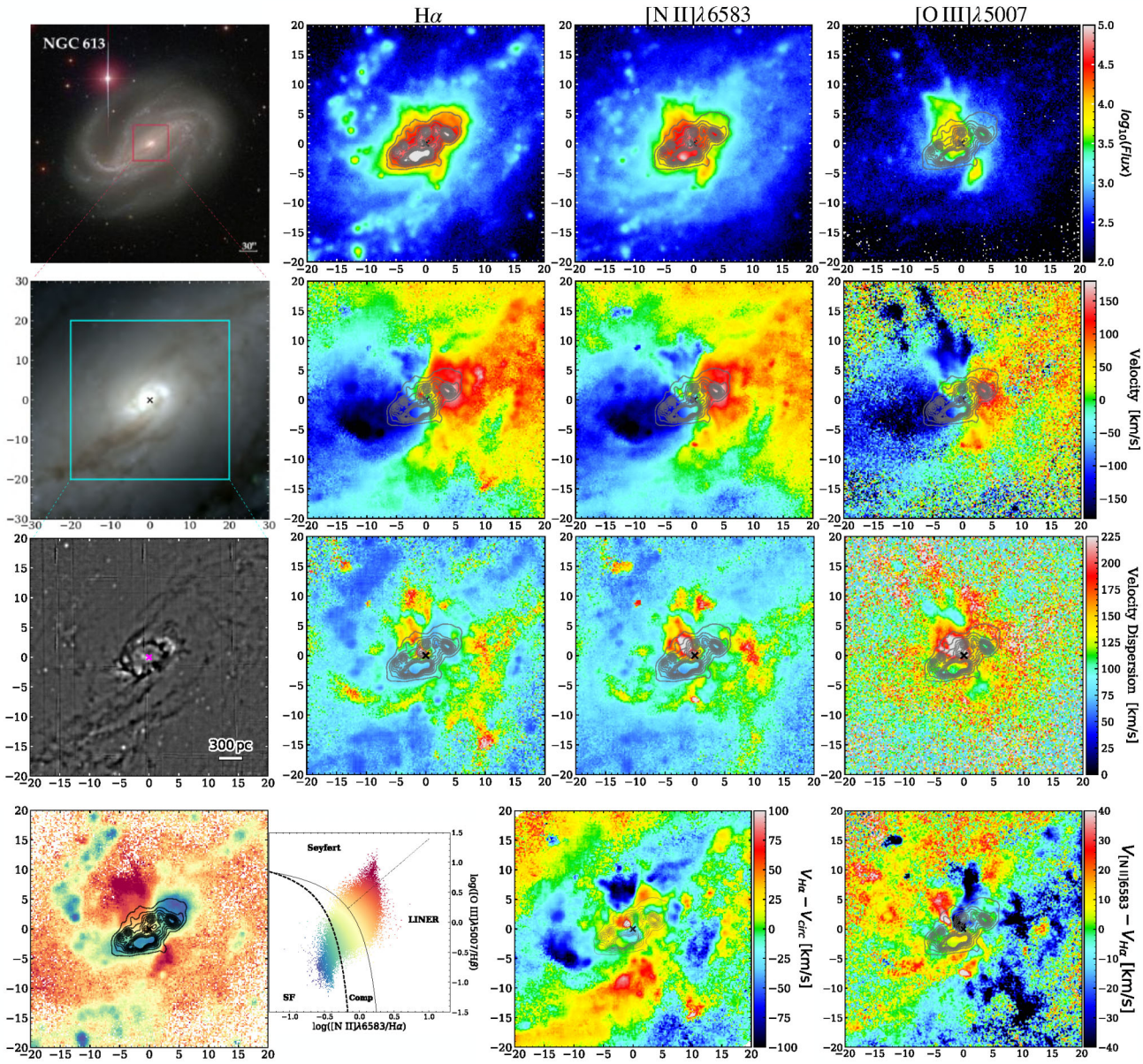

Figure A3. Images and diagnostics maps of NGC 613. Panels show the same as in Fig. 2.

Various aspects of our methodology provide evidence for extended shocks along the dust lanes in the bar, connecting to the nuclear ring. As presented in Table 3, these structures span galactocentric radii from several hundred parsecs to a few kiloparsecs, with deprojected residual velocity magnitudes of approximately 90–110 km s^{-1}. However, the presence of strong AGN outflows within the nuclear ring prevents identifying the signatures of extended shocks to the innermost regions. Therefore, based on the grouping described in Section 5.3, this galaxy is classified under *extended shocks and outflows* kinematic category.

A4 NGC 1300

The images and the diagnostic maps of NGC 1300 are presented in Fig. A4. As can be seen in large scale and colour images, the galaxy has a luminous core encircled by a nuclear ring or disc and a prominent classical bar (P. A. B. Lindblad and H. Kristen 1996; P. A. B. Lindblad et al. 1997). It also has two star-forming spiral arms surrounding the bar region. The MUSE FOV encompasses the core, the nuclear ring, and approximately two-thirds of the bar. Along the bar, we see two dust lanes, one stretching from the east towards the centre, connecting to the nuclear ring from the north, and the other as the weak counterpart of the former, stretching from the west towards the centre, connecting to the nuclear ring from the south. Several other faint dust lanes downstream from the main dust lane to the east are seen, yet these do not join to the nuclear ring, and instead they continue towards the north-west and join the dust lane to the west. Within the nuclear ring, we notice two dust spirals curving towards the core of the galaxy. They appear to connect with the dust lanes in the bar;

Downloaded from academic.oup.com/mnras/article/552/3/stag1204/8721813 by guest on 30 October 2026

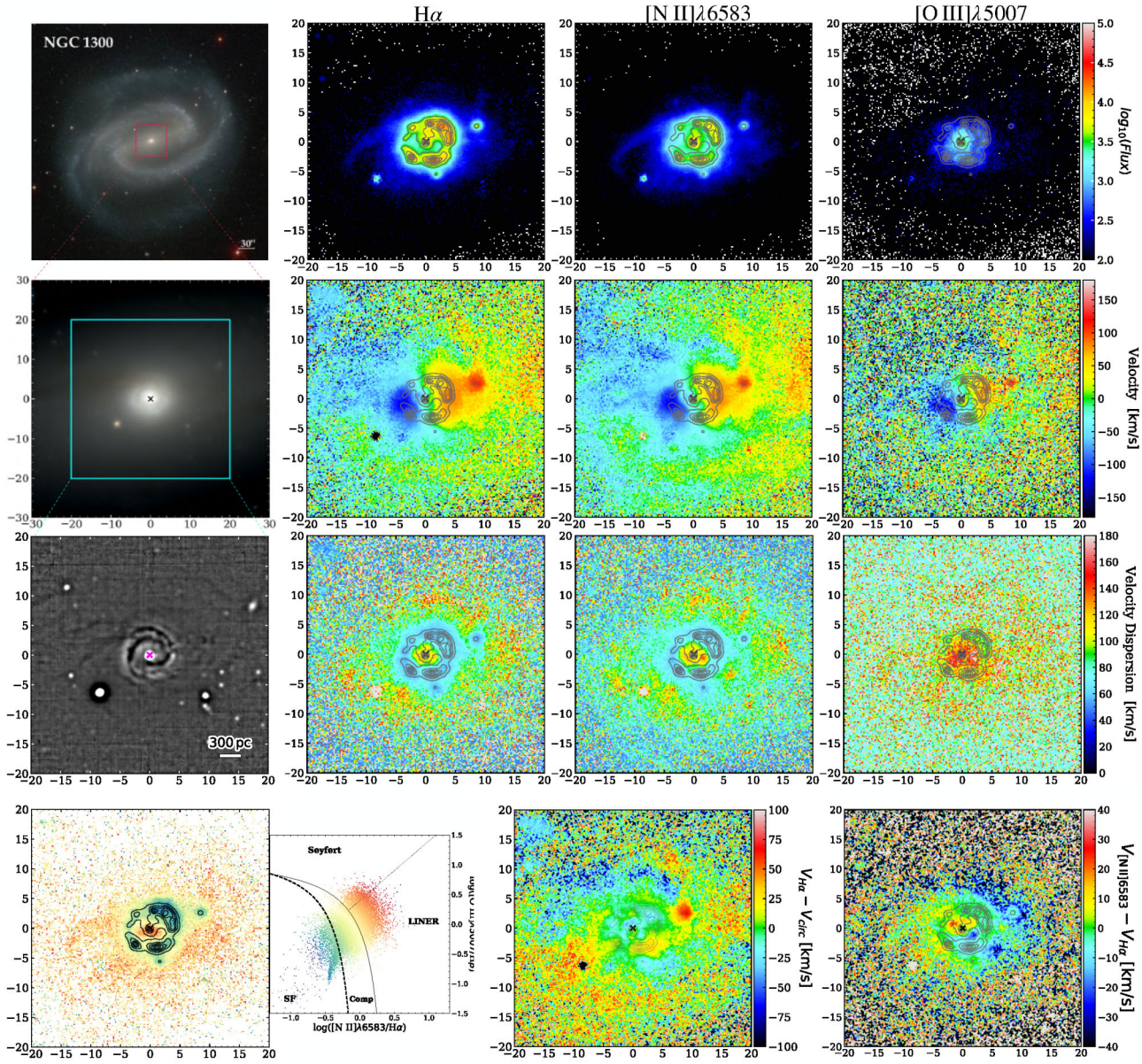

Figure A4. Images and diagnostics maps of NGC 1300. Panels show the same as in Fig. 2.

at the inner end of the western lane, south of the nucleus, the spiral lane looks doubled. The unsharp mask image of the galaxy delineates these faint dust structures.

As shown in the flux maps, Hα and [N II]λ6583 emission is high in the nucleus, drops at $\sim$2–3 arcsec from the centre, and then is high in the nuclear ring of $\sim$5 arcsec radius. In comparison with Hα and [N II]λ6583, the [O III]λ5007 emission is relatively weak and is confined within the $\sim$3 arcsec radius. Outside the nuclear ring, within the bar region, the emission across all line groups is weak, yet several round regions with enhanced Hα and [N II]λ6583 emission are seen, likely originating from local SF.

The velocity maps of Hα and [N II]λ6583 present signs of non-circular motions. Outside the nuclear ring, the zero velocity line has a strong indent and inside the nuclear ring, it shows a strong wiggle due to several local velocity peaks. The velocity dispersion of all line groups shows a peak within the inner $\sim$3 arcsec region, with values $\sim$110–140 km s^{-1}. The values decrease and remain around $\sim$50–60 km s^{-1} within the nuclear ring. Outside the nuclear ring, within the round region where enhanced Hα and [N II]λ6583 emission is seen, at $\sim$9 arcsec north-west of the centre, there is low Hα and [N II]λ6583 velocity dispersion around $\sim$60 km s^{-1}. Moreover, there is a relative increase in velocity dispersion outside the nuclear ring but we can not determine the values reliably due to poor signal within the bar region.

Because of the poor signal within the bar region, the disc orientation parameters of the galaxy are not well constrained with KINEMETRY; the estimated distributions of i and PA of the LON fluctuate as a function of the radius of the fitted ellipse. Therefore, we ran KINEMETRY with different i and PA of the LON values, to fit various rotating discs to the Hα velocity field and, we studied

Downloaded from academic.oup.com/mnras/article/552/3/stag1204/8721813 by guest on 30 October 2026

the corresponding residual velocity maps to identify parameter values that minimize the artefacts. A rotating disc fitted with a fixed centre, PA of the LON at 107°and i at 35°minimized the artefacts seen in residual velocity maps. Consequently, these values are selected as the final orientation parameters for the disc. When compared to the disc orientation parameters estimated from the large-scale fits in P. A. B. Lindblad et al. (1997) (i = 35°and PA of the LON = 87°), the settled value for i aligns well with theirs, but there is a notable 20°difference in the PA of LON. However, this is anticipated and can be attributed to the large-scale fits incorporating contributions from the entire bar and the asymmetric spiral arms of the galaxy (D. M. Elmegreen et al. 1996; P. Martini et al. 2003).

In the residual velocity map of the galaxy, inwards from the nuclear ring, three clumpy regions with negative velocity residuals of amplitudes ∼20–30 km s^{-1}, situated ∼1 arcsec towards the north-east, south-east, and south-west from the centre are exposed. The northern region exhibits the strongest amplitudes. While these three regions resemble $m = 3$ harmonic terms, raised from wrongly fitted i in the disc model, they also coincide with the local velocity peaks seen in the original velocity maps, and therefore they are real and driven by the data. None of these regions overlap with the dust spirals inside the nuclear ring. External to the nuclear ring, we notice a coherent structure with negative velocities, with amplitudes around ∼30–40 km s^{-1}, winding from ∼15 arcsec east of the centre towards the north-west, coinciding with one of the faint dust lanes downstream from the main dust lane. Where this coherent structure ends, ∼10 arcsec north-west of the centre, a round region with high positive residual velocities, with amplitudes exceeding 50 km s^{-1}, is seen. This region coincides with enhanced Hα and [N II]λ6583 emission and low velocity dispersion.

Inwards from the nuclear ring, the velocity difference map reveals two peaks, one with positive and one with negative values, with amplitudes of ∼15–25 km s^{-1}. Both peaks are located at a similar distance, ∼4 arcsec from the centre, one towards the north-east and the other towards the south-west. These two peaks also appear to have an extension of elevated velocity difference amplitudes in the clockwise direction. Considering their similar distances from the centre, and the possible extended natures, these two kinematic structures can be counterparts of one another. Outside the nuclear ring, where velocity residuals were showing an increase, the velocity differences are also coherent, exhibiting amplitudes around ∼20–30 km s^{-1}. This trend persists throughout the dust lane. However, once reaching the round region, where enhanced Hα and [N II]λ6583 emission and low velocity dispersion are seen, the amplitudes are ∼0 km s^{-1}; around this region, the velocity differences remain consistent with those observed in the dust lane.

The core of NGC 1300 is classified as a weak low-mass AGN (J. W. Atkinson et al. 2005; M. A. Hughes et al. 2005). As shown in the BPT map of the galaxy, the nuclear ring exhibits composite emission with contribution from SF, with the most significant SF occurring in the north-west. Inwards from the nuclear ring, ionization is predominantly driven by high-energy mechanisms. Outside the nuclear ring, two clumps, each showing contribution from SF, are observed – one ∼10 arcsec north-west of the centre and the other ∼6 arcsec south of the centre. These structures coincide with round regions displaying enhanced Hα and [N II]λ6583 emission. Considering high residual velocities co-spatial with the structure at the north-west, and elevated velocity differences surrounding it, we hypothesize that this structure can be a young star cluster moving with respect to the surrounding medium of different physical conditions.

Although NGC 1300 shows a clear coherent spiral structure in dust that can be traced down to ∼1 arcsec from the nucleus, this structure does not appear to have a coherent kinematic counterpart. The kinematic structures in the residual velocity and velocity difference maps are likely the result of local shocks and are not associated with extended shocks.

A5 NGC 1433

The images and diagnostic maps of NGC 1433 are shown in Fig. A5(a). The large-scale image of the galaxy reveals a luminous core, a prominent nuclear disc, an outer bar, an inner ring surrounding the outer bar region, outside of which there are two or possibly four spiral arms. The MUSE FOV, shown in the colour image of the galaxy, covers the core, the nuclear disc and roughly half of the bar. There remains a subject of ongoing debate about whether NGC 1433 hosts an inner bar. While several photometric (P. Erwin 2004; R. J. Buta et al. 2015) and kinematic (A. Bittner et al. 2019) studies present evidence in favour of an inner bar, contrasting kinematic studies challenge its existence (A. Lorenzo-Cáceres et al. 2019; A. Bittner et al. 2021). Along the outer bar, two prominent dust lanes are seen which curve around the nuclear disc. Moreover, a faint dust lane is seen following the same pattern as the dust lane to the south-west, yet it extends further beyond and connects to the dust lane to the north-east. Further inwards, there are several dust spiral arms within the nuclear disc, curving towards the centre. These dust features are more clearly seen in the unsharp mask image of the galaxy, where they appear as a continuation of the straight dust lanes along the outer bar.

The [N II]λ6583 flux, velocity, and velocity dispersion maps of NGC 1433 referred to in the paragraph below show the measurements obtained from single Gaussian fits, presented in Appendix B, first row of Fig. B1. Hα and [O III]λ5007 flux, velocity and velocity dispersion measurements can be represented with the maps shown in the main diagnostic maps presented in Fig.A5(a). These measurements are obtained from fits including a secondary component to [N II]λ6583, yet Hα and [O III]λ5007 are not affected by this correction. More details on this are provided in the following paragraph.

As shown in the flux maps, presented in Fig. A5(a) and in the first row of Fig. B1, emission across all line groups is confined within the nuclear disc. The strongest emission comes from the core, confined within ∼3–5 arcsec radius for Hα and [N II]λ6583 emissions, and within ∼3 arcsec radius for [O III]λ5007. There is no nuclear ring in Hα or [N II]λ6583 emission. Within the nuclear disc, distinct clumpy regions with enhanced Hα and [N II]λ6583 emissions are seen. One of the most prominent of these regions is seen as a single blob at ∼9 arcsec south-east of the centre. Another notable region with enhanced emission is characterized by three maxima and is situated ∼6–8 arcsec south-west of the centre. In comparison to Hα emission, the [N II]λ6583 emission from these regions is weaker. These regions also exhibit elevated [O III]λ5007 emission. The velocity maps of all emission line groups exhibit signs of non-circular motions, with indents in the zero-velocity-line characteristic to strong streaming motion in the spiral arms. Outer parts of the nuclear disc, at ∼8 arcsec, have the smallest velocity dispersion with ∼60 km s^{-1}. Throughout the nuclear disc, where enhanced clumpy Hα and [N II]λ6583 emissions are seen, the velocity dispersion of Hα and [N II]λ6583

Downloaded from academic.oup.com/mnras/article/552/3/stag1204/8721813 by guest on 30 October 2026

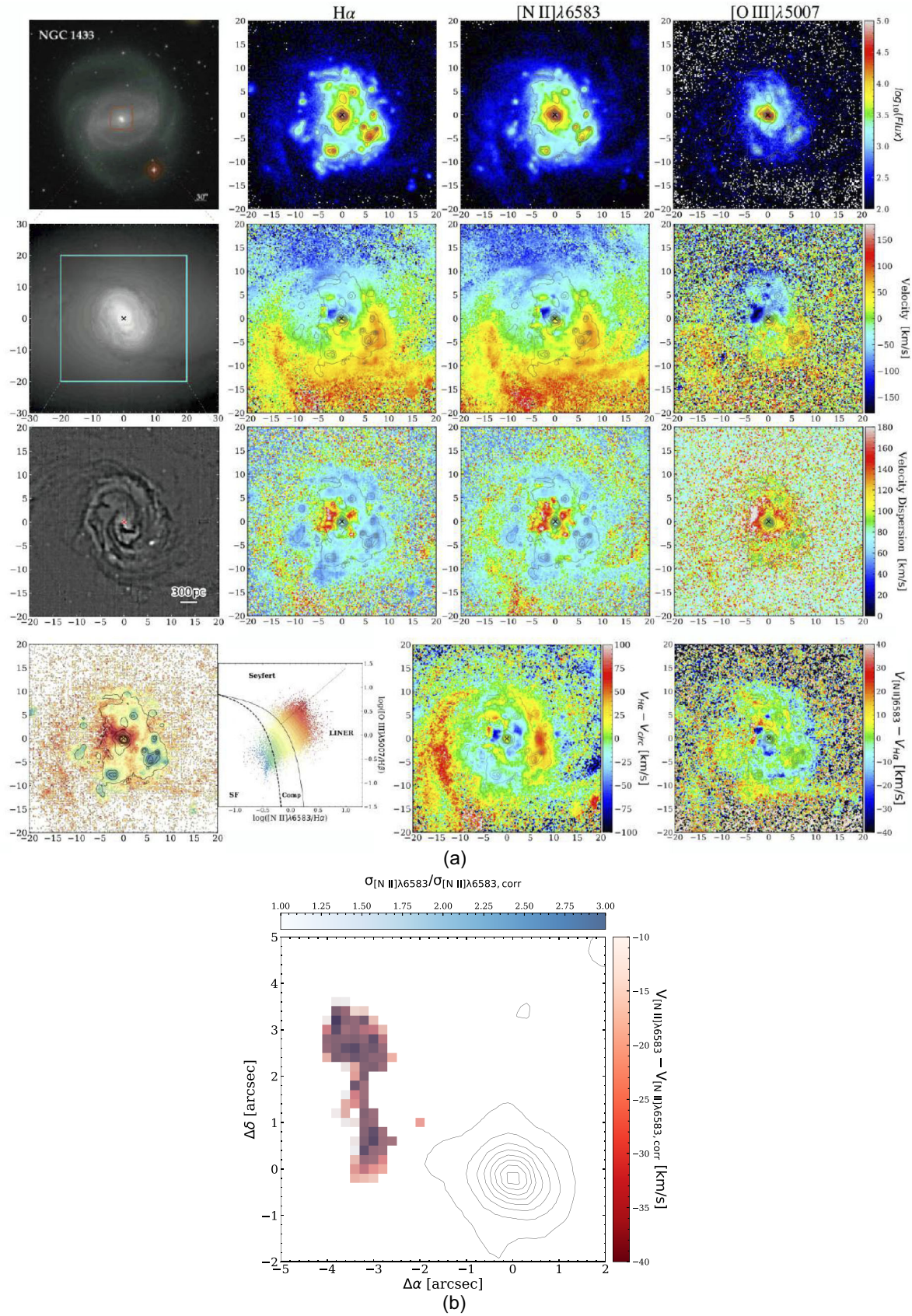

Figure A5. (a) Images and diagnostics maps of NGC 1433. Panels show the same as in Fig. 2. (b) The mask of spaxels for which the fits including secondary component were used in further analysis of NGC 1433. The red and blue colour maps show the velocity shift of [N II]λ6583 and the ratio of [N II]λ6583 velocity dispersion, respectively, before and after including the secondary component in the fitting.

Downloaded from academic.oup.com/mnras/article/552/3/stag1204/8721813 by guest on 30 October 2026

remains around ∼60–70 km s^{-1}. Closer to the nucleus, there is an extended region (5 arcsec across) of high velocity dispersion to the east and two small ones (∼2 arcsec in size) to the west where high dispersion values exceed ∼150 km s^{-1}. These regions also exhibit anomalous Hα and [N II]λ6583 velocities. Due to poor [O III]λ5007 emission, the velocity dispersion values within the nuclear disc are not reliably estimated, but in the regions with high Hα and [N II]λ6583 velocity dispersion, values are also elevated for [O III]λ5007.

The high velocity dispersion in the nucleus prompted us to examine the Gaussian fits in the corresponding spaxels. As we explained in Section 3.2.1, if there are multiple emission sources along the LOS, which can appear as excess emission in the spectra, the standard single Gaussian fitting approach will produce a poor and broad fit in the spectra of spaxels that are affected from the excess emission. Such poor fits correspondingly can shift the recorded velocity of main lines, and can artificially increase the velocity dispersions. Correspondingly, the artificial measurements can significantly influence the residual velocity and velocity difference maps we construct to search for the signatures of extended shocks. Upon checking the spectra, we noticed that spectra in several spaxels within the inner ∼3 arcsec radius are poorly fitted due to an excess emission in the blue wing of the [N II]λ6583 line. Therefore, to address this excess emission, we followed the same procedures introduced in Paper IV, and allowed for fitting a secondary component to [N II]λ6583.

Further, we compare the kinematic measurements obtained from single Gaussian fits and fits including a secondary component to determine regions that are the most affected by the excess emission. In general, Hα and [O III]λ5007 are not affected throughout the entire FOV. However, within a localized region extending from ∼3 arcsec east of the centre ∼4 arcsec towards the north, the introduction of the secondary component shifts the derived velocity of [N II]λ6583 significantly, by ∼15–20 km s^{-1}. The velocity dispersion of [N II]λ6583 in this region remains high. This region is presented in Fig.A5(b), after certain mask conditions are applied which we explain below.

Therefore, by establishing the criteria explained further, we determine the region where the fits to spaxels are the most affected by the excess emission, to correct the [N II]λ6583 kinematic measurements in the regions, by using the values for the main component from the fits that include a secondary component there. The criteria are as follows:

(i) $V_{[N\,II]} - V_{[N\,II],corr} \leq -10$ km s^{-1}
(ii) $\sigma_{[N\,II]}/\sigma_{[N\,II],corr} \geq 1.2$
(iii) $\sigma_{[N\,II]w} \leq 300$ km s^{-1}
(iv) $-4'' \leq \Delta\alpha \leq -1''$ and $-1'' \leq \Delta\delta \leq 4''$

where *corr* indicates the values extracted from the fits including the secondary component. The third condition, the velocity dispersion limit of the secondary [N II]λ6583 component ([N II]w) ensures that the secondary component is real and is not fitted to noise. The spatial cuts are applied to select the region where the change in velocity and velocity dispersion ratio is consistently large. For further analysis, the flux, velocity, and velocity dispersion values for all emission line groups within the mask region are replaced with those from the corresponding main components in fits that include the secondary component. Although Hα and [O III]λ5007 measurements are not affected, we continue to use measurements from fits with a secondary component to maintain consistency. The corrected flux, velocity and velocity dispersions maps of all line groups are presented in Fig. A5(a).

When run with a fixed centre the distributions of the i and PA of the LON obtained from KINEMETRY show strong variation with radius. Therefore, we adopted initial values PA of the LON = 19.7°and i = 29°from the large-scale study P. Lang et al. (2020), and by adjusting these values with small increments, we ran KINEMETRY with different fixed PA of the LON and i values to identify the values that raise the minimum level of artefacts in the residual velocity map. Despite these adjustments, we did not observe a significant change in the residual velocity map. Therefore, we selected the initial parameter values as the final i and PA of the LON.

In the residual velocity map of the galaxy, there are several pronounced coherent structures within the nuclear disc. One of these structures exhibiting positive velocities with amplitudes of ∼30–50 km s^{-1}, forms an arch ∼8 arcsec west of the centre, extending for over 15 arcsec. The corresponding deprojected residual velocity amplitudes across this structure reach up to 115 km s^{-1}. A possible counterpart to this structure, exhibiting negative velocities, extends from ∼10 arcsec south of the centre towards the north-east, exhibiting deprojected residual velocity amplitudes around 70–80 km s^{-1}. Both structures align well with the outer curvature of the nuclear disc, and the dust lanes. Another coherent structure with negative velocity residuals is seen, with residual velocity amplitudes around 40–50 km s^{-1}, forming an arch ∼4 arcsec west of the centre extending almost 10 arcsec. Across the extent of this structure, the deprojected residual velocity amplitudes are high, reaching up to 115 km s^{-1}. The largest amplitude of this structure coincides with one of the peaks of Hα and [N II]λ6583 velocity and velocity dispersion. Moreover, throughout the extent of this structure, the [N II]λ6583 velocity dispersion is ∼30–40 per cent larger than that of Hα. Between ∼2 and ∼5 arcsec to the north-east of the nucleus there are clumpy regions of high negative and positive velocity residuals – they are likely related to the AGN outflows, explained further below. In addition, throughout the nuclear ring, several other regions exhibit high residual velocity amplitudes. However, these regions rather have an amorphous structure and are likely originating from local SF. Outwards from the nuclear ring, extending from the south-east of the centre towards the north-east for ∼20 arcsec, a coherent structure forms an arch, exhibiting velocity residual amplitudes around ∼30 km s^{-1}, with corresponding deprojected residual velocity amplitudes around 80–90 km s^{-1}. This structure coincides with the faint dust lane seen in the same region, likely indicative of overshot gas.

In the velocity difference map of the galaxy, regions of high positive and negative values are seen to the south and south-east of the nucleus, where the velocity dispersion is high. In addition, several clumpy regions with enhanced velocity differences, up to ∼20 km s^{-1} are seen throughout the nuclear disc, that do not particularly coincide with the structures seen in the residual velocity map.

The classification of the galaxy's core remains the subject of a debate (M. P. Veron-Cetty and P. Veron 1986; R. M. Sosa-Brito et al. 2001). Nevertheless, the contribution from the AGN to the ionization is evident in the BPT map of the galaxy. Up to ∼4 arcsec radius, in two regions exhibiting a distinct horizontal biconical shape, characteristic to AGN outflows, the ionization is primarily influenced by a high-energy mechanism. Particularly along east–west direction, in the regions where the velocity dispersion is high. A part of this region coincides with where we corrected for excess emission in the fitting, indicating the excess emission seen

Downloaded from academic.oup.com/mnras/article/552/3/stag1204/8721813 by guest on 30 October 2026

in this region is likely originating from AGN outflows. Furthermore, throughout the nuclear disc, there is composite emission with a contribution from SF. The regions with the strongest SF, to the south-east and south-west, are co-spatial with the most prominent Hα and [N II]λ6583 enhancements seen in emission. These coincide with the two coherent structures with high positive and negative residual velocity amplitudes, situated at the curvature of the nuclear disc. These alignments are indicative of SF being triggered by enhanced gas density at the leading side of the bar and provide evidence of large-scale extended shocks propagating within those regions.

Within the nuclear disc of NGC 1433, the residual velocity map exhibits multiple elongated structures, some confined to galactocentric radii of a few hundred parsecs and others extending out to a few kiloparsecs (see also features outlined in Fig. 3). These features show large deprojected residual velocity amplitudes, reaching $\sim$100 km s^{-1} and coinciding with dust spirals. These features together resemble a nuclear spiral shock, but they lack the continuity expected from such a shock signature. Nevertheless, the alignment of the dust structures with features seen in residual velocity, together with enhanced velocity differences and the elevated SF activity occurring in these features can all be associated with extended shocks in gas. We hypothesize that strong SF activity within the nuclear disc and potentially the AGN activity, interrupt the propagation of the shock, leaving portions of it visible in the residual velocity map. Therefore, based on the grouping described in Section 5.3, this galaxy is classified under *extended shocks* kinematic category.

A6 NGC 1566

The images and the diagnostic maps of NGC 1566 are presented in Fig. A6. As shown in the large-scale and colour images, NGC 1566 has a bright core, which is classified as Seyfert 1.2 type based on its optical broad line ratio, yet also exhibiting optical narrow line ratio typical of Seyfert 2 cores (D. Alloin et al. 1985; G. A. Kriss et al. 1991; S. Smajić et al. 2015). The galaxy also has a weak bar (G. Vaucouleurs et al. 1991; K. Sheth et al. 2010), and two or possibly four star-forming spiral arms encircling the bar region. The MUSE FOV encompasses the core and the entire bar. In the bar region, originating in the north and south, there are dust lanes winding in clockwise direction. These dust features are more prominent in the unsharp mask image. Particularly, within the inner 15 arcsec, we notice the multiplicity of spiral arms in clockwise direction.

As presented in the flux maps, the emission across all line groups is concentrated within $\sim$3 arcsec radius. In the bar region, two strong lanes of emission are seen with clumpy Hα and [N II]λ6583 emission; some of these regions align as a straight line, likely indicating enhanced SF within the bar lanes. The Hα emission in these regions is stronger than [N II]λ6583 emission. We do not discern a nuclear ring in emission. [O III]λ5007 emission beyond the inner $\sim$3 arcsec region significantly weakens. However $\sim$8 arcsec from the centre towards south–south-east enhanced [O III]λ5007 emission is seen; since there is no counterpart to this structure seen in any other emission, it is likely originating from AGN outflows.

The velocity maps reveal significant non-circular motions of no clear pattern across all emission line groups. In the [O III]λ5007 velocity map, $\sim$4–8 arcsec from the centre, at PA $\sim$160°, a region of high negative velocities (up to $\sim$300–400 km s^{-1}) occurs at the location of enhanced [O III]λ5007 emission, confirming its origin being AGN outflows. There is also a blueshifted quasi-linear structure $\sim$10 arcsec to the south-west of the nucleus, co-spatial with a filament seen in [O III]λ5007, but not in Hα or [N II]λ6583, inconsistent with the spiral pattern, possibly related to the AGN outflows.

Within the $\sim$2 arcsec radius, an ambiguous round structure with high velocity across all line groups is seen. Upon closer examination of the spectra, within $\sim$1 arcsec radius of this region, we noticed strong broad emission primarily in the Hα and [N II] wavelength ranges, which can be attributed to the AGN. The emission from AGN was so strong that it even caused saturation in the innermost couple of spaxels. As a result, the Gaussians are not well fitted to the Hα and [N II] lines, indicating that the kinematic measurements derived from them are unreliable within the inner 1 arcsec. Broad emission is also seen in [O III]λ5007, but the Gaussian fits to [O III]λ5007 are still reliably fitted. Although the broad emission is associated with the characteristic of the AGN, there can also be a potential contribution from a small nuclear ring in that region, which has a size smaller than 100 pc, standing as one of the smallest nuclear rings ever found (C. Sá-Freitas et al. 2023). Nevertheless, the erroneous Gaussian fits due to broad emission in the spectra indicate that the measurements within the $\sim$1 arcsec radius are not reliable. The complexity of the broad emission extends beyond the standard approach of including a secondary component in the fitting process and requires careful attention to be addressed. Given that addressing this issue is beyond the scope of this work, we excluded the measurements within the 1 arcsec radius in our further analysis. In Fig. A6, the excluded spaxels appear as an empty white region with no measurements.

As shown in the velocity dispersion maps, within the $\sim$3–4 arcsec radius, beyond the excluded region, the velocity dispersion across all line groups is high, exceeding 150 km s^{-1}. In the bar region, particularly to the southwest, the velocity dispersions remain high, with values $\sim$100–130 km s^{-1} which can be related to AGN features explained above. Along the dust lanes in the bar region, the velocity dispersion of Hα and [N II]λ6583 decreases and remains around $\sim$50–70 km s^{-1}. Where strong blueshifted velocities are seen, to the south-west of the centre, the velocity dispersion of [O III]λ5007 is high, with values $\sim$170–200 km s^{-1}.

The disc orientation parameters estimated with KINEMETRY, i = 40°and PA of the LON = 37°, are consistent with the parameters estimated from large-scale fits from P. Lang et al. (2020), differing by approximately $\pm$5°(see Table 2). Therefore, we settle on these parameters in the final disc model. The residual velocity map of the galaxy reveals coherent continuous structures with velocities around $\sim$30 km s^{-1}. The structure with negative velocities is seen extending from the south of the centre towards the north-east. While a part of this structure curves towards the centre in the north-east, another part continues extending further north by another $\sim$5–6 arcsec. These structures likely reflect the inflow along the two dust lanes seen extending from the south towards the north. A counterpart, exhibiting positive residual velocities, extends from the north of the centre towards the west, coinciding with the dust lane to the north. Throughout the extent of these coherent structures, the deprojected residual velocity amplitudes are around 70–80 km s^{-1}. These large amplitudes further confirm the shock nature of the observed signatures in residual velocity maps.

In the velocity difference map, two extended regions are seen with amplitudes of $\sim$15–25 km s^{-1}; one extending from the

Downloaded from academic.oup.com/mnras/article/552/3/stag1204/8721813 by guest on 30 October 2026

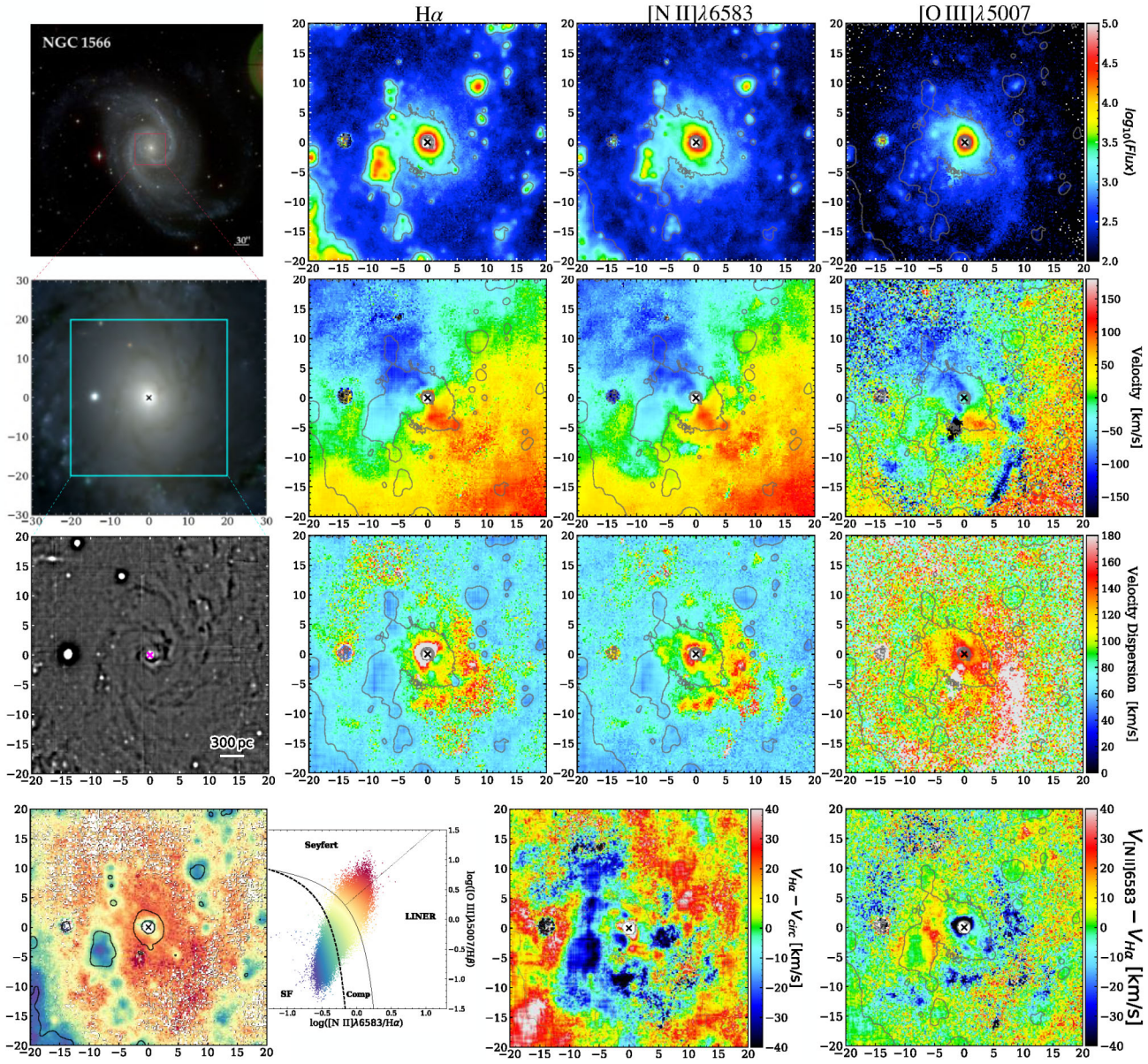

Figure A6. Images and diagnostics maps of NGC 1566. Panels show the same as in Fig. 2.

south-east towards north with positive velocity differences and the other extending from the north-west towards west with negative velocity differences. These two structures appear upstream from the two lanes seen in emission, and the coherent positive and negative residuals, by ∼1 arcsec .

As shown in the BPT map of the galaxy, the majority of the emission is of LINER/Seyfert type. The star-forming regions are rather in clumps grouped along several strings that largely correspond to the two lanes seen in emission. The region with the strongest SF coincides with the strongest Hα enhancement seen in emission, and with a portion of the coherent structure with negative residual velocities. Moreover, in the region where the coherent structure with negative residual velocities continues further north, several aligned round regions with enhanced SF are seen.

Even though the presence of AGN outflows and the possible contribution from the small nuclear ring to the emission prevents us from resolving the propagation of shocks into the very core, there is compelling evidence of extended shocks within the inner kpc, along the bar lanes and curving towards the nucleus, reaching the innermost regions, down to the inner ∼2 arcsec region. As shown in Fig. 3 and Table 3, these structures extend across several kpcs and exhibit large deprojected residual velocity magnitudes of ∼70–80 km s^{-1}.

Even though the presence of AGN-driven outflows and possible emission from the small nuclear ring prevents us from resolving whether the shocks propagate into the very core, the residual velocity map provides compelling evidence for structures associated with extended shocks in the inner regions of the galaxy. Coherent elongated structures are observed along the bar dust

Downloaded from academic.oup.com/mnras/article/552/3/stag1204/8721813 by guest on 30 October 2026

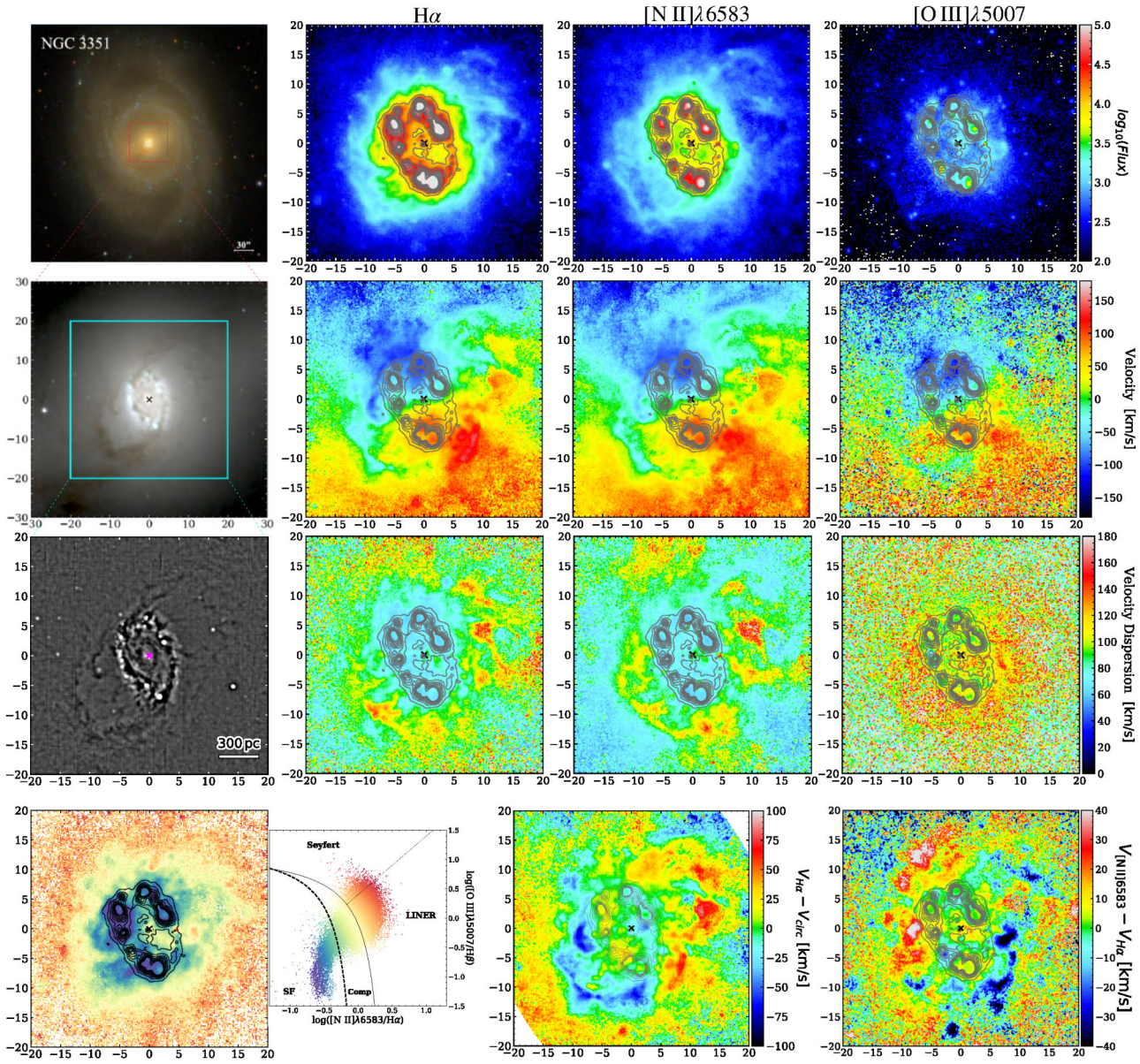

Figure A7. Images and diagnostics maps of NGC 3351. Panels show the same as in Fig. 2.

lanes, curving towards the nucleus and reaching down to the inner ∼2 arcsec region. As outlined in Fig. 3, these structures extend over several kiloparsecs and exhibit large deprojected residual velocity magnitudes of ∼70–80 km s^{-1}. Their large spatial extent, coherent morphology, and high residual velocities therefore support their interpretation as extended shocks. Therefore, based on the grouping described in Section 5.3, this galaxy is classified under *extended shocks* kinematic category.

A7 NGC 3351

NGC 3351 is a well studied galaxy (X. Mazzalay et al. 2014; D. A. Gadotti et al. 2019; R. Leaman et al. 2019; K. I. Smirnova and D. S. Wiebe 2019; D. Calzetti et al. 2021), and is one of the members of the Leo Group. The images and diagnostic maps of this galaxy are presented in Fig. A7. As shown in large-scale and colour images, NGC 3351 has a luminous core, a star-forming nuclear ring within the ∼10 arcsec radius, a prominent bar, an inner ring surrounding the bar region and two or more spiral arms surrounding the inner ring. The MUSE FOV encompasses the core, the nuclear ring and almost the entire bar of the galaxy. Along the bar, two faint dust lanes are seen; one of these extends from the north-west towards the centre and the other extends from the south-east towards the centre. These two dust lanes continue to curve within the nuclear ring over a full circle. Furthermore, within the bar region, an additional and more prominent dust lane is seen, manifesting an 'L' shape. More specifically, this dust lane appears just outside the nuclear ring, where it is initially almost parallel to the south-eastern lane and at ∼10 arcsec towards south from the centre becoming orthogonal to it. To the east and the west

Downloaded from academic.oup.com/mnras/article/552/3/stag1204/8721813 by guest on 30 October 2026

of the nuclear ring, several faint dust lanes are also seen. All dust structures are more prominently seen in the unsharp mask image of the galaxy.

As presented in the flux maps, the emission across all line groups is the strongest in the nuclear ring. Inwards from the nuclear ring the emission decreases, though it remains relatively high. In comparison to Hα and [N II]λ6583, the [O III]λ5007 emission is notably weak. The velocity maps of Hα and [N II]λ6583 show strong distortions from circular motion. Outside the nuclear ring, the zero velocity line has a strong indentation at ∼8-10 arcsec north-west and south-east from the centre. The indent is less pronounced in the O III velocity field, but there it extends further, all the way to the nuclear ring. As shown in the velocity dispersion maps, the velocity dispersion of Hα and [N II]λ6583 is the lowest in the nuclear ring, reaching around ∼50–60 km s^{-1} inside the nuclear ring the velocity dispersion values increase up to 90 km s^{-1} in the region ∼3 arcsec south-west of the nucleus. Outside the nuclear ring, the velocity dispersion values increase up to well above 120 km s^{-1}. The velocity dispersion values for [O III]λ5007 can not be reliably estimated due to poor signal, although even the noisy values suggest the same trends as in Hα and [N II]λ6583.

After fitting the rotating disc with KINEMETRY, i and PA of the LON converged to 46°and 23°, respectively. While the i aligns well with measurements from a large-scale study of P. Erwin et al. (2008) ($i = 46°$, PA of the LON $= 10°$), the PA of the LON slightly deviates from them. The residual velocity map of galaxy exposes two coherent structures with amplitudes of ∼50 km s^{-1}, one exhibiting negative and one exhibiting positive velocities. The feature with positive velocities can be traced from the right edge of the frame at $\Delta\delta$ ∼8 arcsec towards the northern tip of the nuclear ring, coinciding with one of the main faint dust lanes along the bar. The feature with negative velocities coincides with the L-shaped dust lane. Along the dust lanes within the nuclear ring, there are two more coherent structures, one with positive and one with negative velocities with amplitudes up to ∼50 km s^{-1}, corresponding to negative and positive deprojected velocities up to −95 and 50 km s^{-1}, respectively.

Furthermore, several other relatively extended structures with high residual velocity amplitudes are exposed to the east and west of the nuclear ring; one exhibiting negative and two exhibiting positive velocities. The structure with negative velocities has velocity amplitudes ∼40 km s^{-1}, and extends ∼6 arcsec north-east from the centre directly towards the south, coinciding with the faint dust lane observed to the east of the nuclear ring. The two other features with positive velocities, have velocity amplitudes above ∼50 km s^{-1}, each having roughly ∼5 arcsec extent that curves towards the west of the nuclear ring. This appearance of the residual velocity map challenges the textbook understanding of shocks in bars, as in NGC 3351 outside the nuclear ring their kinematic signatures extend along the bar only over a short distance, and then take a right-angle turn, past which they coincide with dust lanes *perpendicular* to the bar.

The velocity difference map of the galaxy exposes two coherent structures with amplitudes of ∼30–40 km s^{-1}, one at the west of the nuclear ring exhibiting negative velocity, and the other at the east of the nuclear ring exhibiting positive velocity. These two structures are among the structures with highest velocity difference amplitudes we observed in other galaxies we studied in this work; not related to AGN. They are consistent with the textbook picture of shocks in bars, they occur downstream from the dust lanes associated with those shocks, but their morphology shows little or no consistency with that of the velocity residuals. Inwards from the nuclear ring, near locations of the peak residual velocities, the velocity differences also show an increase, reaching amplitudes of ∼15–20 km s^{-1}.

The BPT map shows that the emission from the nuclear ring is strongly dominated by SF. Outside the nuclear ring, there is composite emission with a contribution from SF. Particularly, to the west of the nuclear ring, there is composite emission with a contribution from LINER emission. Inwards from the nuclear ring, towards the south-west of the nucleus, there is composite emission.

NGC 3351 exhibits clear signatures of extended shocks. As outlined in Fig. 3, these structures extend across several hundreds of parsecs, have elevated deprojected residual velocity magnitudes reaching ∼50–95 kms^{-1}, and they are cospatial with the coherent morphology of dust structures, especially inside the nuclear ring. Along with elevated velocity differences, there is dominating composite emission inwards from the nuclear ring. Therefore, even though these structures appear rather discontinuous, and are not continuously extending from outer regions towards the nucleus, we still associate them with extended shocks, dominating the inner kpc of the galaxy.

A8 NGC 3368

The images and the diagnostic maps of NGC 3368 are presented in Fig. A8. NGC 3368 belongs to the Leo Group together with the galaxy NGC 3351. As shown in the large-scale and colour images, the galaxy hosts a luminous dusty core and two bars – an outer bar with a length of 75 arcsec and an inner bar with a length of 5 arcsec (P. Erwin 2004; P. Erwin et al. 2015); in between the two bars, there is a nuclear disc (C. Möllenhoff and J. Heidt 2001; P. Erwin 2004; P. Erwin et al. 2015). The outer bar is surrounded by spiral arms. The MUSE FOV covers the core with roughly two-thirds of the outer bar. The dust structures around the core of the galaxy are more clearly seen in the unsharp mask image.

As presented in the flux maps, the strongest emission across all line groups is concentrated within the ∼3 arcsec radius, mostly to the east of the centre. The velocity field of all emission line groups does not exhibit strong perturbations; the zero velocity line remains relatively straight. Two structures, showing local velocity maxima, at PA 100°and −80°, extend radially by ∼8 arcsec. Another linear structure, showing velocity maxima, also at a PA −80°, is located slightly outside the frame, roughly at ∼20 arcsec from the centre. This structure has positive velocities, counter-rotating with respect to the surroundings.

As velocity dispersion maps indicate, the overall velocity dispersion of Hα and [N II]λ6583 is high, with values around ∼100–150 km s^{-1}. The regions with the highest dispersion, where values exceed 150 km s^{-1}, form a biconical structure extending from the centre towards the north-west and south-east. This structure is more prominently seen in the [N II]λ6583 velocity dispersion map. Another region with velocity dispersions exceeding 150 km s^{-1} appears towards the edge of the frame, where the gas is counter-rotating, as seen in the velocity map. The velocity dispersion values of [O III]λ5007 are overall noisy due to poor signal within the FOV, yet the values still suggest an increase along the biconical structure seen in Hα and [N II]λ6583 fields.

The disc orientation parameters estimated with KINEMETRY, $i = 46°$and PA of the LON $= 172°$, agree with estimations from large-scale studies (e.g. P. Erwin et al. 2008; $i = 50°$and PA of the LON $= 172°$). Upon analysing the residual velocity map of galaxy,

Downloaded from academic.oup.com/mnras/article/552/3/stag1204/8721813 by guest on 30 October 2026

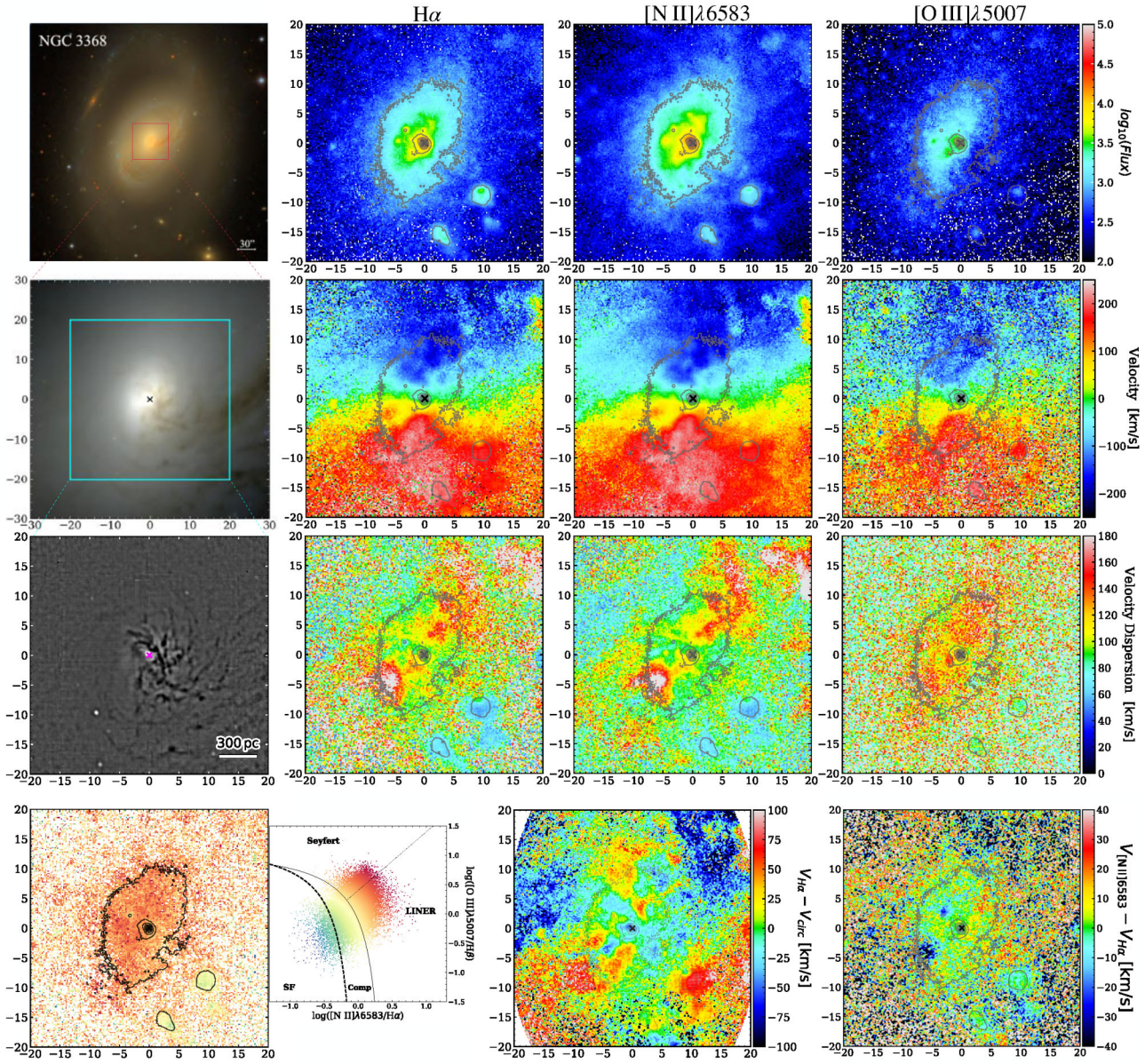

Figure A8. Images and diagnostics maps of NGC 3368. Panels show the same as in Fig. 2.

within the ∼5 arcsec radius towards the north-east, there are extended structures that show similar winding with dust spiral arms which may be related to the kinematics. Moreover, two structures, one with positive and one with negative velocities extend along the biconical structure seen in velocity dispersion, the highest amplitudes of velocity residuals roughly coincide with the highest velocity dispersion. The velocity difference map is noisy and does not exhibit coherent structures. However, where the highest velocity dispersion values are seen along the biconical structure, the velocity differences also show an increase. The region to the south-east exhibits negative velocity differences and the region to the north-west exhibits positive velocity differences, both with amplitudes around ∼20–30 km s^{-1}. The biconical morphology of the observed structure with extreme velocity dispersions, along with structures seen in velocity residual and velocity difference maps confirm that this structure outflows from the AGN. The counter-rotating portion of the gas is a consequence of the outflowing gas, moving in different conditions with respect to its surroundings.

Furthermore, the BPT map of the galaxy reveals that the ionization throughout the entire FOV is predominantly coming from the LINER emission with weak contribution from composite emission.

Although the galaxy is dominated by an AGN, which could potentially prevent identifying extended shocks near the nucleus, we have resolved structures within the innermost regions that are not obscured by AGN outflows. Generally, there is no compelling evidence of extended shocks within the inner kpc of NGC 3368. Therefore, based on the grouping described in Section 5.3, this galaxy is classified under *other perturbations* kinematic category.

Downloaded from academic.oup.com/mnras/article/552/3/stag1204/8721813 by guest on 30 October 2026

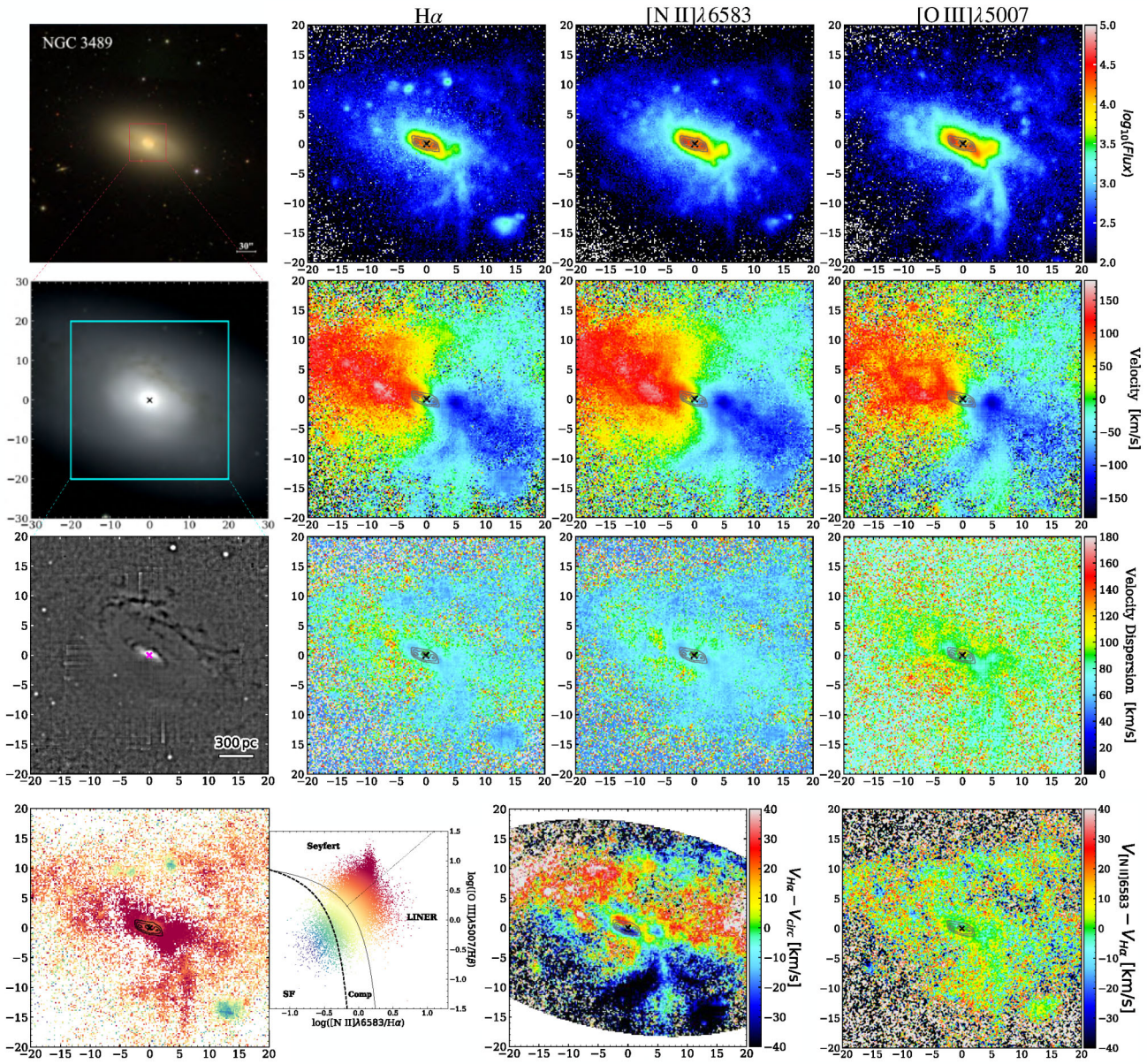

Figure A9. Images and diagnostics maps of NGC 3489. Panels show the same as in Fig. 2.

A9 NGC 3489

The images and the diagnostic maps of NGC 3489 are shown in Fig. A9. As presented in large-scale and colour images, NGC 3489 hosts a bright core, and a bar with ∼20 arcsec in size (P. Erwin and L. S. Sparke 2003), embedded in a dusty disc. The spectral classification of the galaxy's core falls within the Seyfert region (L. C. Ho, A. V. Filippenko and W. L. W. Sargent 1997; M. Sarzi et al. 2006). The MUSE FOV covers the core, the bar, and the disc. The unsharp mask image of the galaxy outlines a prominent dust spiral, originating from the west of the frame and circling the bar region in the counter-clockwise direction. Moreover, to the northeast and south-west, two very faint straight dust lanes are seen along the bar; these two lanes appear to connect a dusty ring of semimajor axis ∼3–4 arcsec.

As presented in the flux maps, the strongest emission across all line groups is mostly confined within the inner ∼5 arcsec. Within the radius of approximately ∼2–3 arcsec, the strongest emission exhibits several off-centred and elongated peaks, indicative of a small nuclear ring. A similar ring structure of size ∼3 arcsec is reported in former works (P. Erwin and L. S. Sparke 2003; N. Nowak et al. 2010). Within the same region, [O III]λ5007 emission is exceptionally strong, exhibiting quasi-radial extensions to the south-west, that may be related to shocks in the bar.

The velocity fields across all line groups reveal a wiggly zero velocity line, where it forms an 'S' shape within the ∼4 arcsec radius, associated with the characteristic flow in bars. There is also a peculiar 'blue arm', with negative velocities extending to the south-east, strongest in [O III]λ5007. As demonstrated in the

Downloaded from academic.oup.com/mnras/article/552/3/stag1204/8721813 by guest on 30 October 2026

the velocity dispersion maps, dispersion across all line groups is high in the nucleus, with values around ∼100–120 km s^{-1}. Within the nuclear ring, the velocity dispersion decreases; values remain consistent towards the south-west end of the frame. To the north-east and south-west of the centre, we discern two local velocity dispersion minima with values ∼50–60 km s^{-1}; these structures coincide with the off-centred peaks in emission. Throughout the dust spiral surrounding the bar region, the velocity dispersion values of Hα and [N II]λ6583 remain around ∼50–60 km s^{-1}, values for [O III]λ5007 cannot be estimated reliably due to poor signal in those regions, yet the dispersion is generally low.

After fitting the rotating disc to the Hα velocity field, the i and the PA of the LON converged to 60°and 80°, respectively. While i agrees well with the measurements estimated from large-scale fits, the PA of LON differs by 10°(e.g. P. Erwin et al. 2008; PA of the LON = 71°, i = 58°). However, when employing the large-scale PA of the LON in the disc model, artefacts of $m = 1$ harmonic terms appear in the residual velocity field. These artefacts were not observed when using values deduced by KINEMETRY in the model. Consequently, we chose to use the KINEMETRY inferred parameters in the final disc model.

The residual velocity map of the galaxy exposes two structures located ∼2 arcsec towards the north and south of the centre; one with negative and one with positive velocities, both exhibiting amplitudes ∼40 km s^{-1}. The largest deprojected residual velocity amplitudes observed across these structures are around 30–40 km s^{-1}. Both structures have an additional ∼2 arcsec extension towards north-east and south-west with weakened residual velocity amplitudes, ∼10–20 km s^{-1} —the deprojected residual velocity amplitudes in these regions are around 30 km s^{-1}. These extensions coincide with the faint dust lanes along the bar and they are consistent with shocks in gas. Moreover, strong residuals of radial extend, with values around ∼40–50 km s^{-1} or more, are also seen where there is quasi-radial emission.

The velocity difference map appears rather noisy, yet it does reveal very faint negative and positive velocities, with values around ∼5–10 km s^{-1}, within the ∼2 arcsec radius, coinciding with the regions with high residual velocity amplitudes. The aligning coherent structures of elevated velocity residuals and velocity differences, together with the aligning dust morphology, can be associated with extended shocks in gas, extending from the outer regions towards the core.

The BPT map of the galaxy reveals strong AGN dominance in the radiation from a Seyfert core. In the nuclear ring, there is a slightly reduced AGN contribution, coinciding with the region with low velocity dispersion, suggestive of the nuclear ring being fed by the inflowing gas. In literature, the galaxy is described as having a rejuvenated nucleus with a young central stellar population based on luminosity-weighted ages (F. Annibali et al. 2007), and this is further associated with the potential gas inflow within the central region towards the AGN (F. Annibali et al. 2010; A. Marino et al. 2011). Therefore, the interpretation of the coherent structures being extended shocks propagating towards the nucleus appears to align with these findings.

Generally, the overall emission in NGC 3489 seems to be of an AGN nature, but the gas flow is not affected by the AGN. The galaxy exhibits coherent structures extending over several hundred parsecs, which are outlined in Fig. 3, with deprojected residual velocity magnitudes reaching up to ∼40 km s^{-1}. We therefore associate these features with signatures of extended shocks.

A10 NGC 3626

NGC 3626 is one of the most complex galaxies in our sample. It is classified as an unbarred galaxy in G. Vaucouleurs et al. (1991), but several photometric studies show evidence of a double barred morphology (C. Möllenhoff and J. Heidt 2001; L. Gutiérrez et al. 2011); the inner bar is within ∼2–2.5 arcsec radius and outer bar is within ∼20 arcsec radius. Examining the stellar velocity dispersion and higher order moments of NGC 3626, which are presented in Fig.A10(a), we identify the velocity dispersion signatures, σ-hollows, characteristic to double-barred galaxies (see A. Lorenzo-Cáceres et al. 2008), agreeing well with the proposed orientation and size of the inner bar. Therefore, for further analysis, we settle on using double barred morphology for NGC 3626. The gas in the galaxy is counter-rotating with respect to the stars (R. Ciri, D. Bettoni and G. Galletta 1995; S. García-Burillo, M. J. Sempere and D. Bettoni 1998), which we confirm after comparing the stellar and gas velocity maps.

The standard images and diagnostic maps we use for the rest of the discussion of NGC 3626 are presented in Fig.A10(a). In the large-scale and colour images, it can be seen that NGC 3626 hosts a luminous core and an inner bar embedded in a dusty disc; the outer bar is not well defined in the colour image. The MUSE FOV covers more than half of the entire galaxy. As notably seen in the unsharp mask image, there are prominent dust lanes surrounding the outer bar region within the inner 20 arcsec.

As shown in the flux maps across all line groups, the emission within the ∼4 arcsec radius is relatively strong and extended towards the north-west and south-east direction, manifesting an 'S' shape. There is also strong and clumpy emission forming a boxy ring structure of ∼15 arcsec radius, coinciding with some of the dust lanes. Extending from the ends of the inner bar towards north-west and south-east, two lanes of emission connect to the boxy ring structure. These two emission lanes resemble the characteristic emission along the bar if gas were to rotate in the same direction as stars, but the gas is counter-rotating in that region. This indicates that the gas in NGC 3626 likely has two different origins.

As shown in the velocity maps, the velocity across all emission line groups shows peculiar structures. Overall the velocity maps follow the typical spider pattern, yet inwards from the boxy ring, there is a notable change in the PA of the zero velocity line. Within the ∼5 arcsec radius, the PA of the LON is around 130°, while beyond this region, the PA of the LON is almost perpendicular to the zero velocity line, measuring ∼160°. This shift in the PAs suggests that the gas is moving in two different planes, indicating likely two different origins. At ∼3 arcsec towards the north-west and south-east from the centre, two local velocity peaks are seen.

Throughout the boxy ring, the velocity dispersion of Hα and [N II]λ6583 remains around 50 km s^{-1}. Inwards from the boxy ring, the velocity dispersions are generally high, with the highest values being in the core. Almost perpendicular to the inner bar, a region extending from the centre towards ∼4 arcsec east and west, shows consistently high velocity dispersions, with values around ∼130 km s^{-1}; in certain spaxels values even exceed ∼150 km s^{-1}. Additionally, situated ∼1–2 arcsec beyond the endpoints of the inner bar, the velocity dispersions are also high, with values around 130 km s^{-1}. This observation further confirms the presence of two kinematically distinct regions inwards from the boxy ring, supporting the argument for gas having two different origins

Downloaded from academic.oup.com/mnras/article/552/3/stag1204/8721813 by guest on 30 October 2026

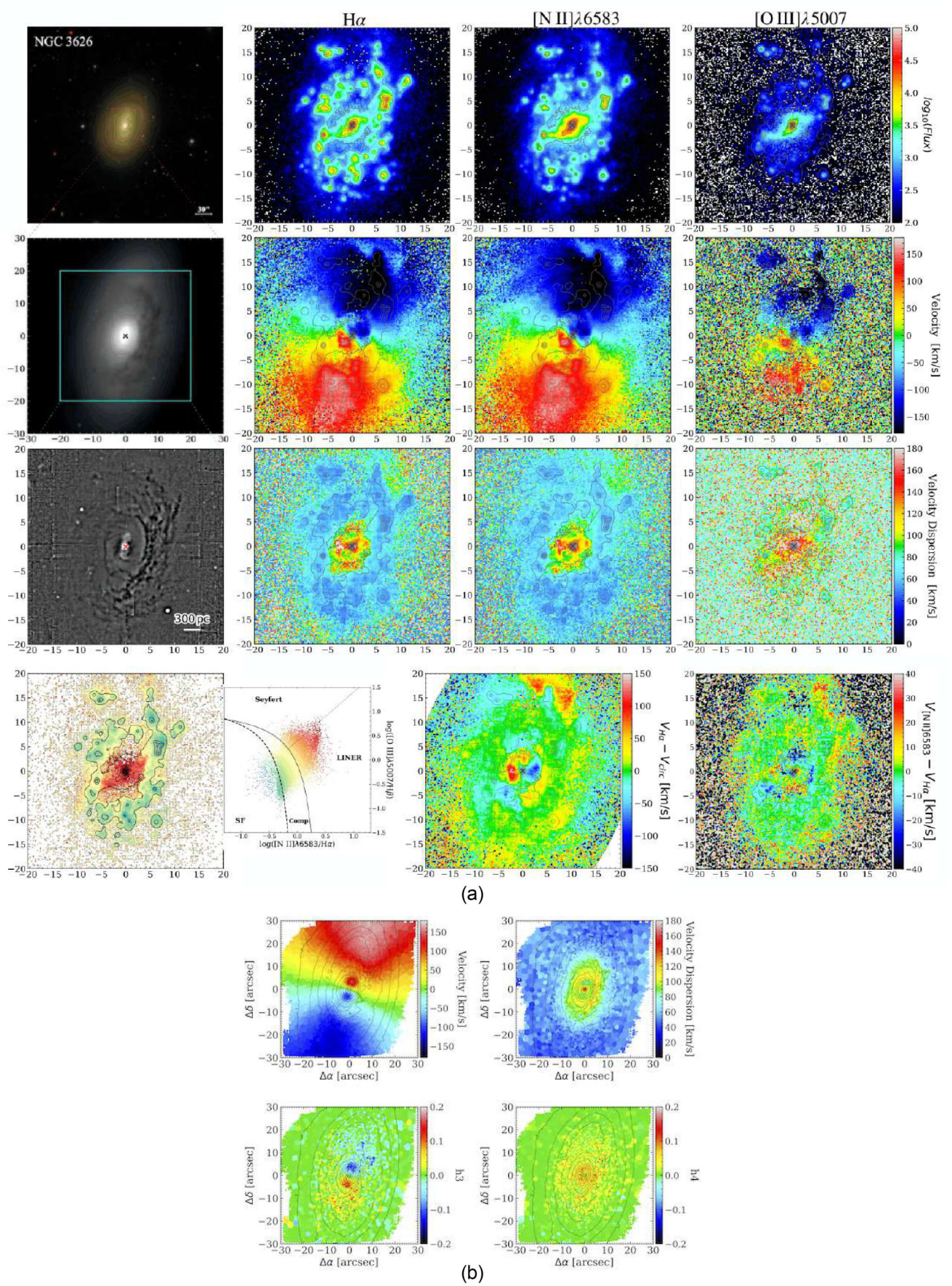

Figure A10. (a) Images and diagnostics maps of NGC 3626. Panels show the same as in Fig. 2. (b) NGC3626. Panels show the same as in Fig. 1.

Downloaded from academic.oup.com/mnras/article/552/3/stag1204/8721813 by guest on 30 October 2026

there. The velocity dispersion of [O III]λ5007 is not reliably estimated due to poor signal, but the values generally show a similar trend to Hα and [N II]λ6583 velocity dispersion values.

While the distributions of PA of the LON and i obtained from KINEMETRY strongly vary inwards from the boxy ring, the distributions estimated outwards from the boxy ring converge around $i = 53°$and the PA of the LON $= 163°$, which agree well with the values estimated from large-scale photometric fits in CBS (see Table 2). This indicates that outwards from the boxy ring, the gas is moving within the galaxy plane, while inwards from the boxy ring, the gas is moving out of the galaxy plane and can not be described by a planar motion. Consequently, the velocity residual map of the galaxy reveals distinct artefacts of wrongly fitted PA of the LON, m= 1 harmonic terms, inwards from the boxy ring. Despite attempting various parameter adjustments for fitting the rotating disc better inwards from the boxy ring, these artefacts persisted and were not minimized. Although several extended structures are present throughout the boxy ring, they do not exhibit a turning behaviour towards the inner regions.

The velocity difference map is noisy and does not show prominent extended structures. However, only within ∼1–2 arcsec radius, we notice a blue and a red structure with residual velocity amplitudes ∼20 km s^{-1}, possibly counterparts of one another, though these structures are rather amorphous. Moreover, from the centre ∼4 arcsec towards the north and south, there are also two regions with elevated velocity differences, one region exhibiting negative and the other region exhibiting positive velocities, with amplitudes ∼15–20 km s^{-1}.

As shown in the BPT map, inwards from the boxy ring, the ionization is dominated by the AGN, where there is mostly LINER emission. Throughout the boxy ring, there is composite emission with weak contribution from star formation.

The complex nature of kinematically distinct gas regions within NGC 3626, prevents us from accurately modelling the disc inwards from the boxy nuclear ring; thus the residual velocity map of the galaxy was dominated by the artefacts. Although we identify emission along the inner bar and a possible flow along the inner bar from the velocity difference map, these structures are rather weak to be interpreted as extended gas shocks. Therefore the galaxy is not exhibiting signatures of extended shocks and based on the grouping explained in Section 5.3, it is classified under *other perturbations* category.

A11 NGC 4237

The diagnostic images and maps of NGC 4237 are presented in Fig. 10. NGC 4237 is a member of the Virgo Galaxy Cluster (R. B. Tully 1988). As shown in its large scale image the galaxy is unbarred and has prominent star formation and dusty spiral arms encircling its bright core. The MUSE FOV covers almost the entire galaxy. The dust structures in spiral arms are enunciated in the unsharp mask image.

As shown in the flux maps, there is clumpy emission across all line groups forming a broken spiral structure. The Hα emission, likely originating from SF, is significantly stronger compared to [N II]λ6583 and [O III]λ5007. The velocity maps of Hα and [N II]λ6583 are relatively unperturbed, exhibiting motion close to circular. The Hα and [N II]λ6583 velocity dispersions remain around ∼50 km s^{-1} across the whole FOV.

The PA of the LON $= 107°$and $i = 53°$obtained from KINEMETRY agree well with the same parameters estimated in large-scale studies (L. Chemin et al. 2006), as shown in Table 2. Residual velocity map of the galaxy exposes weak quasi-spiral structures, with amplitudes of ∼5–10 km s^{-1}, corresponding to deprojected residual velocity amplitudes of ∼20 km s^{-1} or lower. Due to their low velocity amplitudes, we do not interpret these structures as extended shocks. Across the entire FOV, the velocity difference map is noisy. In this map, we observe a weak m=1 signature of amplitude ∼5–10 km s^{-1} mirroring the velocity distribution, which for a presumably single-component gaseous medium may indicate a slight offset between the derived Hα and [N II]λ6583 velocity fields that is proportional to the velocity magnitude. This further confirms the absence of extended shocks in the field.

The BPT map of the galaxy exhibits predominant SF in multiple spiral arms, together with some composite emission. Several round regions show the emission of the LINER type, coinciding with the regions with enhanced [N II]λ6583 velocity dispersion, which may indicate local shocks.

NGC 4237 has relatively unperturbed kinematic fields and does not exhibit signatures of extended shocks.

A12 NGC 4303

The diagnostic images and maps of NGC 4303 are presented in Fig. 2. As the large-scale and colour images show, the galaxy has a luminous core surrounded by a star-forming nuclear ring of ∼3 arcsec radius (L. Colina and K. Wada 2000). This galaxy also has a nested bar system; an inner bar of ∼2 arcsec radius and an outer bar of ∼20 arcsec radius (S. Laine et al. 2002; E. Schinnerer et al. 2002), the outer bar is encircled by spiral arms. The MUSE FOV, covers the core, the nuclear ring and two bars. As enunciated in the unsharp mask image, two prominent dust lanes along the outer bar are connecting to the nuclear ring; inwards from the nuclear ring, the dust lanes along the inner bar are also visible.

The [N II]λ6583 flux, velocity, and velocity dispersion maps of NGC 4303 referred to in paragraph below show the measurements obtained from single Gaussian fits, presented in Appendix B, second row of Fig. B1. Hα and [O III]λ5007 flux, velocity, and velocity dispersion measurements can be represented with the main diagnostic maps presented in Fig. 2. These measurements are obtained from fits including secondary component to [N II]λ6583, yet Hα and [O III]λ5007 are not affected by this correction, more details on this are provided in further paragraphs.

As shown in Figs 2 and B1 (second row), the strongest emission across all line groups is confined within the nuclear ring and the core. Outside the nuclear ring, there is clumpy Hα and [N II]λ6583 emission; Hα being stronger. The velocity field of all emission line groups reveals perturbations superimposed on the circular rotation, clearly manifested in the rugged zero velocity line. Also, ∼5–10 arcsec west to north-west of the nucleus, where the velocities are anticipated to be redshifted, several regions with blueshifted velocities are seen, most notably in [N II]λ6583 and [O III]λ5007. In the [O III]λ5007 velocity map, there is also a region with strong blueshifted velocities, extending from the centre ∼7 arcsec towards the south, suggesting a contribution from outflows. Inwards from the nuclear ring, the velocity dispersion values are up to ∼100 km s^{-1} in Hα and up to ∼150 km s^{-1} in [N II]λ6583 in two peaks ∼2 arcsec offset from the centre. In the nuclear ring and to the east of it, there is low Hα and [N II]λ6583 velocity dispersion, with values around ∼ 60 km s^{-1}. Outside the nuclear ring, both Hα and [N II]λ6583 velocity dispersion values are generally around 60–80 km s^{-1}, but to the north-west and south-east of the centre, the values are high, around 100–130 km

Downloaded from academic.oup.com/mnras/article/552/3/stag1204/8721813 by guest on 30 October 2026

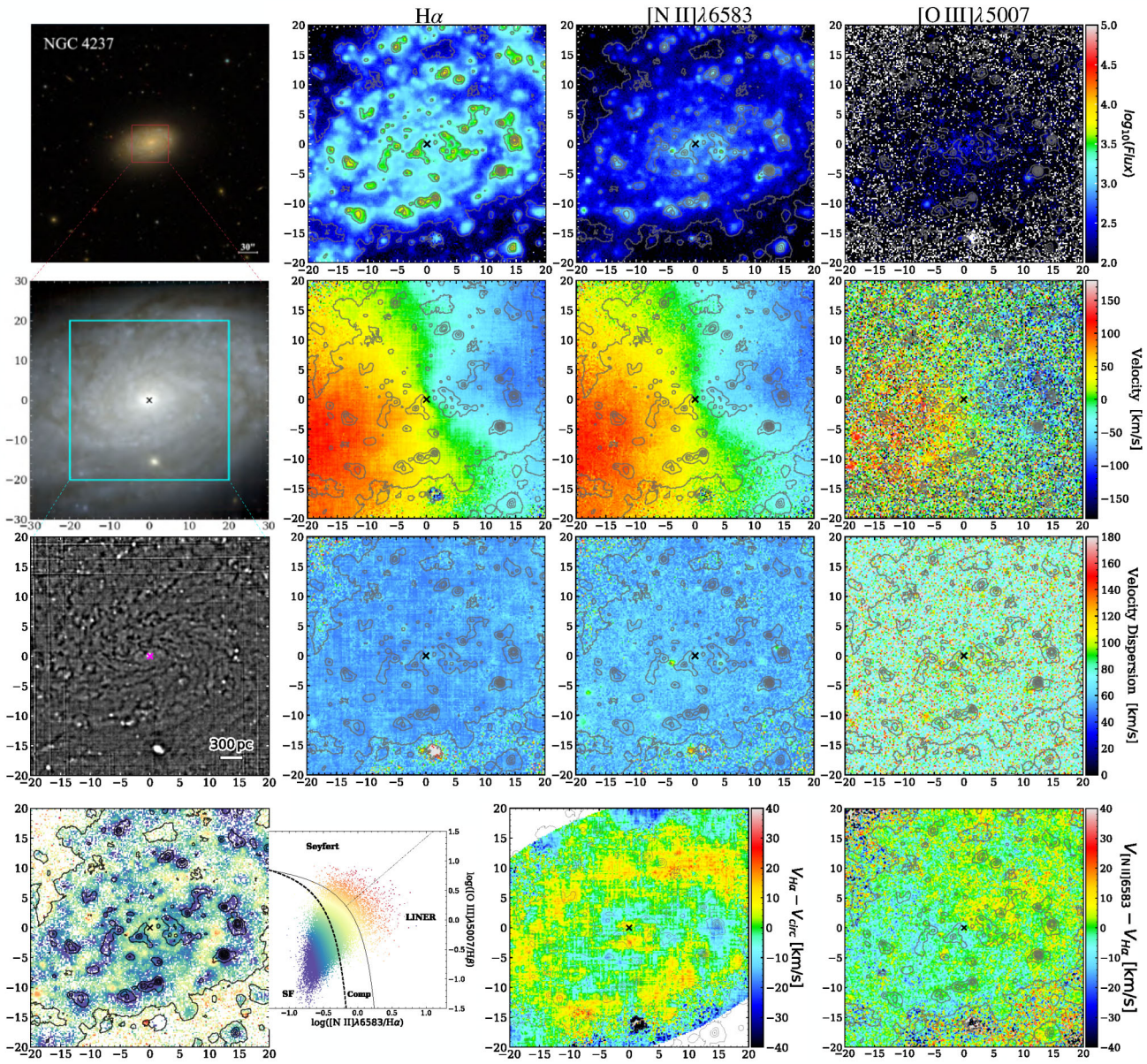

Figure A11. Images and diagnostics maps of NGC 4237. Panels show the same as in Fig. 2.

s^{-1}. Particularly, in a small region ∼7 arcsec to the north-west of the centre, the [N II]λ6583 velocity dispersions reach their highest values, exceeding 200 km s^{-1}. The [O III]λ5007 velocity dispersions, exhibit values over 200 km s^{-1} in a ring of ∼1–4 arcsec around the centre, and ∼6 arcsec extension to the south. The region extending to the south coincides with the strong blueshifted [O III]λ5007 velocities.

The high velocity dispersion of [O III]λ5007 prompted us to search for an excess emission in the spectra, and the Gaussian fits. If there is an excess emission in the spectra, fitting the excess and the main emission line with single Gaussians is not sufficient. The fitted Gaussian will be broad and will artificially increase the velocity dispersion and alter the velocity of the main emission line. Upon closer examination of the spectra where velocity dispersion of [O III]λ5007 is high, we noticed a weak asymmetry in the [O III]λ5007 line profile. To ensure this asymmetry does not artificially influence the measurements, following the same concept introduced in Paper IV, we allowed for fitting a secondary component to [O III]λ5007. If the emission is dominated by two components along the LOS, coming from both the excess emission sources and the disc, fitting two components will allow separating them. After allowing to fit a secondary component to [O III]λ5007, in the region where highly blueshifted [O III]λ5007 velocities and high [O III]λ5007 velocity dispersions are seen, we did not notice a significant [O III]λ5007 velocity shift. The velocity dispersion of [O III]λ5007 in the same region was reduced by 30–40 per cent; despite this reduction, the values remained high, confirming that the disturbance of the [O III]λ5007 is real. The extreme kinematics of [O III]λ5007 likely indicate a contribution from AGN outflows. Since kinematics are not significantly affected by the excess emission, to reduce the number of free parameters of the fit we only use single Gaussians to fit [O III]λ5007.

Downloaded from academic.oup.com/mnras/article/552/3/stag1204/8721813 by guest on 30 October 2026

Not only in [O III]λ5007 but high velocity dispersions are also seen in [N II]λ6583. Thus, to ensure these values are real, following the same concept and procedure in Paper IV, we allowed for fitting a secondary component to the [N II]λ6583 within the entire FOV. We note that an excess emission to the blue wing of [N II]λ6583 can affect the Gaussian fits to both Hα and [N II]λ6583, causing artificially high velocity and velocity dispersions for both, as seen in our pilot study with NGC 1097. This issue can consequently affect the residual velocity map of NGC 4303, which we construct by fitting a disc model to the Hα velocity field. Comparisons between measurements obtained from single Gaussian fits and fits including the secondary component, did not show a significant velocity shift or velocity dispersion change for Hα, indicating that the residual velocity map is not affected by an excess emission. However, the introduction of the secondary component led to a [N II]λ6583 velocity shift of ∼5–10 km s^{-1} and a [N II]λ6583 velocity dispersion reduction of ∼40 per cent in the regions to the east and west of the centre, where the velocity dispersion of [N II]λ6583 was originally high, but also to south of the centre, which coincide with highly blueshifted [O III]λ5007 velocities and high [O III]λ5007 velocity dispersions. This spatial coincidence likely indicates that [N II]λ6583 is also affected by the AGN outflows. Such differences in [N II]λ6583 measurements are large enough to recognize the contribution from the AGN outflows but have a negligible effect on the velocity difference map, which incorporate [N II]λ6583 velocity field together with Hα. Therefore, to the east, west, and south of the centre, we do not apply masking and the measurements are kept with those obtained from the single Gaussian fits.

However, the most prominent [N II]λ6583 velocity shifts, ∼40–60 km s^{-1}, occur outside the nuclear ring, ∼7 arcsec north-west of the centre, where the highest [N II]λ6583 velocity dispersions are originally seen; see Fig. A12. Including the secondary component to the fitting reduced the velocity dispersions there by ∼60–70 per cent. This region is outlined by a pink box in the second panel of Fig. A12, also presented in the third panel of the same figure after certain mask conditions are applied, which is explained below in more detail. Additionally, this region has anomalously blueshifted [N II]λ6583 velocities, while Hα velocities are at similar values to the surrounding.

Because of such large changes in [N II]λ6583 velocity and velocity dispersion after introducing the secondary component to the fitting, we had a closer look at the spectra of spaxels in that region. The Hα and [N II]λ6583 wavelength region of spectra exhibited features much more complex than those seen in NGC 1097. To demonstrate this, in the first panel of Fig. A12, we present two spectra: (a) from a spaxel where the fits are unaffected by the excess emission, (b) from a spaxel where the fits to [N II] components are significantly affected from the excess emission, (c) from the same spaxel in (b), after the excess emission is fitted with the secondary component. In all three subpanels, there are two emission line components associated with components of [N II] doublet and of Hα; unlike what is seen in the spectra of NGC 1097, NGC1433, and NGC4321 where the excess emission only appears as an asymmetry to the main emission line. In the spaxel marked with an 'x' in the second panel (left) of the figure, fitting single Gaussians to each emission line recovers well the parameters of the main component. However, in the spaxel marked with an '+' in the second panel (left) of the figure, the fit to the Hα line incorporates the main component only, and the fit to [N II]λ6583 line incorporates both the main and secondary components which artificially increases the [N II]λ6583 velocity dispersion and blueshifts the [N II]λ6583 velocities for those spaxels. Since Hα is fitted well, the measurements are not affected by the second component of [N II]λ6583. Moreover, since [N II]λ6548 and [N II]λ6583 fits are kinematically bound, the wrongly fitted single Gaussian to [N II]λ6583 also affects Gaussian fits to [N II]λ6548. As shown in subpanel (c), including the secondary component effectively separates the two [N II]λ6583 components, correcting the Gaussian fits. Consequently, the [N II]λ6583 velocity dispersions are reduced and the blueshifted velocities are brought back to values similar to the surrounding, as shown in the region outlined with a pink box in the second panel (right) of Fig. A12.

Since such large [N II]λ6583 velocity shifts, with ∼40–60 km s^{-1}, would affect the velocity difference map significantly, we proceed to mask the artificial measurements in the affected region, and then use the measurements of the main line component of fits including the secondary component. The spaxels that are most affected by the excess emission are presented in the third panel of Fig. A12. To correct the measurements in these spaxels, we have followed the masking concept explained in Section 3.2.1; ensuring there is a significant velocity shift and velocity dispersion change for [N II]λ6583 between measurements from the two fitting approaches. Since Hα is not affected by the secondary component, we do not include any conditions regarding Hα measurements, unlike in the case with NGC 1097 presented in Paper IV. The conditions applied to construct the mask are as follows:

(i) $V_{[N\,II]} - V_{[N\,II],corr} \leq -10$ km s^{-1}.
(ii) $\sigma_{[N\,II]}/\sigma_{[N\,II],corr} \geq 1.5$.
(iii) $\sigma_{[N\,II]w} \leq 300$ km s^{-1}.
(iv) $3'' \leq \Delta\alpha \leq 6''$ and $3.5'' \leq \Delta\delta \leq 6.5''$.

where *corr* indicates the values extracted from the fits including the secondary component. The third condition, the velocity dispersion limit of the secondary [N II]λ6583 component ([N II]w), ensures that the secondary component is real and is not fitted to noise. The spatial cuts are applied to select the region where the change in velocity and velocity dispersion ratio is consistently large. For further analysis, the flux, velocity, and velocity dispersion values for all emission line groups within the mask region are replaced with those from the corresponding main components in fits that include the secondary component. Although Hα and [O III]λ5007 measurements are not affected, we continue to use measurements from fits with a secondary component to maintain consistency. The resultant flux, velocity, and velocity dispersion maps of all emission line groups are presented in Fig. 2.

The PA of LON returned from KINEMETRY varies from 110°, within the outer regions, to 140°within regions inside the nuclear ring. Since the flow is more circular inside the nuclear ring, we explored around 140°, and converged using 135°as the PA of the LON since this value minimized the artefacts seen in the residual velocity map; 135°also agrees with values obtained from large-scale fits within a couple of degrees (L. Chemin et al. 2006; PA of LON = 132°). i inferred from KINEMETRY converged around 42°, which differs by 18°from the inclination obtained from large-scale fits (L. Chemin et al. 2006; $i = 23.5°$). Upon several checks, the residual velocity map resultant from subtracting a disc with $i = 23.5°$, reveals weak $m = 3$ harmonic terms, while such artefacts are less emphasized when the disc model is constructed with $i = 42°$. Thus for further analysis, we settle on using the i and PA of the LON inferred from KINEMETRY. As shown in Fig. 2, the residual velocity map reveals a coherent structure exhibiting negative velocities, with amplitudes of ∼20 km s^{-1} to the west of the nucleus. This structure extends from the north towards

Downloaded from academic.oup.com/mnras/article/552/3/stag1204/8721813 by guest on 30 October 2026

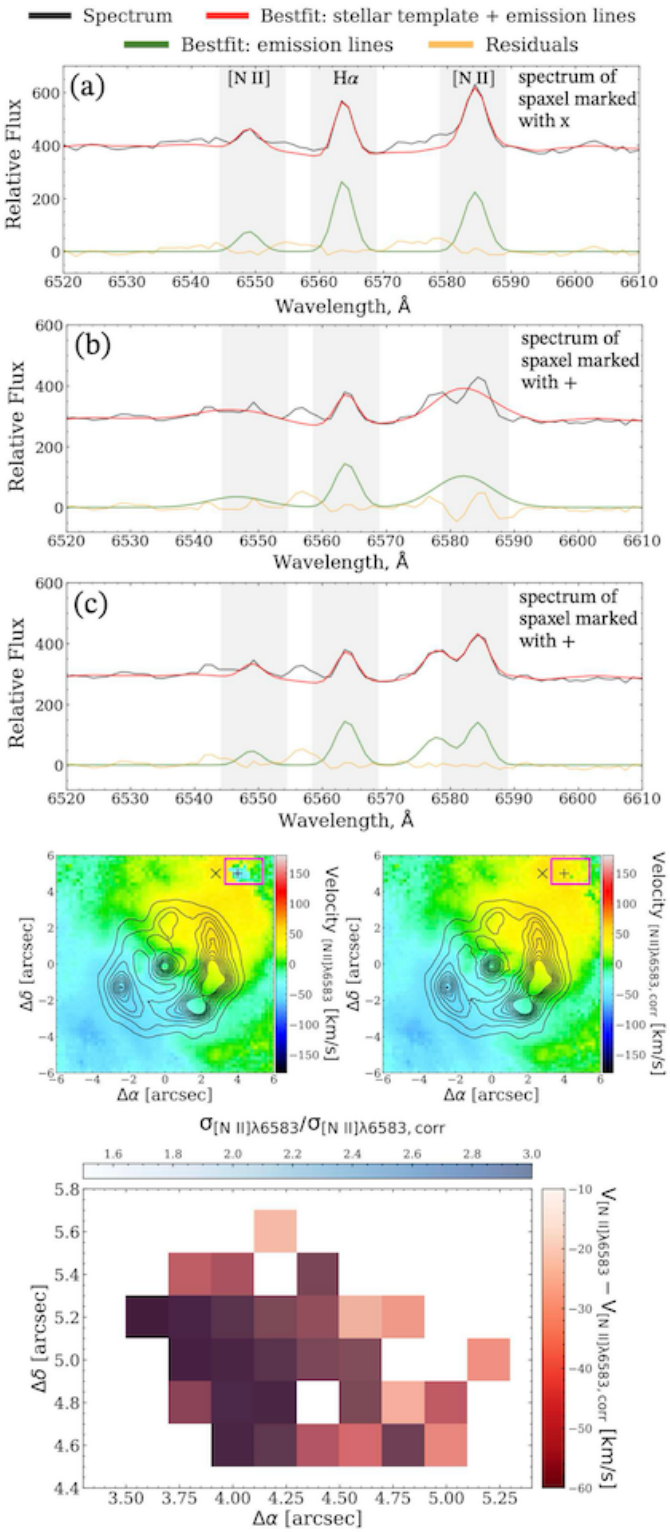

Figure A12. Spectra and masked region of NGC 4303. *First:* Spectrum of spaxels: marked with an 'x' in the second panel, excess emission does not affect the fits (a); marked with a '+' in the second panel, excess emission affects the fits (b); same spaxel as in (b), after the excess emission is fitted with a secondary component (c). The lines represent the MUSE spectrum (black), the best fit of the stellar template with emission lines (red), the best fit of the emission lines (green) and the difference between the MUSE spectrum and the combined best fit with stellar template with emission line templates (orange). *Second:* velocity map of [N II]λ6583 when emission lines are fitted with single Gaussians (left), and with the secondary component included (right). The pink box represents the region where [N II]λ6583 measurements are the most affected by the excess emission. Black contours represent the Hα emission from the nuclear ring. *Third:* region enclosed by the magenta box in the second panel, showing the mask of spaxels for which the fits including secondary component were used in further analysis. The red and blue colour maps show the velocity shift of [N II]λ6583 and the ratio of [N II]λ6583 velocity dispersion, respectively, before and after including the secondary component in the fitting.

Downloaded from academic.oup.com/mnras/article/552/3/stag1204/8721813 by guest on 30 October 2026

the south and connects to the nuclear ring at the south-west, roughly coinciding with the north-western dust lane external to the nuclear ring. The largest deprojected residual velocity amplitudes observed across this structure are roughly $\sim$50 km s^{-1}. After crossing the nuclear ring, the same coherent structure extends towards the nucleus from the west of the centre, roughly along the major axis of the inner bar. Although several extended structures exhibit enhanced positive residual velocities throughout the FOV, exhibiting deprojected residual velocity amplitudes up to $\sim$20 km s^{-1}, particularly in the nuclear ring, we do not see a clear counterpart to the structure with negative residual velocities.

Outside the nuclear ring, roughly coinciding with the coherent structures in the velocity residuals there, a coherent structure with negative velocity differences of $\sim$15–20 km s^{-1} is seen, extending inwards from the nuclear ring and approaching to the nucleus from the east of the centre. This structure is located $\sim$0.2–0.5 arcsec downstream of a dust lane, which appears to be related to the inner bar; thus this kinematic structure can be indicative of an inflow along the inner bar. Moreover, two regions $\sim$1–2 arcsec north-west and south-east from the centre, show elevated velocity differences of amplitudes $\sim$15 km s^{-1}, one with negative and one with positive velocities, supporting the argument of potential inflow seen along the inner bar.

The BPT map of the galaxy shows predominant SF in the nuclear ring and outside of it where clumpy Hα emission is seen. In the remaining regions, the ionization is dominated by composite and LINER emission. Inwards from the nuclear ring, the emission is of LINER kind, agreeing with the classification from former works (e.g. L. C. Ho et al. 1997).

Both the residual velocity and velocity-difference maps reveal consistent signatures of extended shocks along the outer and inner bars of NGC 4303. These coherent structures extend over several kiloparsecs and exhibit large deprojected residual velocity magnitudes of up to $\sim$50 km s^{-1}, which can be seen as the outlined features in Fig. 3. Their coherent morphology, large spatial extent, and high residual velocities therefore support their association with extended shocks. This consistency across different methodologies indicates that signatures of extended shocks can be reliably detected using complementary approaches. These findings reinforce the importance of searching for extended shocks using both model-dependent and model-independent methods.

A13 NGC 4321

NGC 4321, also known as M100, is a member of the Virgo Cluster and has been extensively studied in former works (J. H. Knapen et al. 1995a, b, 2000; S. D. Ryder, J. H. Knapen and M. Takamiya 2001; E. L. Allard, R. F. Peletier and J. H. Knapen 2005; S. García-Burillo et al. 2005; S. Haan et al. 2008; M. Pohlen et al. 2010; L. Hermosa Muñoz et al. 2022; D. Liu et al. 2023). The images and diagnostic maps of the galaxy are presented in Fig. A13(a). As shown in the large-scale and colour images, the galaxy has a bright core and a nuclear ring within the $\sim$8–10 arcsec radius. The galaxy is double barred, hosting an inner bar within $\sim$5 arcsec radius and an outer bar within $\sim$26 arcsec radius (J. H. Knapen et al. 1995a, b; P. Erwin 2004). There are several star-forming spiral arms surrounding the outer bar. Both large-scale and MUSE FOV images, and the unsharp mask image reveal the curved dust lanes along the outer bar, joining the nuclear ring and continuing towards the nucleus.

The [N II]λ6583 flux, velocity, and velocity dispersion maps of NGC 4321 referred to in paragraph below show the measurements obtained from single Gaussian fits, presented in Appendix B, third row of Fig. B1. Hα and [O III]λ 5007 flux, velocity, and velocity dispersion measurements can be represented with the main diagnostic maps presented in Fig.A13(a). These measurements are obtained from fits including secondary component to [N II]λ6583, yet Hα and [O III]λ5007 are not affected by this correction, more details on this are provided in the following paragraphs.

As presented in Figs A13(a) and B1 (third row), the strongest Hα and [N II]λ6583 emission is in the nuclear ring and the core. Hα emission is significantly stronger than [N II]λ6583 emission. Outside the nuclear ring, clumpy Hα and [N II]λ6583 emission is seen. [O III]λ5007 emission is weak throughout the FOV, yet the most pronounced emission is confined within the core. Across all emission line groups, velocity maps reveal perturbations from circular rotation with the zero velocity line having strong indents outside the nuclear ring at $\sim$5–7 arcsec radius. There is also an indent in the zero velocity line, $\sim$3 arcsec south-east of the nucleus, evident in [N II]λ6583 and [O III]λ5007, but absent in Hα. In the nucleus, the velocity dispersion of all emission line groups is high. Moreover, in a region extending from the central $\sim$4 arcsec towards the south, which partially overlaps with the indent in the zero velocity line, the [N II]λ6583 velocity dispersions are up to $\sim$170 km s^{-1} and [O III]λ5007 velocity dispersions are up to $\sim$200 km s^{-1}; while Hα velocity dispersions are not elevated there. Throughout the nuclear ring and the curved dust lanes, the velocity dispersion of Hα and [N II]λ6583 is low, around $\sim$60–70 km s^{-1}. Outside the nuclear ring, to the west and south-east of the centre, several regions exhibit enhanced Hα and [N II]λ6583 velocity dispersions with values ranging from 90 to 120 km s^{-1}.

Examining the spectra in the regions south of the nucleus, where the highest [N II]λ6583 velocity dispersions are seen, we noticed an excess to the blue wing of [N II]λ6583, similar to that seen in NGC 1097 and NGC 1433. This indicates that the high velocity dispersion in those spaxels is artificial and caused by poorly fitted Gaussians. Thus, to account for the excess, we allowed for fitting a secondary component to [N II]λ6583, following the approach introduced in Paper IV. The secondary component fitted to the excess will allow separating the main emission coming from the disc and an excess source.

Next, to identify the regions that are the most affected by the excess emission, we compared the kinematic measurements of main emission lines obtained from single-Gaussian fits and the fits with the secondary component. The Hα and [O III]λ5007 measurements throughout the FOV are generally unaffected. However, extending from the centre $\sim$4 arcsec towards the south, we identified a localized region with large [N II]λ6583 velocity shifts, up to $\sim$45 km s^{-1}, between the two kinematic measurements explained above; this region is shown in the top-left panel of Fig. A13(b), after the masking criteria explained in further are applied.

To correct the kinematic measurements of [N II]λ6583, which are the most affected by the excess emission in spectra, we must define the region where including the secondary component alters the kinematic measurements of the [N II]λ6583 significantly. To define this region, we used the following criteria:

(i) $V_{[N\,II]} - V_{[N\,II],corr} \leq -10$ km s^{-1}.
(ii) $\sigma_{[N\,II]}/\sigma_{[N\,II],corr} \geq 1.2$.

Downloaded from academic.oup.com/mnras/article/552/3/stag1204/8721813 by guest on 30 October 2026

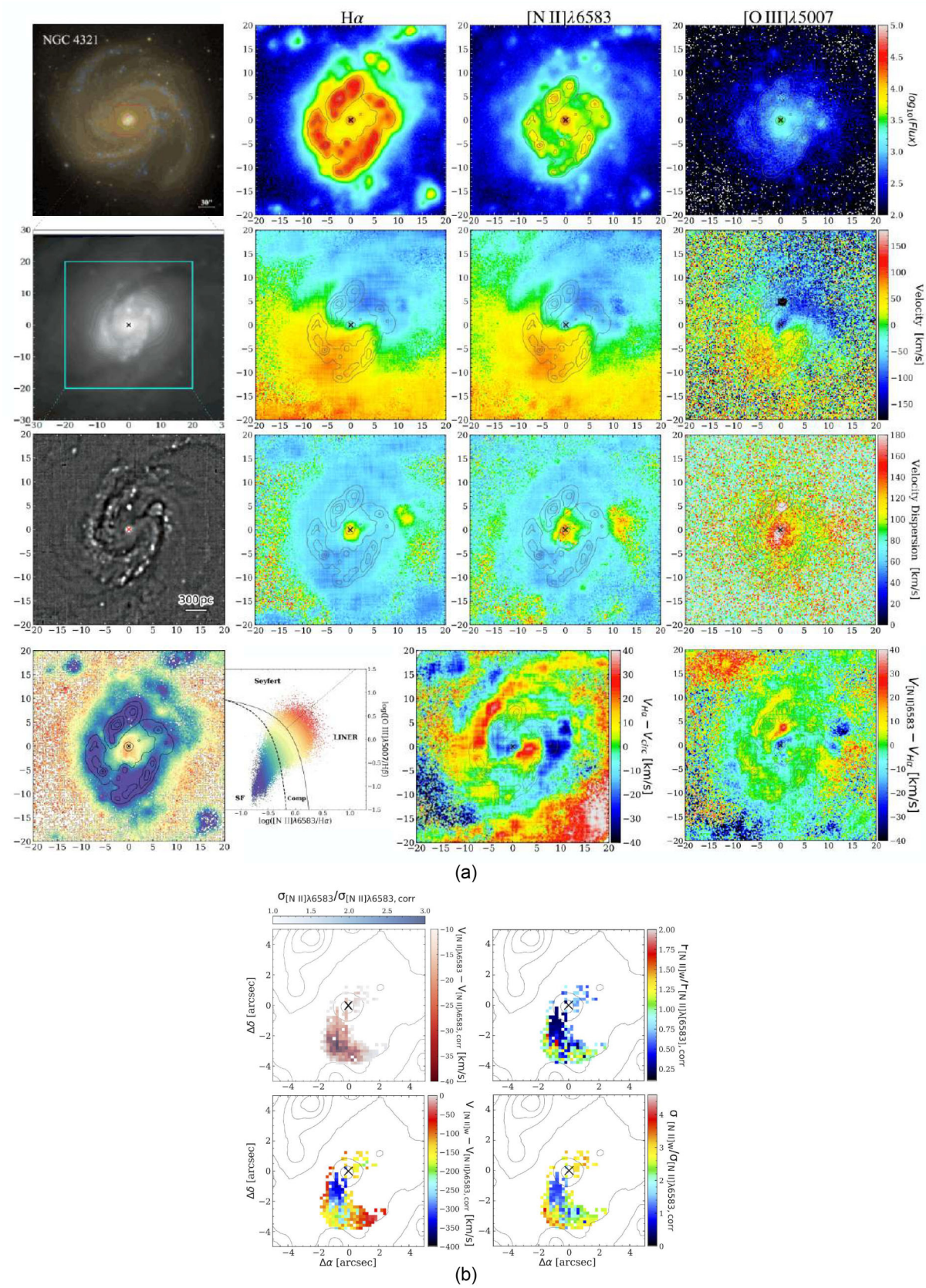

Figure A13. (a) Images and diagnostics maps of NGC 4321. Panels show the same as in Fig. 2. (b) Mask of spaxels for which the fits including secondary component were used in further analysis of NGC4321 (top left). The red and blue colour maps show the velocity shift of [N II]λ 6583 and the ratio of [N II]λ 6583 velocity dispersion, respectively, before and after including the secondary component in the fitting. Comparison of the secondary and main component: their flux ratio (top right) velocity difference (bottom left) and velocity dispersion ratio (bottom right).

Downloaded from academic.oup.com/mnras/article/552/3/stag1204/8721813 by guest on 30 October 2026

(iii) $\sigma_{[\mathrm{N\,II]w}} \leq 300$ km s^{-1}.
(iv) $-2.5'' \leq \Delta\alpha \leq 2.5''$and $-4'' \leq \Delta\delta \leq 2''$.

where *corr* indicates the values extracted from the fits including the secondary component. The third condition, the velocity dispersion limit of the secondary [N II]λ6583 component ([N II]w) ensures that the secondary component is real and is not fitted to noise. The spatial cuts limit, defined in criterion iv., is applied to select the region where the change in velocity and velocity dispersion ratio is consistently large. The above criteria ensure that within the region, where the derived flux, velocity and velocity dispersion measurements are significantly affected by the presence of the excess [N II]λ6583 emission, those measurements are replaced by the ones from the fit that include the secondary component. Although, for NGC 4321 only [N II]λ6583 measurements are affected by the excess emission, we also replaced the Hα and [O III]λ5007 measurements obtained from single Gaussian fits with those obtained from the fits with the secondary component, to maintain consistency across different line groups. After these corrections, Hα and [N II]λ6583 velocities and velocity dispersion are in much better agreement than before the correction. The velocity dispersion of [N II]λ6583 within the masked region is reduced by roughly ∼ 30 per cent. The resultant flux, velocity, and velocity dispersion maps of all emission line groups are presented in the Fig. A13(a); [O III]λ5007 and Hα maps are not affected.

As shown in the bottom panels of Fig. A13b, the secondary component appears blueshifted by ∼300 km s^{-1} with respect to the main component, and the blueshift decreases away from the galaxy centre. The velocity dispersion of the secondary component is larger than that of the main component by up to 20 per cent, and this ratio increases away from the nucleus. The coherent morphology of the region where excess is dominating, and extreme kinematics of the secondary component within this region suggest the presence of AGN outflows.

The disc orientation parameters inferred from KINEMETRY, PA of the LON = 155° and $i = 36°$, are within only a couple of degrees from parameters estimated from large-scale fits (e.g. S. Haan et al. 2008; PA of the LON = 152°, $i = 32°$). The residual velocity map of galaxy exposes two strong coherent structures, one with positive and one with negative velocities, with amplitudes of ∼25–30 km s^{-1}. The structure with positive velocities extends from the north-west and joins the nuclear ring from the east, and the structure with negative velocities extends from the south-east and joins the nuclear ring from the south-west. After joining the nuclear ring both structures continue extending along the nuclear ring. These coherent structures are downstream from the dust lanes by ∼0.5–1 arcsec and are consistent with being their counterparts. The largest deprojected residual velocity amplitudes across these structures are around 55 km s^{-1}. Outside the nuclear ring, to the north-west, a part of the coherent structure with negative velocities continues extending straight, towards the north rather than following the ring; this region coincides with the region with enhanced [N II]λ6583 and Hα velocity dispersion, likely indicating the overshooting of the post-shock gas there. Inwards from the nuclear ring, two regions with enhanced residual velocities with amplitudes of ∼20–30 km s^{-1} are seen; one exhibiting negative and one positive velocities. These regions can be a continuation of the structures extending along the nuclear ring and likely indicate the continuity of inflow to the innermost region.

The velocity difference map of the galaxy exposes several distinct structures. Inwards from the nuclear ring, there are regions with positive and negative velocity differences of amplitudes ∼20–30 km s^{-1}, but these regions are rather amorphous and show no point symmetry around the nucleus. Outside the nuclear ring, there is a coherent structure exhibiting positive velocity differences, with amplitudes of ∼10 km s^{-1} which roughly coincides with the coherent structure with positive velocities in the residual velocity map. Within the region associated with overshot gas, and west of it, the velocity differences are elevated, exhibiting amplitudes of ∼15 km s^{-1} or more; this observation supports the presence of complex dynamics there.

Furthermore, the BPT map shows the emission of LINER type in the nucleus. The nuclear ring and the regions with clumpy Hα and [N II]λ6583 emission are predominantly star-forming. Within the remaining regions outside the nuclear ring, there is predominant LINER emission.

NGC 4321 reveals strong coherent continuous structures in the residual velocity map, extending over several kiloparsecs (see also features outlined in Fig. 3) and exhibiting large deprojected residual velocity amplitudes up to ∼55 km s^{-1}, which are consistent with the concept of extended shocks in gas.

A14 NGC 4380

The diagnostic images and maps of NGC 4380 are presented in Fig. A14. As the large scale and colour image show, NGC 4380 is an unbarred galaxy with a bright core encircled by flocculent SF and dusty spiral arms. The MUSE FOV encompasses the core and a portion of the dusty spirals around it. As presented in the unsharp mask image, the prominent spiralling dust features around the core are revealed.

As shown in the flux maps, emission across all line groups is weak, particularly [O III]λ5007. Hα and [N II]λ6583 emission is clumpy. The velocity fields of Hα and [N II]λ6583 are mostly unperturbed. The zero velocity line remains straight. The velocity dispersion of Hα and [N II]λ6583 remains low, around ∼50–60 km s^{-1} throughout the entire FOV.

The PA of the LON = 161°and $i = 59°$estimated by fitting the velocity field with KINEMETRY agrees well with the parameters obtained from large-scale photometry (PA of the LON=157°and i=59°). The residual velocity map of the galaxy exposes faint and noisy m=1 harmonic terms; after finely adjusting the PA of the LON in 1°increments, we settled on using 159°since this value raises the weakest artefacts. This demonstrates that once the velocity field is undisturbed, KINEMETRY can estimate the disc orientation parameters consistent, within couple of degrees, with those obtained from large-scale photometric fits. The deprojected residual velocity amplitudes throughout the faint structures seen in the map are small, 20 km s^{-1} or below, indicating an absence of a shock nature. Similarly, the velocity difference map is overall noisy and exposes no prominent structures.

The BPT map of the galaxy shows prominent SF interspersed with LINER emission spots in the spiral arms, where clumpy Hα and [N II]λ6583 emission is seen. Moreover, within ∼3–4 arcsec radius, ionization is dominated by LINER emission. While the central LINER emission can be associated with contribution from the core, the LINER emission along the spiral arms can be attributed to hot old low-mass stars or potentially to supernovae.

NGC4380 has relatively unperturbed kinematic fields and does not present signatures of extended shocks. This quiescence possibly can be attributed to the unbarred morphology of the galaxy, similar to our findings for NGC 4237.

Downloaded from academic.oup.com/mnras/article/552/3/stag1204/8721813 by guest on 30 October 2026

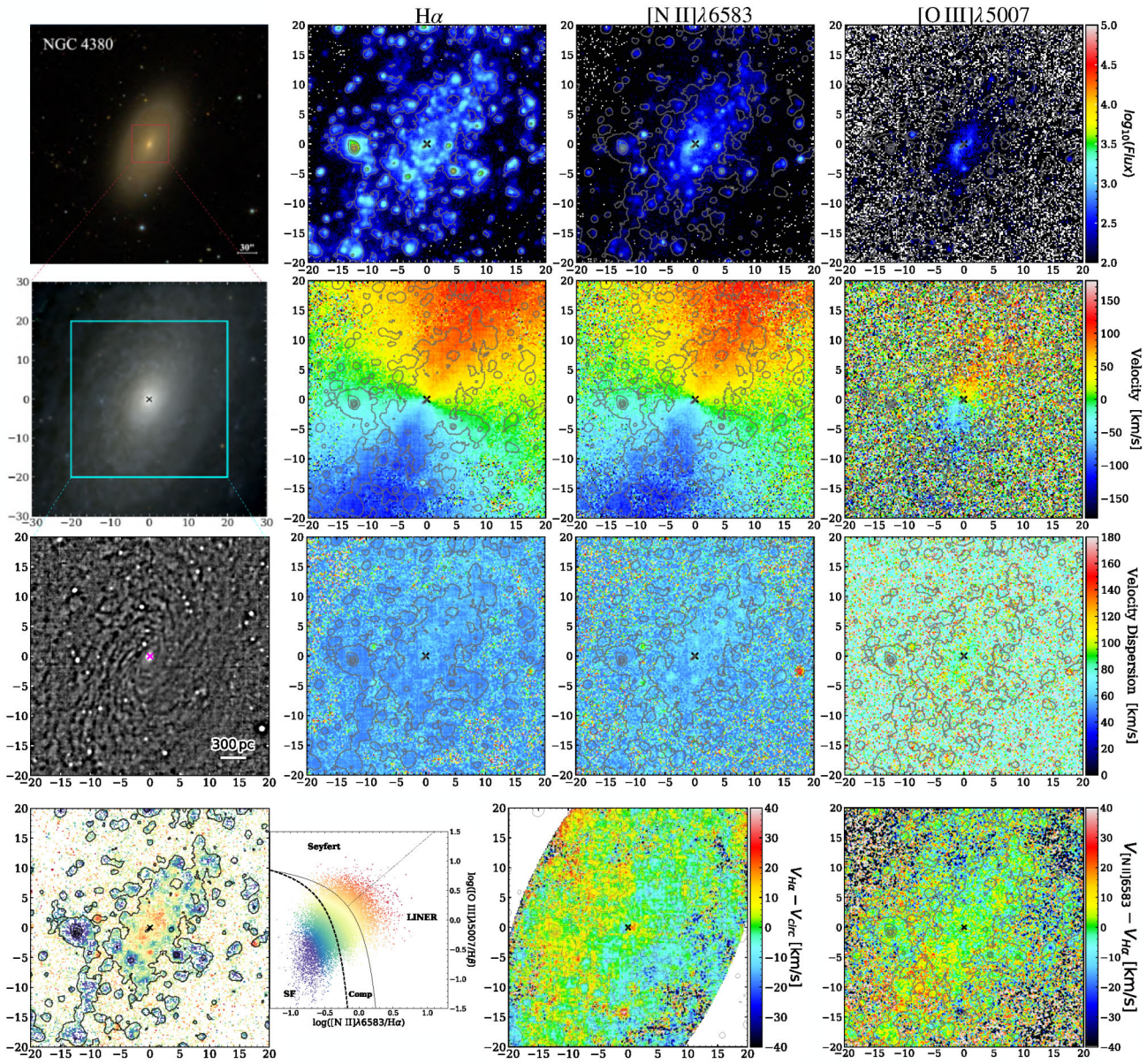

Figure A14. Images and diagnostics maps of NGC 4380. Panels show the same as in Fig. 2.

A15 NGC 4457

NGC 4457 has been well-studied in many former works (B. Vollmer et al. 2013; R. S. Nemmen, T. Storchi-Bergmann and M. Eracleous 2014; J. R. Cortés, J. D. P. Kenney and E. Hardy 2015; M. Querejeta et al. 2021; S. K. Stuber et al. 2021; L. Hermosa Muñoz et al. 2022; H.-A. Pan et al. 2022; I. D. Roberts et al. 2023). The images and diagnostic maps of the galaxy are presented in Fig. A15. As shown in the large-scale and colour images, the galaxy has a bright core, which is classified as LINER type (Y. Terashima et al. 2000; L. Hermosa Muñoz et al. 2022), and a bar of ∼2–3 arcsec radius. Moreover, based on its brightness profile, NGC 4457 is classified as having a lensed morphology (M. Querejeta et al. 2021); the lens is visible within the ∼30 arcsec radius. The MUSE FOV covers almost the entire lens, the bar, and the core. In colour images, two dust lanes are seen, resembling standard dust lanes along bars but instead in an oval with major axis ∼80°, measured from North to the East. A string of young stars is seen downstream the dust lanes. The formation of these stars is likely triggered by the increased gas density downstream of the extended shocks, unlike in standard bar lanes where strong shear usually inhibits SF. In the unsharp mask image, the dust lane that extends from the southwest end of the frame that curves inwards at east-south-east is more pronounced than its counterpart. The most prominent region of the counterpart dust lane is seen extending north to south within the inner 5 arcsec radii.

As shown in the flux maps, the emission for all line groups is concentrated within the ∼3–4 arcsec radius. A string of Hα and [N II]λ6583 emission is seen along the dust lane to the southwest. Several Hα and [N II]λ6583 clumps, aligned with the north to south direction at ∼5 arcsec radius, are present downstream from the counterpart dust lane. Examining the velocity maps of

Downloaded from academic.oup.com/mnras/article/552/3/stag1204/8721813 by guest on 30 October 2026

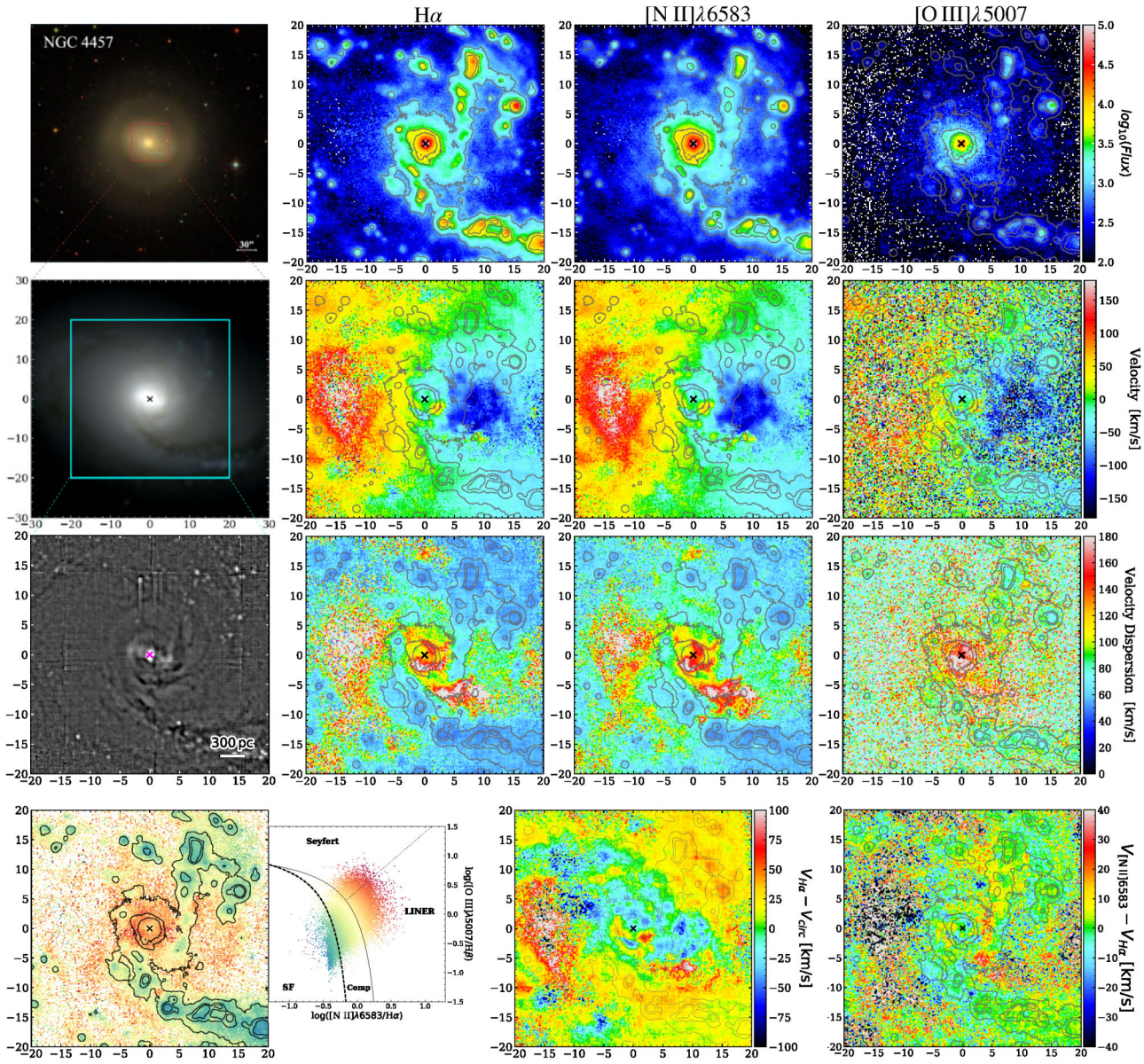

Figure A15. Images and diagnostics maps of NGC 4457. Panels show the same as in Fig. 2.

Hα and [N II]λ6583, we notice disturbances and velocities inconsistent with the rotating disc. Within ∼4 arcsec radius, the zero-velocity line has strong indents, and positive velocities are present to the south-west of the centre where negative velocities would be expected for a rotating disc. A string of regions with Hα and [N II]λ6583 velocities positive or close to zero extends into the region where velocities are expected to be blueshifted, at $\Delta\delta \sim -7$, starting at $\Delta\alpha \sim 0$ arcsec and stretching up to $\Delta\alpha \sim$ 10 arcsec.

The velocity dispersion of Hα and [N II]λ6583 is high in the core and around it; within ∼4 arcsec radius values exceed 150 km s^{-1}. Similarly, high velocity dispersion is recorded to the east from the centre, up to a 15 arcsec distance. Additionally, in a region extending from ∼6 to ∼15 arcsec of the centre, the velocity dispersion values are as high as the values seen in the core. This region roughly coincides with the above-mentioned string of regions with anomalous positive velocities. In regions with clumpy Hα and [N II]λ6583, the velocity dispersion of Hα and [N II]λ6583 remain around ∼60 km s^{-1}. The velocity and velocity dispersion maps of [O III]λ5007 are rather noisy due to poor signal, yet the values suggest the same trends as the values seen in Hα and [N II]λ6583 velocity and velocity dispersion maps.

The PA of the LON = 80°and $i = 20°$ estimated using KINEMETRY agree well with the parameters obtained from large-scale fits within CBS (see Table 2). Consequently, we adopt these parameters for the final disc model of the galaxy. The residual velocity map of the galaxy reveals several regions within ∼4 arcsec radius with velocity residuals of amplitudes ∼30–50 km s^{-1}. Four of these regions exhibit negative velocities. Three of them are towards the north-east to north-west and one towards the

Downloaded from academic.oup.com/mnras/article/552/3/stag1204/8721813 by guest on 30 October 2026

south. The other two regions exhibit positive velocities, one to the east and one to the west. There are no signs of wrongly fitted i or the PA of the LON in the residual velocity map, indicating that the structures seen in the residual velocity map, particularly within ∼4 arcsec, are not due to the modelling of the disc and are likely caused by the AGN outflow cone piercing the disc and raising complex signatures in the kinematics (T. C. Fischer et al. 2013).

In the region to the south-west, where elevated velocity dispersions and anomalous velocities are seen, the velocity residuals exhibit coherent positive values with amplitudes exceeding 50 km s^{-1}. Moreover, high positive residual velocities are partially coinciding with the emission lane to the south-west. This structure potentially continues towards the east of the frame where values reach above 50 km s^{-1}. In the same region to the east, the velocity dispersion of both Hα and [N II]λ6583 is high. Although several coherent structures can still be noticed, which can be associated with the inflow in the bar, the residual velocities throughout the emission lane are noisy and patchy. The corresponding deprojected residual velocity amplitudes across the extent of these structures are up to 120–125 km s^{-1}. Due to complex mechanisms within the innermost regions of the galaxy, none of the structures that is relatively extended can be traced to the nucleus.

The velocity difference map of the galaxy is rather noisy. Inside the north to south running dust lane, at ∼4–5 arcsec, velocity differences are increased with amplitudes around 15 km s^{-1}.

Moreover, the BPT map exhibits LINER-type emission within the ∼4 arcsec radius. This supports the idea that the AGN might be contributing to disturbances of gas in the core region. In regions of strong Hα emission, there is composite emission with a contribution from SF.

Despite potential signatures of extended shocks within the bar region, the presence of strong local SF and AGN activity within the innermost regions of the galaxy prevents us from tracing these signatures to the innermost regions. Therefore, we do not classify this galaxy as showing signs of coherent extended shocks, and it is grouped under *other perturbations* category.

A16 NGC 4643

NGC 4643 is one of the galaxies for which CBS provides a detailed morphological, photometric, and stellar kinematic study (P. Erwin et al. 2021). We present the images and diagnostic maps of the galaxy in Fig. A16. As shown in the large scale image, NGC 4643 has a bright core and a strong bar surrounded by a ring. The MUSE FOV covers the core and almost the entire bar region. The unsharp mask image of the galaxy highlights a faint nuclear ring with ∼3–4 arcsec radius. However, this ring appearance is a side effect of Galaxy's nuclear disc having a broken-exponential radial profile; more details can be found in P. Erwin et al. (2021). Therefore, we refer to this structure as a nuclear disc instead of nuclear ring.

As shown in the flux maps, compared to other galaxies we studied in this work, NGC 4643 has the weakest emission across all line groups. The strongest emission is confined within ∼4–5 arcsec radius, and there is no sign of the nuclear ring in emission. Weak emission lanes are seen extending from the western side of the nuclear disc to the south, and a weak one from the eastern side to the north. These may be the inner parts of the bar lanes curving onto the nuclear disc. As can be seen in the velocity maps of all line groups, the zero-velocity line has a wiggly shape; within the central ∼1–2 arcsec there is an intrusion of positive velocities to the south and negative to the north. Further to the north, intrusions of negative–positive velocities repeat interchangeably forming indents in the zero-velocity line.

The Hα and [N II]λ6583 velocity dispersion maps reveal high velocity dispersion values in the core, with values reaching ∼100 km s^{-1}. Within the nuclear disc, and along the bar lanes, the values decrease and remain around 70–60 km s^{-1}. The velocity and velocity dispersion of [O III]λ5007 are not reliably estimated due to poor signal, the maps are rather noisy but still show a similar trend to Hα and [N II]λ6583 fields.

The PA of the LON = 58°and i = 43°estimated by using KINEMETRY differs by 5°from the parameters estimated from large-scale photometric fits in P. Erwin et al. (2008) (PA of the LON = 53°and i = 38°). This difference can be attributed to the kinematics within central regions being dominated by the strong bar, which can influence the parameter estimations in that region. Once we model the rotating disc with parameters adopted from large-scale fits, the resultant residual velocity map is dominated by the m= 1 harmonic terms, which are the artefacts of wrongly fitted PA of the LON. The artefacts are minimized when incorporating the parameters obtained from KINEMETRY, yet subtracting the disc with parameters taken from large scale photometric fits does not affect the residual maps significantly. Therefore, we chose to adopt both parameters from the KINEMETRY, while constructing the final disc model.

The residual velocity map of the galaxy exposes two strong coherent continuous structures. One exhibits positive velocity residuals, while the other exhibits negative velocity residuals, both with amplitudes of approximately 40–50 km s^{-1}. The structure with negative velocities extends from the south edge of the frame, completing almost a full turn around the nuclear disc as it is winding inwards to connect the disc. This structure exhibits deprojected residual velocity amplitudes up to 110 km s^{-1}. The counterpart to this structure is seen in positive velocities, exhibiting deprojected residual velocity amplitudes up to 70 km s^{-1}. These two structures provide strong evidence of extended shocks in gas. Additionally, ∼0.5–1 arcsec to the north and south-east of the centre, two regions with enhanced residual velocities are seen. These regions exhibit similar amplitudes to those found around the nuclear disc. One of these structures exhibits negative velocities, while the other exhibits positive velocities, suggesting a likely inflow to the core.

The velocity difference map of the galaxy is noisy and does not exhibit any strong structures. The BPT map is dominated by LINER emission.

NGC 4643 exhibits weak emission across all line groups and has relatively less disturbed velocity and velocity dispersion fields compared to other sample galaxies we studied in this work. Nevertheless, as explained in paragraphs above and stated in Table 3, we identify coherent kinematic features extending over several kiloparsecs and exhibiting large deprojected residual velocity amplitudes of up to ∼70–110 km s^{-1}. Their coherent morphology, large spatial extent, and high residual velocities support their association with extended shocks.

A17 NGC 4941

The images and diagnostic maps of NGC 4941 are shown in Fig. A17. NGC 4941 has a bright, dust-obscured (A. Jana, S. Naik and N. Kumari 2022) Seyfert 2 type (M. P. Véron-Cetty and P. Véron 2006; D. Asmus et al. 2012) core, and an inner bar (D. Greusard et al. 2000) within ∼5–6 arcsec radius. This bar can

Downloaded from academic.oup.com/mnras/article/552/3/stag1204/8721813 by guest on 30 October 2026

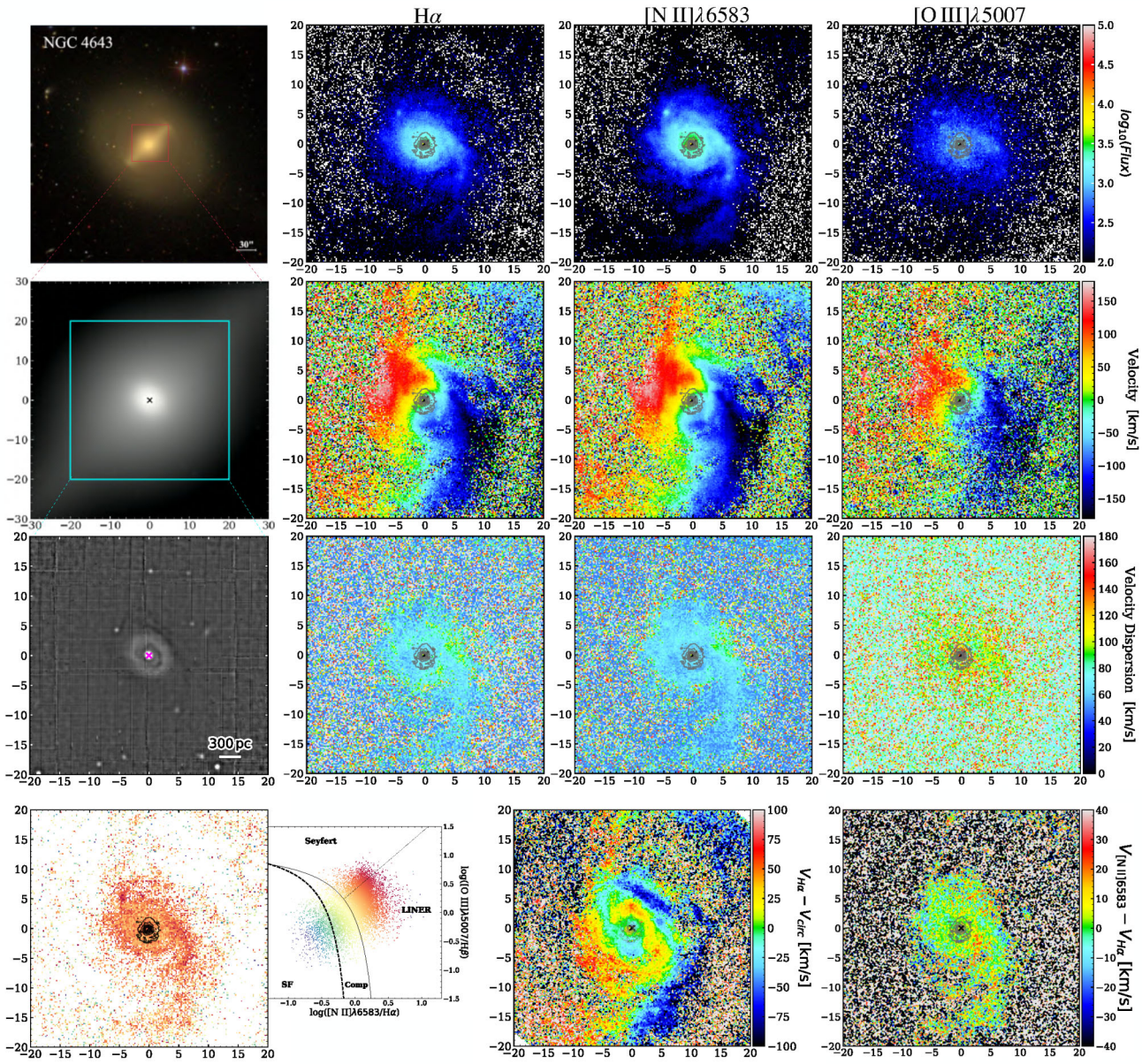

Figure A16. Images and diagnostics maps of NGC 4643. Panels show the same as in Fig. 2.

be more clearly seen in our unsharp mask image of the galaxy. Additionally, the existence of a weak boxy outer bar with a radius of ∼20 arcsec, which is surrounded by a dusty star-forming ring, is also proposed in this galaxy, both from visual and kinematic studies (P. B. Eskridge et al. 2002; P. Erwin 2004; S. K. Stuber et al. 2023). The existence of the outer bar remains a subject of an ongoing debate (G. Vaucouleurs et al. 1991; D. Greusard et al. 2000). As shown in the large scale and colour image of the galaxy, the MUSE FOV covers the core, the inner bar, and a portion of the proposed outer bar. In the unsharp mask image, several dust lanes are seen along the proposed outer bar. One such dust lane, extending inwards from the north-east, appears broken into segments and connects to the inner bar at the south-east, and another, as a much fainter counterpart to the former, connects to the inner bar at the north-west.

As shown in the flux maps, the strongest emission across all line groups is confined within the ∼2 arcsec radius for Hα and [N II]λ6583, and ∼3–4 arcsec radius for [O III]λ5007, but it is not extended along the inner bar. Beyond this region, two weak emission lanes are seen extending towards the north-east and south-west, stronger in the north-east. Both lanes appear to fork into two components ∼8–10 arcsec from the centre. In the north-east lane, [N II]λ6583 flux dominates over Hα, and in the south-west lane the opposite is true. These emission lanes mostly align with the dust lanes along the proposed outer bar.

The velocity maps reveal pronounced signs of strong non-circular motions for all emission line groups. Approximately 3 arcsec to the north-east of the centre, there is a region with kinematics inconsistent with a rotating disc. Notably, the zero velocity line exhibits prominent indents at a radius of ∼8–10 arcsec. The

Downloaded from academic.oup.com/mnras/article/552/3/stag1204/8721813 by guest on 30 October 2026

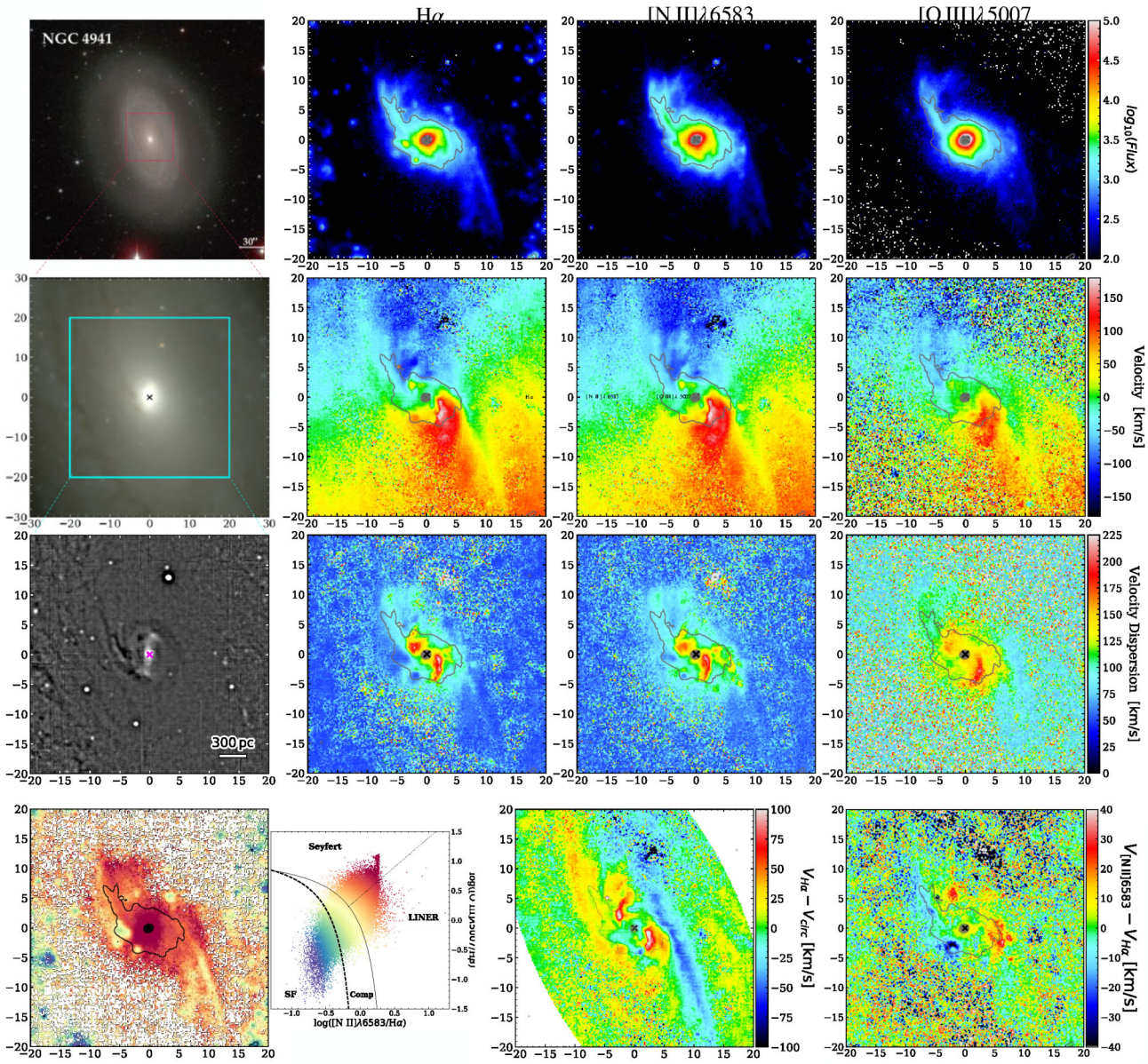

Figure A17. Images and diagnostics maps of NGC 4941. Panels show the same as in Fig. 2.

velocity dispersion maps of all emission line groups, reveal very peculiar structures. In two regions ∼4–5 arcsec towards north-east and south-west from the centre the velocity dispersion values exceed 170 km s^{-1} particularly in Hα. These structures have a bi-symmetric nature, indicative of strong outflows from the AGN, which is in line with the north structure having kinematics inconsisitent with a rotating disc. Along the emission lane to the north-east, both Hα and [N II]λ6583 velocity dispersions are notably high, reaching values around 100 km s^{-1}. On the other hand, in the outer regions of the south-west lane, the velocity dispersion drops to ∼50 km s^{-1}, while in its inner region [N II]λ6583 velocity dispersions are around 130 km s^{-1}. While [O III]λ5007 velocity dispersions exhibit some noise, a clear trend mirrors what is seen in Hα and [N II]λ6583 velocity dispersion. In the remaining regions, the velocity dispersion remains around ∼50–70 km s^{-1}.

While the PA of the LON = 25°and i = 60°estimated from KINEMETRY, slightly differs from parameters estimated from large-scale fits (e.g. L. Gutiérrez et al. 2011: PA of the LON = 21°, i = 48°), the differences can be attributed to the outer bar affecting the kinematic fits within the innermost regions. Since, we do not notice signs of artefacts from incorrectly fitted geometry in the residual velocity map, we use the parameters derived from KINEMETRY fits. As seen in the residual velocity map, two strong coherent continuous structures with amplitudes of ∼40 km s^{-1} are seen within the proposed outer bar region highlighted with the dashed lines in Fig. 3. One of these structures has positive velocities, and extends from the north edge of the frame to the south, east of the centre, while the other with negative values extends from the south edge of the frame to the north, west from the centre. These two structures manifest as straight lines parallel

Downloaded from academic.oup.com/mnras/article/552/3/stag1204/8721813 by guest on 30 October 2026

to the LON and follow the dust lanes, exhibiting deprojected velocity amplitudes up to 40 to 60 km s^{-1}. Therefore, we attribute these structures to straight shocks, indicative of inflow along the bar, providing compelling evidence supporting the existence of the outer bar. At ∼2–5 arcsec from the centre towards the north-east and south-west, there are two regions with high positive velocity residuals, with amplitudes exceeding ∼50 km s^{-1}. These structures coincide with the enhanced velocity dispersion seen across all emission line groups and further indicate its association with the AGN outflows. Although the two lane structures appear to wind towards inner regions, the structures associated with the AGN prevent us from tracing them further in.

The velocity difference map is noisy but there are regions of coherent velocity differences of magnitude ∼10–20 km s^{-1}, in alignment with the straight shocks observed along the bar in the residual velocity map. The region to the south exhibits positive and the one to the north exhibits negative velocity differences, providing further support for the disturbance of gas and the inflow along the bar. Moreover, in the regions associated with the AGN outflows, there are positive velocity differences with amplitudes around ∼15–30 km s^{-1}.

The BPT map of the galaxy reveals strong Seyfert emission within the core due to irradiation from the AGN. Beyond this central region, ionization is mostly dominated by LINER emission, except within the emission lanes, where there is also contribution from composite emission and very weak SF.

The kinematic fields of NGC 4941 reveal pronounced kinematic structures elongated along the outer bar, spanning across several kiloparsecs, with deprojected residual velocity magnitudes reaching up to ∼60 km s^{-1}. These features are associated with extended shocks along the bar but due to the strong AGN outflows, we cannot trace them to the innermost regions. Therefore, based on the grouping explained in Section 5.3, this galaxy is classified under *extended shocks and outflows* category.

A18 NGC 5248

Images and the diagnostic maps of the NGC 5248 are presented in Fig. A18. As shown in the large scale and colour image, the galaxy has a bright core surrounded by an inner nuclear ring with ∼2 arcsec radius and an outer nuclear ring with ∼7 arcsec radius. It also has a weak bar with ∼20–25 arcsec radius, surrounded by spiral arms. The MUSE FOV covers the core, the inner, and outer nuclear rings, the bar and a portion of the spiral arms. The unsharp mask image of the galaxy reveals prominent dust structures throughout the entire FOV, many extending as spirals from the outer regions towards the outer nuclear ring and then towards the innermost regions.

As shown in flux maps, the strongest Hα and [N II]λ6583 emission is confined within the inner and outer nuclear rings and there is a [N II]λ6583 emission peak in the nucleus; between the two rings the emission decreases. There is clumpy Hα and [N II]λ6583 emission outside the rings, some aligned with the dusty spirals seen in the colour image. The [O III]λ5007 emission across the entire FOV is weak but it has a peak at the nucleus. The Hα and [N II]λ6583 velocities are relatively unperturbed within the nuclear rings. However, outwards from the outer nuclear ring, the zero velocity line shows a strong indent at $\Delta\delta$ roughly 13–14 and −5 arcsec indicating streaming motion along the spiral arms.

The velocity dispersion of Hα and [N II]λ6583 is low, with values ∼60–70 within both rings. Between the two rings, the [N II]λ6583 velocity dispersion shows local peaks with values around ∼90–100 km s^{-1} in several regions to the east and south-east of the centre. Moreover, the velocity dispersion of Hα and [N II]λ6583 is around ∼60 km s^{-1} where clumpy Hα and [N II]λ6583 emission are seen outside the rings. However, outside the rings, the velocity dispersion shows an increase in two arms upstream from the spiral dust lanes, possibly indicating some shocks there.

The disc orientation parameters, the PA of the LON = 114°and $i = 44°$, obtained from KINEMETRY agree well with parameters estimated from the large-scale fits (S. Haan et al. 2008, 2009), as shown in Table 2. Thus, we employ these parameters for the final disc model. The residual velocity map of the galaxy exposes two coherent continuous spiral structures – one with positive velocities and the other with negative velocities. Both of these structures are winding from the outer edge of the FOV in clockwise direction towards the innermost regions. These two spiral structures appear as counterparts of one another and are consistent with extended shocks in gas propagating to the innermost regions. Throughout the extent of these coherent structures, the deprojected residual velocity amplitudes are around 50 to 60 km s^{-1}. These structures reach the outer nuclear ring, even though further in they are more patchy; there is an indication that the red structure is crossing and entering the inner ring, down to ∼1 arcsec.

The velocity difference map shows enhancements with amplitudes of ∼10–20 km s^{-1}. Especially inwards from the outer ring and extending to the innermost spaxel, the enhancements in velocity differences remain prominent, maintaining the characteristic positive and negative pattern. The strongest amplitudes are within the inner ∼1 arcsec. These consistent signatures provide further support for the presence of extended shocks propagating down to the innermost regions.

The BPT map of the galaxy reveals LINER emission in the core and prominent SF within both the outer and inner nuclear rings. The region between the rings, where signatures of extended shocks are seen both in velocity residual and velocity difference maps, shows a contribution from composite emission, indicating the complex interaction of a high-energy mechanism there. Outside the rings, there is composite emission with a strong contribution from SF; the SF is particularly strong where clumpy Hα emission is seen. Additionally, outside the rings, there is a contribution from LINER emission in the regions where enhanced velocity dispersions are seen.

As outlined in Fig. 3, NGC 5248 exhibits compelling signatures of extended shocks, with coherent structures extending from large radii towards the innermost regions. These structures span several kiloparsecs and show large deprojected residual velocity magnitudes of up to ∼60 km s^{-1} (see also Table 3), as identified through the different methodologies applied in this work. The extended shock signatures are particularly pronounced and show strong agreement with the expected line-of-sight velocity residual patterns presented by R. I. Davies et al. (2009).

A19 NGC 7177

NGC 7177 is a well-studied galaxy in many kinematic and photometric studies (R. S. Jong 1996; K. A. Misselt, G. C. Clayton and K. D. Gordon 1999; A. I. Díaz et al. 2000; F. Simien and P. Prugniel 2002; P. Erwin 2005; P. Erwin et al. 2008; O. K. Sil'chenko, A. V. Moiseev and A. P. Shulga 2010). The images and diagnostic maps of the galaxy are presented in Fig. A19. As shown in the large-

Downloaded from academic.oup.com/mnras/article/552/3/stag1204/8721813 by guest on 30 October 2026

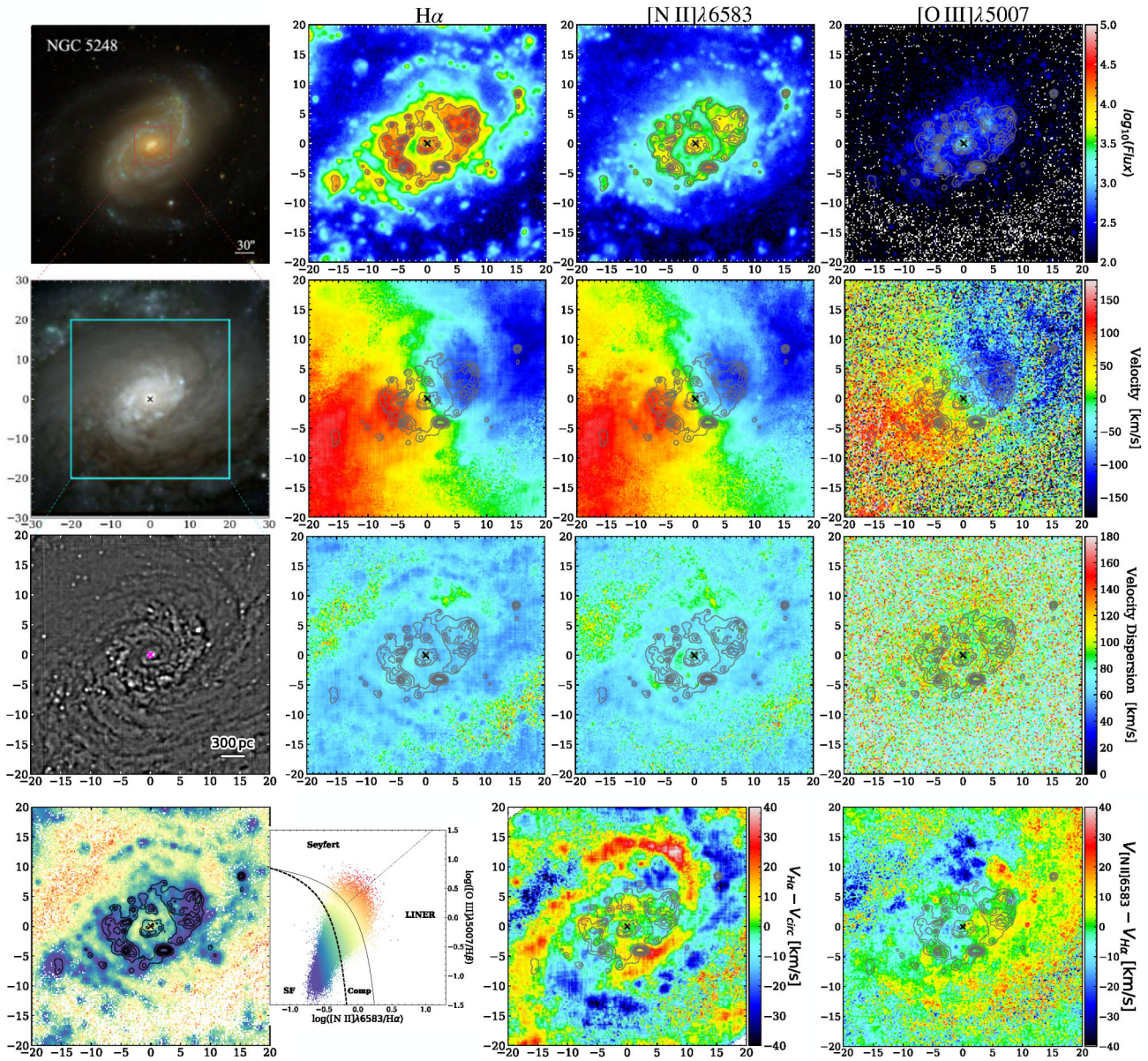

Figure A18. Images and diagnostics maps of NGC 5248. Panels show the same as in Fig. 2.

scale and the colour image, NGC 7177 has a bright dusty core, and a bar within ∼10 arcsec radius (P. Erwin 2005) surrounded by a ring. The MUSE FOV encompasses the core, the bar and the ring. The unsharp mask image of the galaxy reveals several dust lanes are seen within the bar region, more prominent in the east side of the galaxy.

As the flux maps show, the strongest emission across all line groups is confined within the inner ∼3 arcsec radius with two clumps ∼2 arcsec north and south of the nucleus, roughly along the major axis of the bar, seen in Hα emission. We also notice extended emission to the east, especially in [O III]λ5007. There is clumpy Hα and [N II]λ6583 emission indicative of local SF throughout the FOV.

Moreover, the velocity across all line groups shows non-circular motions. Within the ∼3–4 arcsec radius, the zero velocity line has a wiggly shape, with indents at the locations of the two Hα clumps. Velocity amplitude at the emission extension to the east is ∼50 km s^{-1} higher than on the other side of the nucleus. The velocity dispersion of Hα and [N II]λ6583 is high in the core and in an extended region ∼3 arcsec towards the north-east and south-west of the centre. Coinciding with this region, there appears a dust lane almost perpendicular to the bar. Upon a careful examination of the spectra of spaxels with relatively high velocity dispersions, we confirm that there is no need for a secondary component in the fitting during the kinematic extraction, and the high velocity dispersion values are intrinsic. Where clumpy Hα and [N II]λ6583 emission is seen, throughout the FOV, the velocity dispersion of Hα and [N II]λ6583 is around ∼50–60 km s^{-1}. There are velocity dispersion minima in the emission clumps ∼2 arcsec south and north of the nucleus, and another minimum ∼1–2 arcsec south of the east emission extent, spatially coincident with anomalously high LOS velocity. The velocity dispersions within

Downloaded from academic.oup.com/mnras/article/552/3/stag1204/8721813 by guest on 30 October 2026

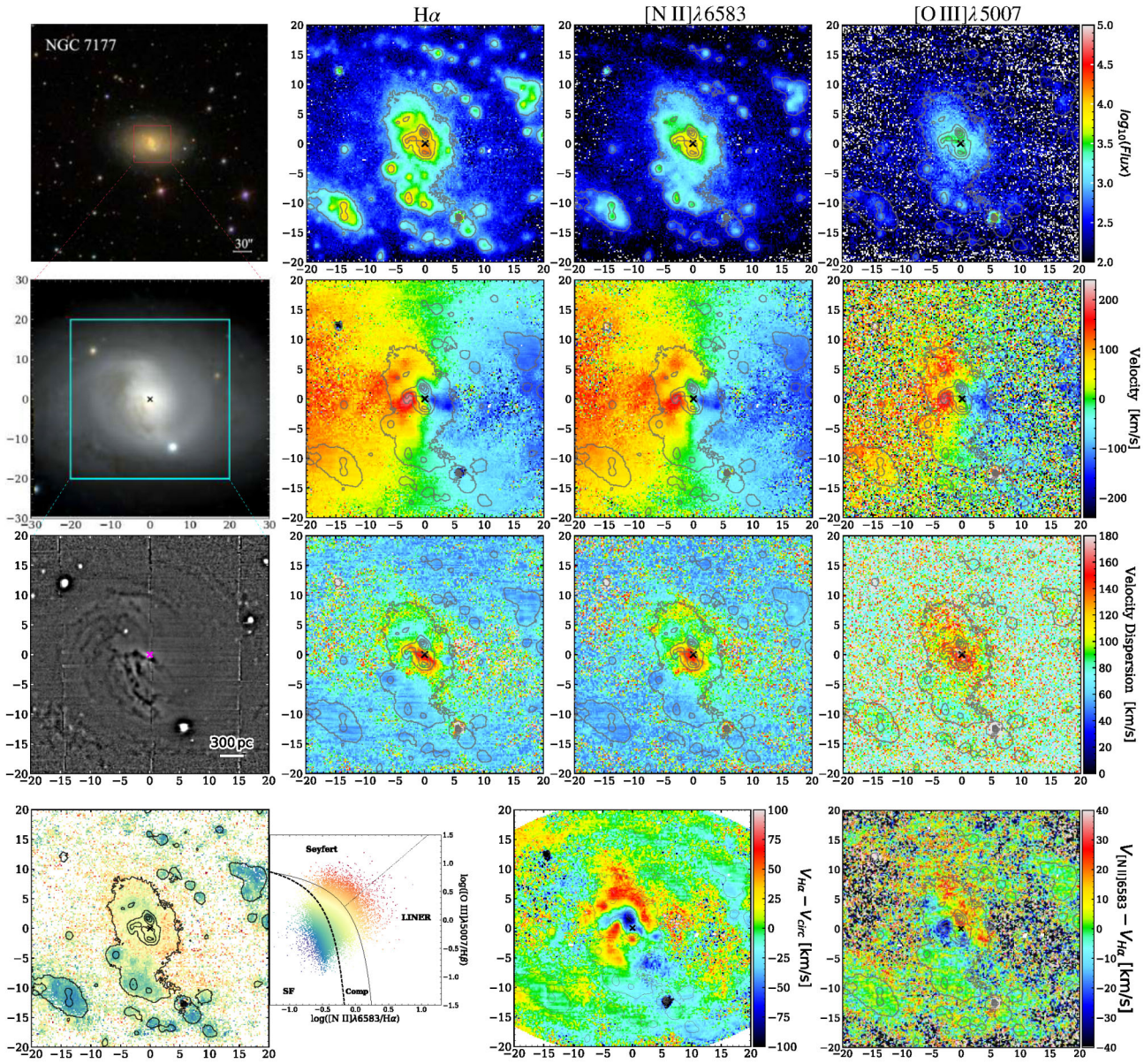

Figure A19. Images and diagnostics maps of NGC 7177. Panels show the same as in Fig. 2.

the remaining regions in the bar are relatively high with values around ∼70–120 km s^{-1}.

Fitting the velocity field with KINEMETRY, we determined the optimal disc orientation parameters as PA of the LON = 90° and i = 46°. These values deviate only slightly from the values obtained from large-scale photometric fits (e.g. P. Erwin et al. 2008; PA of the LON=83°and i =48°). However, when using the large-scale parameters in the disc model, the residual maps exhibit slight signatures of m=1 harmonic terms, while using KINEMETRY-deduced parameters minimizes those artefacts. Therefore, we settle on using parameters estimated from KINEMETRY.

The residual velocity map of the galaxy reveals several peculiar structures. Specifically, two relatively extended structures with positive residual velocities, exceeding 50 km s^{-1}, coincide with the pattern of the dust lanes. One of these structures, forms an arch to the north of the centre with further extension to the north, while the other extends almost as a straight line over ∼7 arcsec south-east of the centre. In between these two structures, a curved structure with negative velocities, of amplitudes exceeding 70 km s^{-1}, reaches the nucleus from the north. These structures appear coherent, although they do not have point symmetry. The strong positive and negative velocity residuals are separated by high velocity dispersion region, which may be indicating two streams of gas colliding, as in on-axis inflow along the bars. Thus, the low velocity dispersion regions, with local minima at ∼1–2 arcsec north and south of the nucleus, appear also to inflow towards the nucleus.

Furthermore, the velocity difference map reveals two regions with consistent velocity differences, with amplitudes around

Downloaded from academic.oup.com/mnras/article/552/3/stag1204/8721813 by guest on 30 October 2026

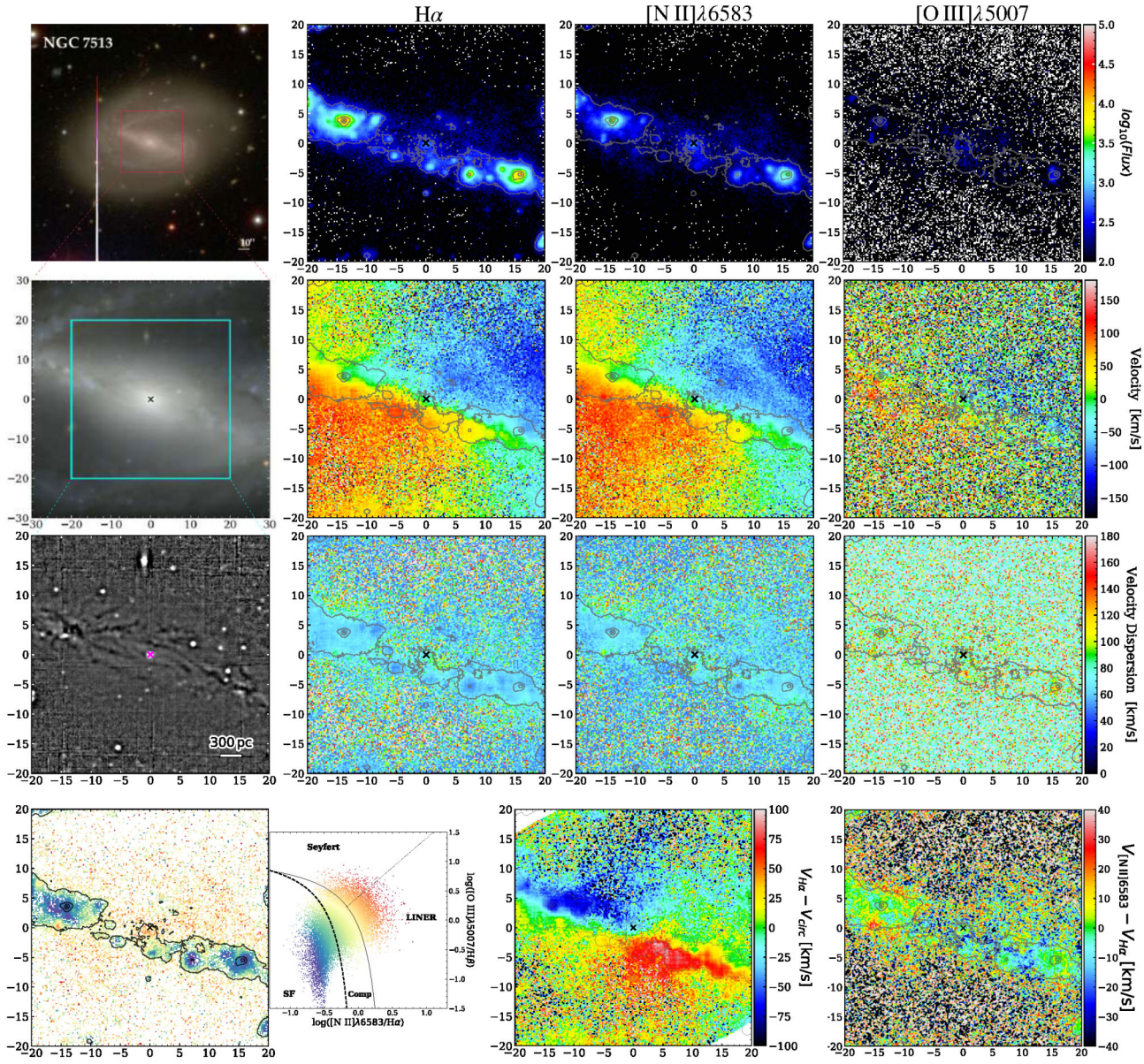

Figure A20. Images and diagnostics maps of NGC 7513. Panels show the same as in Fig. 2.

$\sim$15–30 km s^{-1}; one region with positive differences to the north-west of the centre, and the other region with negative differences to the east-south-east. Particularly, there are three peaks with maximum velocity differences, coinciding with the three minima in velocity dispersion maps.

The BPT map of the galaxy exhibits composite emission with a slight contribution from LINER emission in the core. This confirms that the contribution from the AGN to the overall gas disturbance in the galaxy is weak, indicating that the high velocity dispersions seen in the core, in an extended region $\sim$3 arcsec towards the north-east and south-west of the centre, is not associated with the AGN and is caused by another physical mechanism, potentially due to collision of gas along on-axis inflow. Throughout the FOV there is composite emission with a contribution from star formation.

The central regions of NGC 7177 exhibit complex kinematic behaviour. The emission-line maps show high and relatively extended nuclear velocity dispersion, accompanied by coherent structures spanning roughly a kiloparsec. These structures exhibit large amplitudes in both the deprojected residual velocity map ($\sim$70 km s^{-1}) and the velocity-difference map (up to $\sim$30 km s^{-1}). Although the BPT diagnostics do not indicate a dominant contribution from AGN-driven outflows within the inner kiloparsec, the overall kinematic complexity is likely influenced by AGN activity. The observed kinematics are also broadly consistent with on-axis inflow along the bar (E. Athanassoula 1992). Given the presence of extended-shock signatures, together with indications that the inner regions are affected by AGN activity, we classify this galaxy in the *extended shocks and outflow* category.

Downloaded from academic.oup.com/mnras/article/552/3/stag1204/8721813 by guest on 30 October 2026

A20 NGC 7513

The images and diagnostic maps of NGC 7513 are presented in Fig. A20. As shown in large-scale image, the galaxy has a bright core, a strong bar (R. J. Buta et al. 2009) within ∼30 arcsec radius, and two dusty star-forming spiral arms connecting to the ends of the bar. The MUSE FOV shown in the colour image covers the core, almost entire bar region with some portion of the spiral arms. The unsharp mask image of the galaxy reveals straight dust lanes within 12 arcsec along the bar; on the leading side of the bar, they pass the nucleus at ∼2 arcsec distance and continue ∼5 arcsec into the trailing sides.

As shown in the flux maps, within ∼6 arcsec radius, the emission across all line groups is weak, particularly for [O III]λ5007. Along the bar there is clumpy Hα and [N II]λ6583 emission, weak in the inner 12 arcsec radius, significantly stronger outside of it, indicating local SF along the bar lanes. In velocity maps of Hα and [N II]λ6583, the zero velocity line is bent by 90°at ∼10 arcsec radius, roughly at the locations where line emission becomes strong. The velocity dispersion of Hα and [N II]λ6583 is generally low. The values are ∼70 km s^{-1} in the core and ∼50 km s^{-1} within the regions with clumpy emission along the bar.

The disc inclination obtained by KINEMETRY converged around 46°. However, the radial distribution of the PA of the LON ranged between 100° and 130°. Examining different residual velocity maps, after altering the fixed PA of the LON between the accepted range of 100°–130°, we settled on using 105°as this value raised the least amount of artefacts. The final fixed parameters in the disc model, i 46°and PA of the LON 105°agree well with the parameters estimated from large-scale fits.

The residual velocity map of galaxy exhibits two straight coherent features along the bar appearing as counterparts, on its trailing side; one exhibiting positive and one exhibiting negative velocities, extending across few kiloparsecs. To guide the reader, these extended features are outlined with dashed lines in the deprojected residual velocity map shown in Fig. 3. These features extend beyond the bend of the zero velocity line, continuing outside the frame, all the way to the emanation of the spiral arms from the bar. They do not reflect the bend in the zero velocity line, which indicates different gas kinematics in the outer regions of the bar, where strong line emission is present, and the inner regions. These features have deprojected residual velocity magnitudes around 80–100 km s^{-1}, comparable to the structures seen in the other galaxies we studied in this work, and are similar to the extended features seen in the residual velocity map of NGC 289 (see Section A2). Although these features are on the trailing side of the bar, rather than the leading side as the typical extended shocks are, we still classify them as structures indicative of extended shocks due to their large coherent extent, magnitude, and similarities shown in other galaxies.

The velocity difference map of galaxy is noisy and shows no outstanding structures. Moreover, the BPT map exhibits a combination of composite LINER type emission in the core and contribution from SF along the bar lanes, where clumpy emission is seen.

APPENDIX B: SUPPLEMENTARY MAPS AND FIGURES

In this section, we present supplementary figures and maps that support the analysis discussed in the main body of this article.

Fig. B1 shows the flux, velocity, and velocity dispersion maps of NGC 1433, NGC 4303, and NGC 4321, derived from single-Gaussian fitting.

Fig. B2 shows the circular velocity maps for the galaxies in our sample. These maps are derived by fitting a rotating disc model to the Hα velocity field of each galaxy using KINEMETRY, with the fixed geometry, as described in Section 4.1.1 using orientation parameters (PA of LON and inclination) provided in Table 2.

Fig. B3 presents the deprojected residual velocity maps for galaxies in our sample that do not present extended structures, thus do not meet the criteria for extended shocks outlined in Section 4.3. Although some structures are visible, consideration of the full set of diagnostic maps does not support their interpretation as extended shocks. These maps are included for completeness.

Fig. B4 shows the distributions of Hα velocity dispersion and AON for all spaxels within an elliptical aperture of semimajor axis 1 kpc, corrected for the distance and inclination of each galaxy; as discussed in Section 6.3, this figure forms the basis for estimating a robust average Hα velocity dispersion within the central kiloparsec of each system. Table B1 presents the average Hα velocity dispersion values for each galaxy calculated using different weighting approaches: unweighed, flux, and AON weighted.

Downloaded from academic.oup.com/mnras/article/552/3/stag1204/8721813 by guest on 30 October 2026

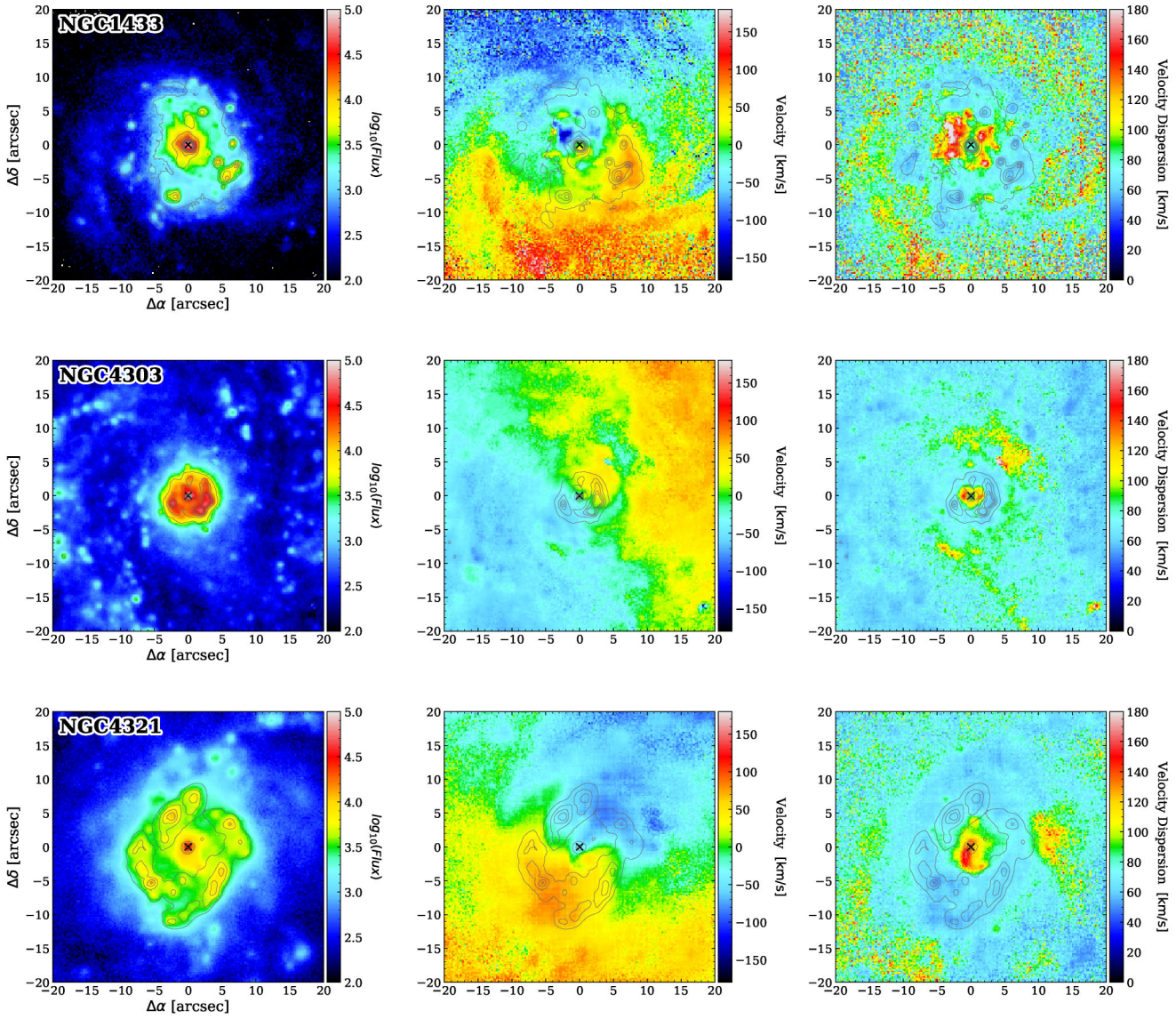

Figure B1. The [N II]λ6583 flux, velocity, and velocity dispersion maps of NGC 1433 (top), NGC 4303 (middle), and NGC 4321 obtained from single Gaussian fits. Grey contours represent the Hα emission. Centre of the galaxy is marked with an 'x'.

Downloaded from academic.oup.com/mnras/article/552/3/stag1204/8721813 by guest on 30 October 2026

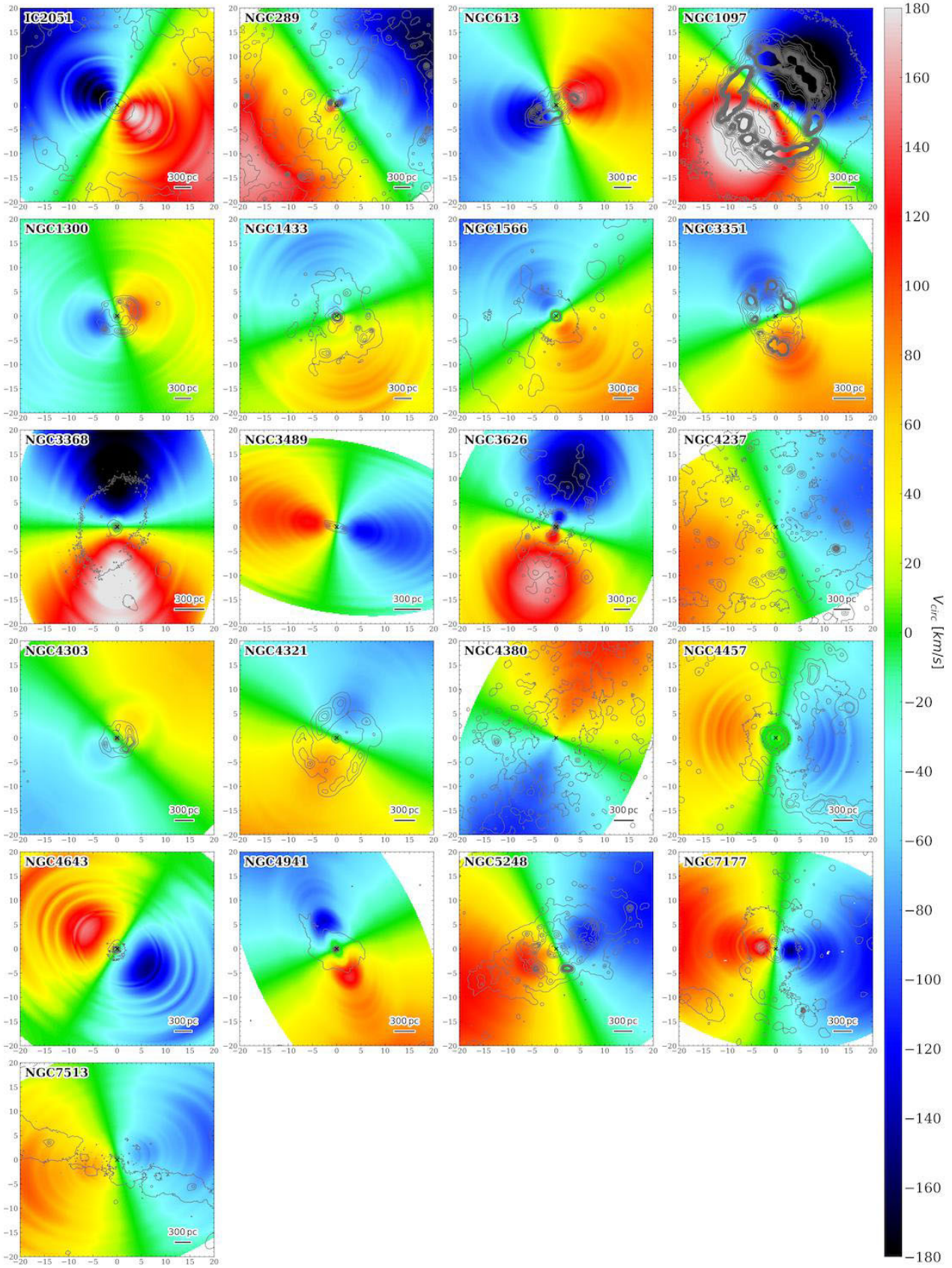

Figure B2. Maps of the circular velocity of a rotating disc, constructed with KINEMETRY using a fixed centre, PA, and inclination, with the adopted parameters listed in Table 2. The models are based on the Hα line-of-sight velocity field.

Downloaded from academic.oup.com/mnras/article/552/3/stag1204/8721813 by guest on 30 October 2026

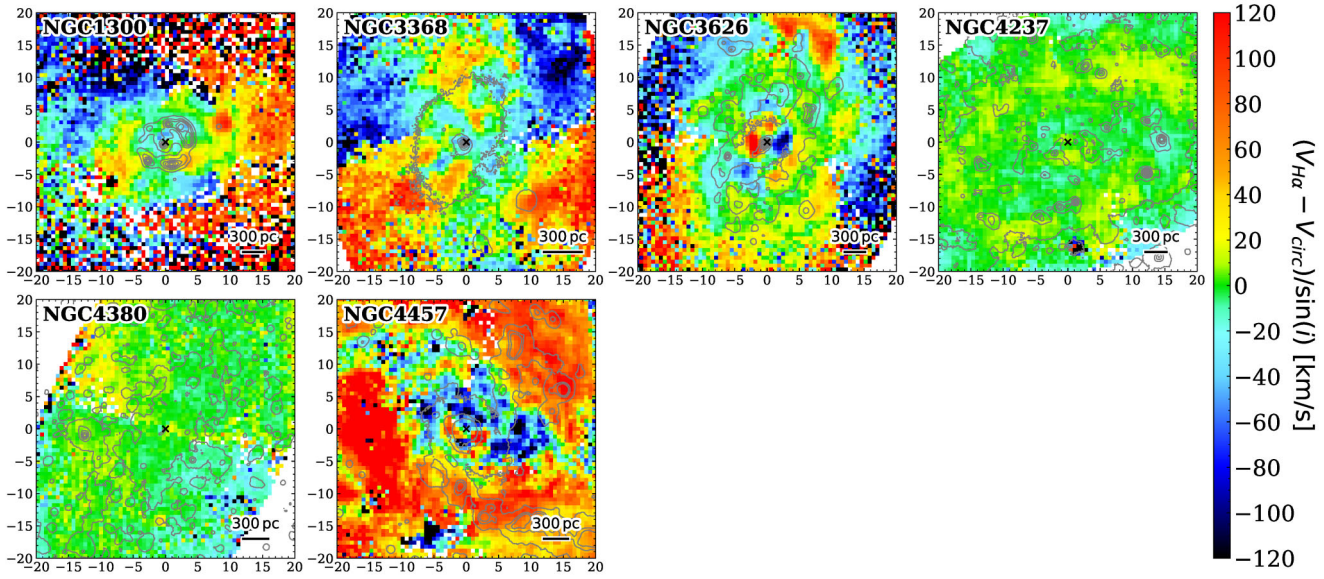

Figure B3. Maps of deprojected residual velocity for the galaxy sample studied in this work in which no extended structures are identified. The value of each spaxel is the average over 3 × 3 spaxels' box centred on it. The grey contours represent the Hα emission, dashed lines outline the coherent structures we identify on the maps.

Downloaded from academic.oup.com/mnras/article/552/3/stag1204/8721813 by guest on 30 October 2026

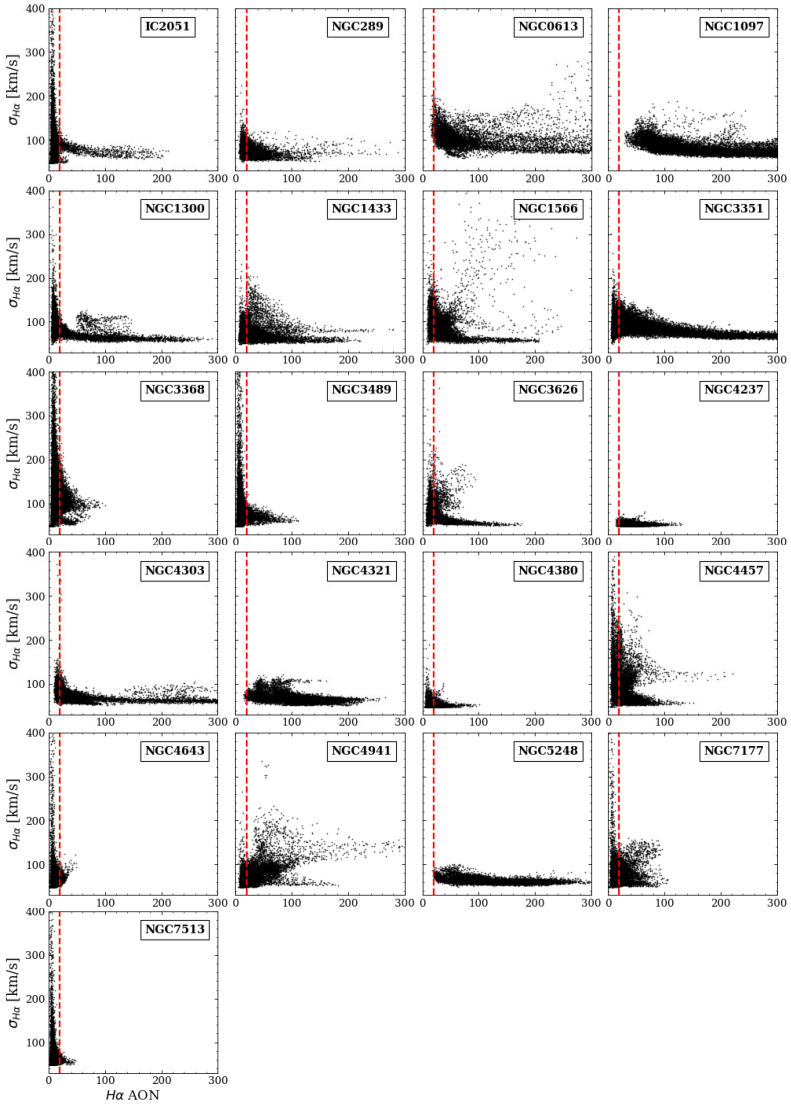

Figure B4. The distribution of spaxels within the inner kpc on the plane defined by the Hα velocity dispersion and AON for each galaxy studied in this work. The dashed line represents the AON = 20 threshold.

Downloaded from academic.oup.com/mnras/article/552/3/stag1204/8721813 by guest on 30 October 2026

Table B1. Comparison of the Hα velocity dispersion for each galaxy with different weighting approach used within calculation. Columns show the Galaxy ID, unweighted mean, flux-weighted mean, and AON-weighted mean.

Galaxy ID	Unweighted	Flux	AON
IC2051	77.6	72.8	73.8
NGC289	72.9	73.8	72.0
NGC0613	103.9	94.3	98.3
NGC1097	83.0	76.2	78.4
NGC1300	72.4	68.9	68.6
NGC1433	76.1	76.6	73.1
NGC1566	94.7	197.8	106.1
NGC3351	85.8	70.1	76.2
NGC3368	104.7	105.9	102.9
NGC3489	70.3	71.0	69.3
NGC3626	76.1	87.3	71.9
NGC4237	54.2	53.9	54.0
NGC4303	71.4	65.7	67.2
NGC4321	67.9	65.1	66.0
NGC4380	53.9	53.5	53.6
NGC4457	87.1	102.5	85.7
NGC4643	70.9	73.0	71.6
NGC4941	89.4	134.2	101.2
NGC5248	63.4	61.1	61.9
NGC7177	81.8	89.0	83.1
NGC7513	59.6	59.2	59.0

This paper has been typeset from a TEX/LATEX file prepared by the author.

Downloaded from academic.oup.com/mnras/article/552/3/stag1204/8721813 by guest on 30 October 2026

© The Author(s) 2026.
Published by Oxford University Press on behalf of Royal Astronomical Society. This is an Open Access article distributed under the terms of the Creative Commons Attribution License (https://creativecommons.org/licenses/by/4.0/), which permits unrestricted reuse, distribution, and reproduction in any medium, provided the original work is properly cited.